



# Mathematical Modelling and Numerical Simulation with Applications

ISSN Online : 2791-8564

Year : 2024

Volume : 4

Issue : 2



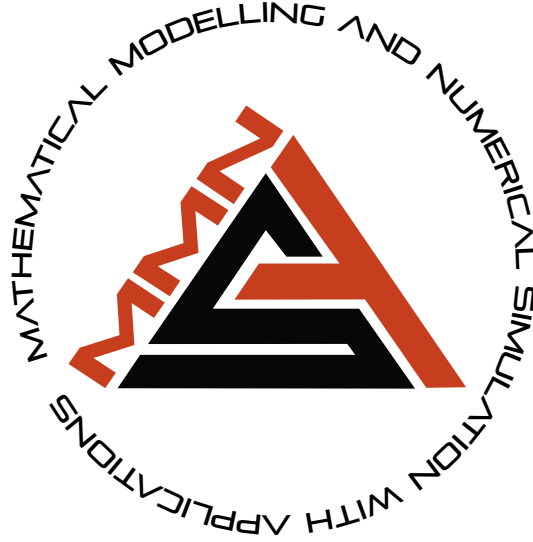
<https://dergipark.org.tr/en/pub/mmnsa>

Editor-in-Chief  
Mehmet Yavuz, PhD

M  
M  
N  
S  
A

VOLUME: 4 ISSUE: 2  
ISSN ONLINE: 2791-8564

June 2024  
<https://dergipark.org.tr/en/pub/mmnsa>



# MATHEMATICAL MODELLING AND NUMERICAL SIMULATION WITH APPLICATIONS

---

## Editor-in-Chief and Publisher

---

Mehmet Yavuz  
Department of Mathematics and Computer Sciences,  
Faculty of Science, Necmettin Erbakan University,  
Meram Yeniyol, 42090 Meram, Konya / TÜRKİYE  
mehmetyavuz@erbakan.edu.tr

---

## Associate Editors (In Alphabetical Order)

---

- **Abdeljawad, Thabet** - Prince Sultan University, Saudi Arabia
- **Agarwal, Praveen** - Anand International College of Engineering, India
- **Baleanu, Dumitru** - Cankaya University, Türkiye; Institute of Space Sciences, Bucharest, Romania
- **Hammouch, Zakia** - ENS Moulay Ismail University Morocco
- **Hristov, Jordan** - University of Chemical Technology and Metallurgy, Bulgaria
- **Karaca, Yeliz** - University of Massachusetts Chan Medical School, USA
- **Özdemir, Necati** - Balıkesir University, Türkiye
- **Pinto, Carla M.A.** - ISEP, Portugal
- **Sarris, Ioannis E.** - University of West Attica, Greece
- **Sene, Ndolane** - Cheikh Anta Diop University, Senegal
- **Stamova, Ivanka** - University of Texas at San Antonio, USA
- **Torres, Delfim F. M.** - University of Aveiro, Portugal
- **Townley, Stuart** - University of Exeter, United Kingdom

---

## Editorial Board Members (In Alphabetical Order)

---

- **Aguilar, José Francisco Gómez** - National Center for Technological Research and Development, Mexico
- **Ahmad, Hijaz** - International Telematic University, Uninettuno, Italy
- **Arqub, Omar Abu** - Al-Balqa Applied University, Jordan
- **Asjad, Muhammad Imran** - University of Management and Technology, Pakistan
- **Atangana, Abdon** - Faculty of Natural and Agricultural, Sciences, University of the Free State, South Africa
- **Başkonuş, Hacı Mehmet** - Harran University, Türkiye
- **Biswas, Md. Haider Ali** - Khulna University, Bangladesh
- **Bonyah, Ebenezer** - Akenten Appiah Menka University, Department of Mathematics Education, Ghana
- **Bulai, Iulia Martina** - University of Basilicata, Italy
- **Cabada, Alberto** - University of Santiago de Compostela, Spain
- **Dassios, Ioannis** - University College Dublin, Ireland
- **Eskandari, Zohreh** - Department of Mathematics, Faculty of Science, Fasa University, Fasa, Iran
- **Flaut, Cristina** - Ovidius University of Constanta, Romania
- **González, Francisco Martínez** - Universidad Politécnica de Cartagena, Spain
- **Gürbüz, Burcu** - Johannes Gutenberg-University Mainz, Institute of Mathematics, Germany
- **Jafari, Hossein** - University of Mazandaran, Iran; University of South Africa, UNISA003, South Africa
- **Jajarmi, Amin** - University of Bojnord, Iran
- **Kaabar, Mohammed K.A.** - Washington State University, USA
- **Kumar, Devendra** - University of Rajasthan, India

- **Kumar, Sunil** - National Institute of Technology, India
- **Lupulescu, Vasile** - Constantin Brâncuși University of Târgu-Jiu, Romania
- **Merdan, Hüseyin** - TOBB University of Economy and Technology, Department of Mathematics, Türkiye
- **Mohammed S. Abdo** - Hodeidah University, Al-Hodeidah, Department of Mathematics, Yemen
- **Muñoz-Pacheco, Jesus Manuel** - Faculty of Electronics Sciences at the Autonomous University of Puebla (BUAP), Mexico
- **Noeiaghdam, Samad** - Irkutsk National Research Technical University, Russian Federation
- **Owolabi, Kolade** - Federal University of Technology, Nigeria
- **Otero-Espinar, Maria Victoria** - University of Santiago de Compostela, Spain
- **Panigoro, Hasan S.** - Universitas Negeri Gorontalo, Indonesia
- **Povstenko, Yuriy** - Jan Dlugosz University in Czestochowa, Poland
- **Qureshi, Sania** - Mehran University of Engineering and Technology, Pakistan
- **Sabatier, Jocelyn** - Bordeaux University, France
- **Safaei, Mohammad Reza** - Florida International University, USA
- **Salahshour, Soheil** - Bahçeşehir University, Türkiye
- **Sarı, Murat** - Yıldız Technical University, Türkiye
- **Singh, Jagdev** - JECRC University, India
- **Valdés, Juan Eduardo Nápoles** - Universidad Nacional del Nordeste, Argentina
- **Veerasha, Pundikala** - Christ University, India
- **Weber, Gerhard-Wilhelm** - Poznan University of Technology, Poland
- **Xu, Changjin** - Guizhou University of Finance and Economics, China
- **Yang, Xiao-Jun** - China University of Mining and Technology, China
- **Yuan, Sanling** - University of Shanghai for Science and Technology, China

---

## Scientific Managing Editor

---

Fırat Evirgen  
Balıkesir University, Balıkesir / TÜRKİYE  
fevirgen@balikesir.edu.tr

---

## Technical Editor

---

Kerim Sarıgül  
Gazi University, Ankara / TÜRKİYE  
kerimsarigul@gazi.edu.tr

---

## English Editors (In Alphabetical Order)

---

- **Abdulkadir Ünal** - School of Foreign Languages, Foreign Languages, Alanya Alaaddin Keykubat University, Antalya Türkiye.
  - **Ahmet Sınak** - Necmettin Erbakan University, Department of Mathematics and Computer Sciences, Konya, Türkiye.
  - **Faruk Türk** - Karamanoğlu Mehmetbey University, School of Foreign Languages, Karaman, Türkiye.
  - **Richard Little** - University of Exeter, School of Foreign Languages, Penry Campus, Cornwall, United Kingdom.
- 

## Editorial Secretariat

---

Fatma Özlem Coşar  
Department of Mathematics and Computer Sciences,  
Faculty of Science, Necmettin Erbakan University,  
Meram Yeniyol, 42090 Meram, Konya / TÜRKİYE

Müzeyyen Akman  
Department of Mathematics and Computer Sciences,  
Faculty of Science, Necmettin Erbakan University,  
Meram Yeniyol, 42090 Meram, Konya / TÜRKİYE

---

# Contents

## *Research Articles*

- 1 Analysis of patient data to explore cardiovascular risk factors  
*Jawaher Almushayqih, Abayomi Samuel Oke, Belindar Atieno Juma* 133-148
- 2 Approximate solution of integral equations based on generalized sampling operators  
*Fuat Usta* 149-164
- 3 An approach to stochastic differential equations for long-term forecasting  
in the presence of  $\alpha$ -stable noise: an application to gold prices  
*Bakary D. Coulibaly, Chaibi Ghizlane, Mohammed El Khomssi* 165-192
- 4 Finite element static analysis of polyurethane-sandwiched skewed bridge decks  
*Ashwin Anand, Deepak Kumar Singh, Preeti Agarwal* 193-215
- 5 Mathematical modelling of using renewable energy in the power sectors  
for the sustainable environment  
*Md. Sirajul Islam, Mst. Shefali Khatun, Md. Haider Ali Biswas* 216-237



RESEARCH PAPER

## Analysis of patient data to explore cardiovascular risk factors

Jawaher Almushayqih <sup>1,†</sup>, Abayomi Samuel Oke <sup>2,\*,‡</sup> and Belindar Atieno Juma <sup>3,‡</sup>

<sup>1</sup>Department of Mathematics, College of Science, Qassim University, 52571 Buraydah, Saudi Arabia,

<sup>2</sup>Department of Mathematics, Adekunle Ajasin University, 342111 Akungba Akoko, Nigeria,

<sup>3</sup>Department of Mathematics, University College London, WC1E6BT London, United Kingdom

\*Corresponding Author

† [j.j.almoshigah@qu.edu.sa](mailto:j.j.almoshigah@qu.edu.sa) (Jawaher Almushayqih); [okeabayomisamuel@gmail.com](mailto:okeabayomisamuel@gmail.com) (Abayomi Samuel Oke); [belindarjuma.23@ucl.ac.uk](mailto:belindarjuma.23@ucl.ac.uk) (Belindar Atieno Juma)

### Abstract

According to the World Health Organisation, cardiovascular diseases claim over 17.9 million lives yearly on a global scale. Hence, cardiovascular diseases are responsible for 32 percent of global deaths yearly. Furthermore, it is estimated that more than 50 percent of heart disease cases are only discovered after they have reached the critical stage of heart failure and stroke. However, early detection of these heart diseases can reduce the mortality rates of cardiovascular diseases. Scientists have suggested using machine learning algorithms to identify the risk factors. However, the unavailability of data has hindered the significant success of this approach. In this study, machine learning algorithms are used to identify the important features that should be monitored to prevent heart diseases by considering a dataset obtained from 1000 patients. The six machine learning algorithms used for this study are Logistic Regression, Support Vector Machine, k-nearest Neighbour, Decision Tree, Random Forest and Multi-layer Perception Classifier. The dataset consists of twelve features that are considered to be associated with heart disease and a target variable. The results from this study show that patients suffering from typical and atypical angina chest pain are prone to heart disease. Patients who exercise up the slope have a higher likelihood of living without heart disease. Among the six algorithms used, the MLP Multi-layer Perception Classifier outperforms all others by achieving a 99 percent accuracy. Moreover, the Random Forest algorithm follows with an accuracy of 98 percent.

**Keywords:** Machine learning algorithms; cardiovascular diseases; heart disease; risk factors

**AMS 2020 Classification:** 68T01; 92B20; 92C50

## 1 Introduction

According to the World Health Organisation, Cardiovascular diseases (CVDs) are the leading cause of death, responsible for 32 percent of deaths globally [1]. CVDs have also been estimated

to be responsible for nearly 40 percent of premature deaths due to non-communicable diseases. The fact that CVDs can be prevented by improving behavioral factors necessitates the impetus to explore patients' data to identify patterns, correlations, and potential risk factors associated with heart disease [2]. This present study analyses a dataset of 1000 patients to provide information on the behavioral activities that can prevent cardiovascular health challenges.

The human heart, located in front of the chest behind the ribcage, is responsible for blood circulation throughout the body, control of the rhythm and speed of the heart rate and the maintenance of blood pressure [3]. The heart is divided into 5 parts; the walls, the chambers, the valves, the blood vessels and the electrical conduction system [4]. The muscles that contract and relax to pump blood throughout the body are the heart walls; separated into the left and right halves by a layer of muscle called the septum. The heart wall consists of three layers; endocardium (inner layer), myocardium (middle layer made up of muscle) and epicardium (outer layer of protection). There are four chambers in the heart; right atrium, left atrium, right ventricle and left ventricle. The atrium is on the top part of the heart while the ventricles are on the lower part. The right atrium receives blood with low oxygen content and pumps the blood through the right ventricle to the lungs for oxygenation. The oxygenated blood is passed back into the heart through the left atrium and finally pumped through the left ventricle to other parts of the body. The passageways in the heart are called the heart valves [5, 6]. The valves are classified as atrioventricular valves and semilunar valves. The tricuspid valve (the valve connecting the right atrium and right ventricle) and the mitral valve (between the left atrium and the left ventricle) are the atrioventricular valves. The semilunar valves open when blood flows out of the ventricles, the aortic valve and the pulmonary valve. The blood vessels are vessels through which blood is pumped to and from other parts of the body and there are three types of blood vessels; arteries, veins and capillaries [7]. The arteries carry oxygenated blood from the heart to other body parts (except the pulmonary artery that carries deoxygenated blood to the lungs), the veins carry deoxygenated blood into the heart (except the pulmonary vein that carries oxygenated blood from the lungs to the heart) and the capillaries are small blood vessels where your body exchanges oxygen-rich and oxygen-poor blood. The electrical conduction system is responsible for the exchange of electrical signals and pulses within the heart [8, 9].

The human heart is susceptible to a myriad of conditions, with heart disease representing a prominent threat [10]. Heart diseases are diseases that affect the heart, ranging from diseases that affect the blood vessels and heartbeat rhythm to the heart muscle and heart valves. Symptoms associated with heart disease depend on the type of heart disease. A common heart disease is coronary artery disease in which blood flow to and from the heart is hindered. Symptoms include chest pains, breath shortness, neck pain, numbness and weakness in the legs and arms. Heart attack or failure, angina and stroke are usually the symptoms that bring the patients to the hospital for diagnosis. Arrhythmias, a distortion in the rhythm of the heartbeat, is another common heart disease whose symptoms include chest pain, fainting, chest fluttering breath shortness, and slow breath [11]. Heart valve diseases and other diseases often come with symptoms such as chest pains, dizziness, and breath shortness. According to Shah et al. [12], the survival rate among heart disease patients is low because the diagnosis of most cases is done after the heart disease has reached critical stages. Recognizing the significance of early detection and intervention, this study explores key attributes that may contribute to the presence or absence of heart disease.

Machine learning (ML) is an artificial intelligence technique that learns hidden patterns in a dataset, aiding more accurate prediction or classification for decision-making. Several algorithms have been developed to guide the learning process and formulate a reliable model for any given dataset but the machine learning algorithms are generally categorised as either supervised (for datasets with a target column) or unsupervised (for datasets without a target column). Supervised learning

algorithms include linear regression, logistic regression, decision trees, random forest, support vector machine, k-Nearest Neighbours, Naive Bayes and Neural Networks. Unsupervised learning algorithms include K-Means Clustering, Density-Based Spatial Clustering of Applications with Noise, Autoencoders, t-distributed Stochastic Neighbour Embedding, Association Rule Mining and Singular Value Decomposition (SVD). ML algorithms have been applied by several authors on the UCI dataset and authors have found seemingly conflicting results on the best classifier. Saboor et al. [13] used XGBoost, random forest, decision trees, support vector machine (SVM), multinomial Naïve Bayes, logistic regression, linear discriminant analysis, AdaBoost classifier, and extra trees classifier on the UCI dataset on heart disease. The performance of all the algorithms indicates that the Support vector machine outperforms all other algorithms. Ramesh et al. [14] also considered the dataset by including the use of k-Nearest Neighbour, Random Forest, Decision Tree, Logistic Regression, Naive Bayes and SVM. In their study, k-NN outperformed other models. According to Chang et al. [15], the Random Forest classifier outperforms other classifiers. Boukhatem et al. [16] also found SVM as the best classifier among others. The inconsistencies in the outcomes of the studies could be due to the few data available on the UCI dataset on heart disease patients, containing only 303 rows.

In this study, we identify the human features that point towards heart disease. This is achieved by using machine learning algorithms to classify the data and extract the significance of each feature in contributing to heart disease. This current study differs from existing literature in two ways. Firstly, studies from the literature utilised the dataset sourced from the UCI website that consists of data from 303 patients, but this study utilises the dataset from the Kaggle website that consists of data from 1000 patients. The use of a larger dataset provides us with the potential to offer a richer understanding of cardiovascular risk factors. Secondly, this study delves into the question of classifier selection, building upon the observations from prior studies that revealed a lack of consensus among authors regarding the optimal classifier. The significance of this study includes the identification of the optimal classifier for cardiovascular disease. Furthermore, this study provides a good pointer to the features that can reduce the chance of heart disease in any patient.

## 2 Methodology

### Data source and features

The data on the cardiovascular disease dataset is downloaded from the Kaggle website (the data can be found on the link <https://www.kaggle.com/datasets/jocelyndumlao/cardiovascular-disease-dataset>). The dataset consists of 14 columns; column 1 for patients' identification number, columns 2 to 13 for the features, and column 14 for the target variable. The patient identification number is dropped from the dataset, leaving the 12 feature columns and 1 target column. The feature columns are age, gender, chestpain, restingBP, serumcholesterol, fastingbloodsugar, restingelectro, maxheartrate, exerciseangia, oldpeak, slope and noofmajorvessels.

**age:** The age feature is a numeric data that represents the age of a patient.

**gender:** The gender is considered binary taking 1 for male and 0 for female.

**chestpain:** The chestpain variable is the type of chest pain experienced by the patients. The chest pains are classified into four with 0 representing typical angina, 1 representing atypical angina, 2 representing non-anginal pain and 3 representing asymptomatic pain.

**restingBP:** The restingBP is a numeric data type, ranging between 94 mmHg and 200 mmHg, that shows the blood pressure of the patients when they are resting.

**serumcholesterol:** The serumcholesterol is a numeric data type that specifies the level of cholesterol in the blood of the patients, typically ranging between 126 mg/dl and 564mg/dl.

**fastingbloodsugar:** The fastingbloodsugar is a numeric data type that represents blood sugar

levels in the patients. It is divided into a binary mode where 0 represents blood sugar < 120 mg/dl and 1 represents blood sugar > 120 mg/dl.

**restingelectro:** The restingelectro is a nominal data type where 0 represents normal, 1 represents having ST-T wave abnormality, and 2 represents probable or definite left ventricular hypertrophy by Estes' criteria.

**exerciseangia:** The exerciseangia is binary data in which 0 indicates that there is no exercise-induced angina and 1 means angina is induced by exercise in the patient.

**maxheartrate:** The maxheartrate is a numeric data type between 71 and 202 for the maximum heart rate of the patient.

**oldpeak:** The oldpeak is a numeric value between 0 and 6.2 representing the ST depression induced by exercise relative to rest.

**slope:** The slope variable represents the type of slope on which exercises are carried out; 1 for upslope, 2 for flat surface, and 3 for downslope.

**noofmajorvessels:** The noofmajorvessels is a nominal value; 0, 1, 2, 3.

**target:** The target is a numeric variable that indicates whether the patient has heart disease (value=1) or does not have heart disease (value=0).

**Table 1.** Descriptive statistics for patients with heart disease

	count	mean	std	min	25%	50%	75%	max
age	420	49.07	18.7	20	32	49	66	80
gender	420	0.76	0.43	0	1	1	1	1
chestpain	420	0.36	0.68	0	0	0	1	3
restingBP	420	134.77	26.56	94	122	130	142	200
serumcholesterol	420	281.06	87.56	132	230	270	345	465
fastingbloodsugar	420	0.13	0.34	0	0	0	0	1
restingelectro	420	0.36	0.52	0	0	0	1	2
maxheartrate	420	136.31	39.26	71	103.75	134	171	202
exerciseangia	420	0.52	0.5	0	0	1	1	1
oldpeak	420	2.51	1.72	0	1.1	2.3	3.8	6.2
slope	420	0.6	0.55	0	0	1	1	2
noofmajorvessels	420	0.67	0.83	0	0	0	1	3
target	420	0	0	0	0	0	0	0

**Table 2.** Descriptive statistics for patients without heart disease

	count	mean	std	min	25%	50%	75%	max
age	580	49.37	17.25	20	35	49	63	80
gender	580	0.77	0.42	0	1	1	1	1
chestpain	580	1.43	0.87	0	1	2	2	3
restingBP	580	164.04	26.04	94	143	168	187	200
serumcholesterol	580	333.45	153.5	0	241	351.5	456.25	602
fastingbloodsugar	580	0.41	0.49	0	0	0	1	1
restingelectro	580	1.03	0.8	0	0	1	2	2
maxheartrate	580	152.12	28.22	96	133	152	175	202
exerciseangia	580	0.48	0.5	0	0	0	1	1
oldpeak	580	2.85	1.71	0	1.4	2.7	4.3	6.2
slope	580	2.22	0.65	1	2	2	3	3
noofmajorvessels	580	1.63	0.87	0	1	2	2	3
target	580	1	0	1	1	1	1	1

## Data description

Table 1 and Table 2 show the descriptive statistics for the patients with heart disease and without heart disease respectively. There are a total of 1000 patients out of which 420 are with heart disease and 580 are without heart disease. The mean age of patients with heart disease is 49.07 years while the mean age of the patients without heart disease is 49.37 years. This is an indication that patients who have heart disease are younger than the ones without heart disease. The mean chest pain for patients with heart disease is 0.36. This indicates that both typical and atypical angina chest pain are significant features signalling heart disease. The mean chest pain for the patients without heart disease is 1.43 and this indicates that non-angina chest pains are not an indication of heart disease. The analysis of the gender distribution is shown in Figure 1. The bar chart shows that there are more male patients with heart disease than there are females. It can also be seen that males visit the hospital more frequently to complain about heart-related problems.

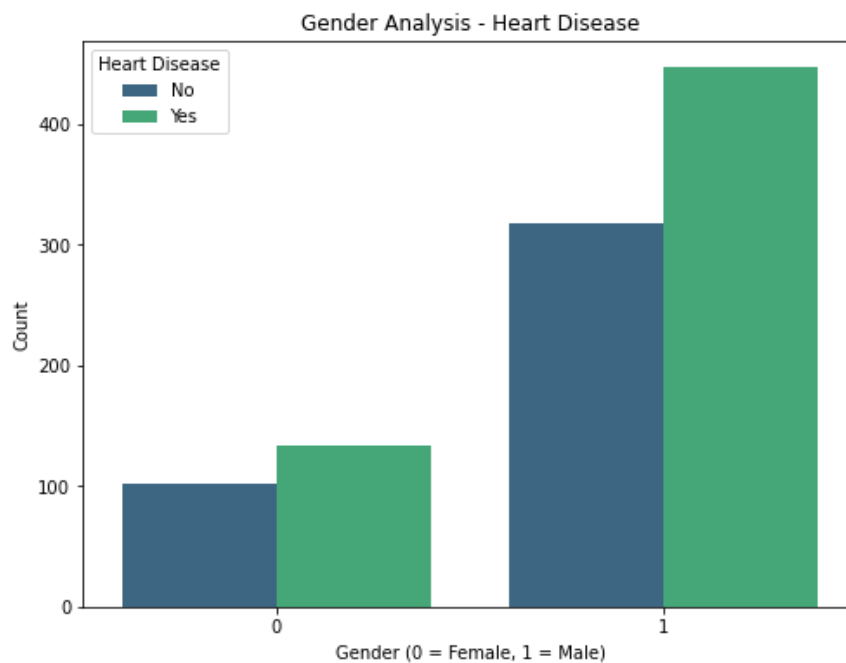


Figure 1. Gender analysis

## Data exploration

The characteristics and patterns in the dataset are explored with the aid of a correlation matrix and Kernel Density Estimation (KDE) plots. It is important to note that correlation coefficients range from -1 to 1 (where -1 indicates perfect negative correlation, 0 represents no correlation, and 1 represents perfect positive correlation). Figure 2 shows the correlation coefficients and what they mean. The correlation matrix shows the correlation between all the variables in the dataset. The correlation matrix between all the data features and the target is shown in Figure 3. Figure 3 shows the matrix of the correlation coefficients for all features and target variables. The correlation coefficients for all features against the target variable are recorded in the last row (and also the column) of the correlation matrix. The slope has the strongest positive correlation coefficient of 0.80, followed by chest pain (0.55) and then the number of vessels (0.49) and resting blood pressure (0.48) have a weak correlation with the target. The slope and chest pain show a very strong positive correlation with the target; indicating that heart disease in a patient is highly

dependent on the choice of slope of the peak exercise and the nature of the chest pain.

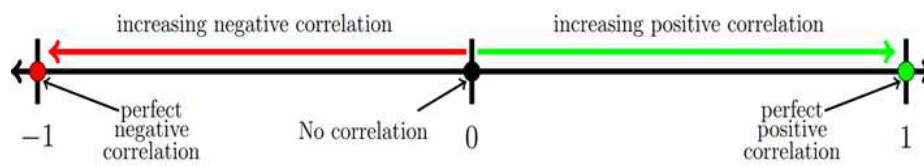


Figure 2. Correlation coefficients

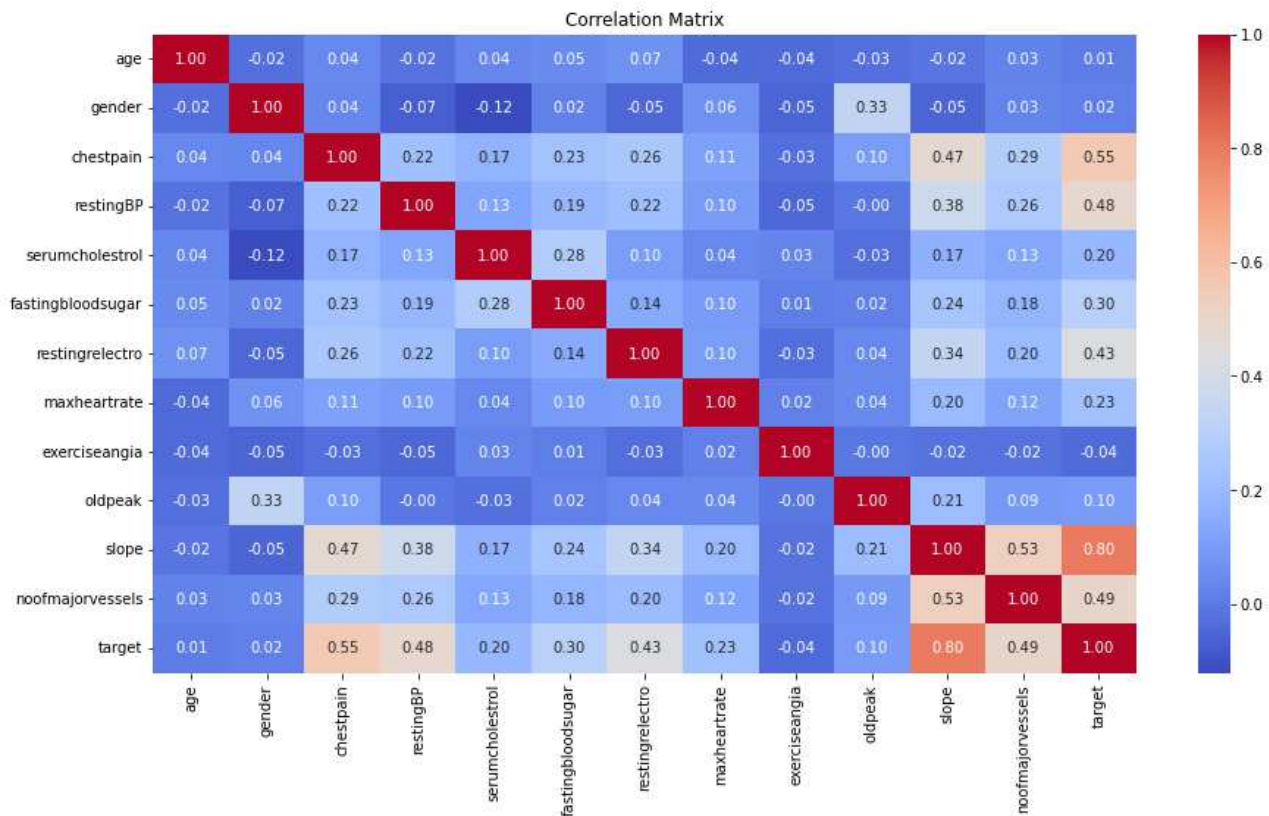


Figure 3. Correlation matrix

The KDE plot is used to estimate the probability distribution function of a dataset. By starting with the initial dataset, a smooth symmetric kernel is placed at each data point and the contribution of all kernels is summed up to create a continuous, smooth curve that estimates the probability density function. The results are normalised to ensure that the area under the curve is 1. In this case, the KDE plots for the two features that show a strong positive correlation with the target variable are displayed in Figure 4 and Figure 5. Figure 4 shows the distribution of slope with the density of the target. The slope is divided into 3 classes; 1 for upsloping, 2 for flat and 3 for downsloping. The upsloping represents the involvement of the patient in an exercise up a slope, the flat represents the involvement of the patient in an exercise on a flat surface, and The downsloping represents the involvement of the patient in an exercise down a slope. It is clear from the KDE plot that patients who are involved in exercises up the slope have a high tendency of not developing heart diseases and the patients who are involved in exercises on a flat surface or down the slope are more likely to have heart disease than the ones who engage in exercises up a slope. Figure 5 shows the distribution of chest pain with the density of the target. For chest

pain, the value 0 represents typical angina, value 1 represents atypical angina, value 2 represents nonanginal pain and value 3 represents asymptomatic chest pains. The concentration of patients with no disease is around 0 while the concentration of patients with diseases is around 2. The patients with angina chest pain are most likely not suffering from any heart disease while patients with non-anginal chest pain are most likely to suffer from heart disease.

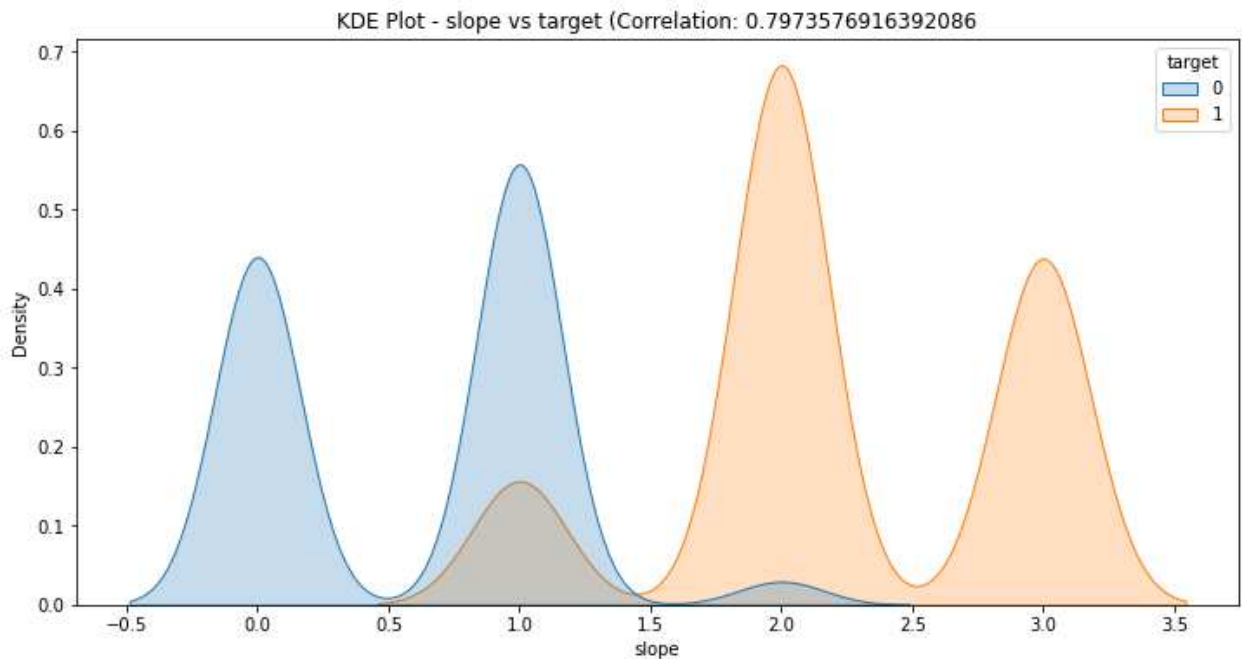


Figure 4. KDE plot for slope

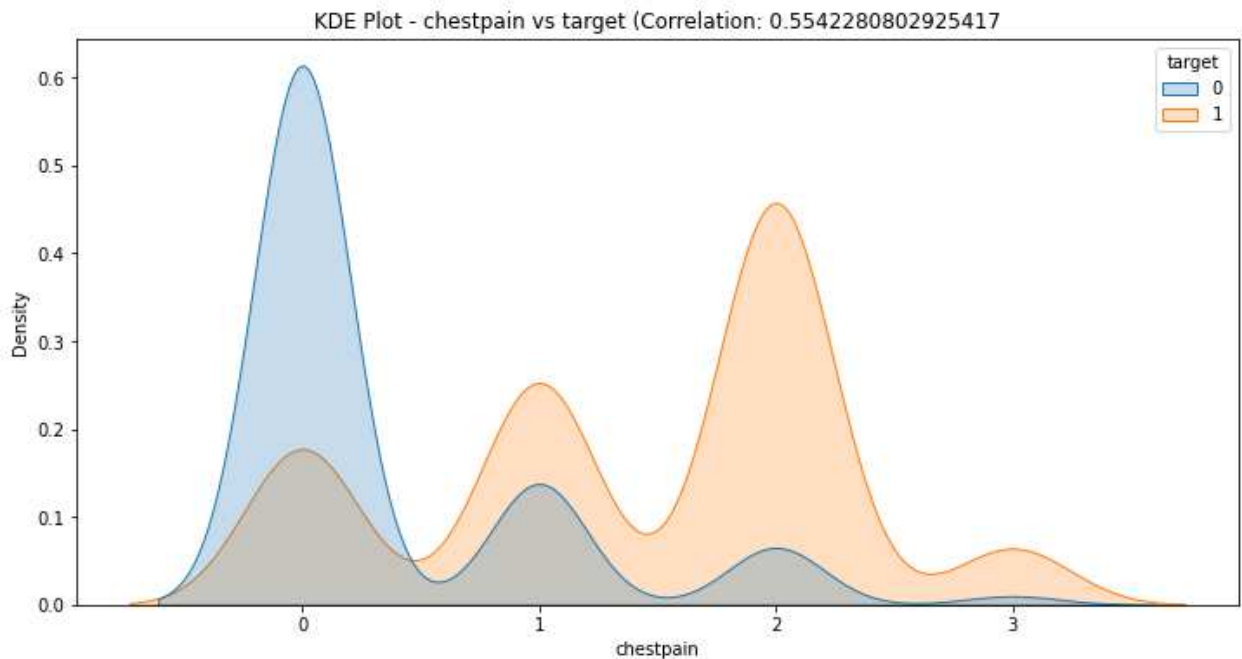


Figure 5. KDE plot for chestpain

## Machine learning algorithms

Six machine learning algorithms used in training the data are Logistic Regression (LR), Support Vector Machine (SVM),  $k$ -Nearest Neighbour ( $k$ NN), Decision tree, Random Forest and Multi-layer Perception Classifier (MLP). The algorithms are discussed below. The Logistic Regression [17, 18] estimates the probability that an instance belongs to one of two categories, hence it is used for binary classification. A linear regression model for the target variable  $y$  is formulated as a linear function of the features  $x_k$  as

$$y = \beta_0 + \sum_{k=1}^n x_k. \quad (1)$$

The sigmoid function

$$P(Y = 1) = \frac{1}{1 + \exp(\beta_0 + \sum_{k=1}^n \beta_k x_k)}, \quad (2)$$

is adopted to ensure results stay in the interval  $(0,1)$ . A decision line is used to separate the classes so that the instances above the line are classified into class 1 while the instances below are classified into class 0. The SVM classifier [19] attempts to obtain the optimal hyperplane (also called the support vector) that best separates the classes in the feature space. The hyperplane is usually of dimension  $n - 1$  for an  $n$ -dimensional feature space, thereby serving as the decision boundary. For a binary classification, a decision function  $f(x)$  is defined as

$$f(x) = \text{sgn}(w \cdot x + b), \quad (3)$$

(where  $w, x, b$  are the weight vector, feature vector and bias term) is used to determine the class for each instance. The  $k$ -nearest neighbour classifier [20] uses the Euclidean distance to measure the similarity between instances. The Euclidean distance is defined as

$$d_i = \left( \sum_{m=1}^k \|x_m - x_i\|^2 \right)^{\frac{1}{2}}. \quad (4)$$

The algorithm chooses the  $k$ -nearest neighbours to a certain instance and takes the frequency of their classes. The instance is allocated to the class with the highest frequency under the assumption that neighbouring instances have greater influences on each other. the choice of  $k$ , however, must be carefully made to avoid noise sensitivity or smoothing out local patterns. The Decision tree [21] algorithm starts by partitioning the dataset into subsets based on the significant attributes at each step. The tree starts with a root node, representing the entire dataset. The root node is partitioned into child nodes depending on the feature that provides the best separation. Next to the root node are the decision nodes, each representing a test condition on a specific feature. The predicted outcome is the leaf nodes, with each leaf corresponding to the class label for binary classification. Random Forest [22] uses a technique called bagging, which involves creating multiple subsets of the training dataset with replacement (bootstrap samples). Each subset is then used to train an individual Decision Tree. At each node of each Decision Tree, a random subset of features is considered for splitting. This randomness introduces diversity among the trees, leading to a more robust ensemble. For classification tasks, the final prediction is determined by a majority

vote among the trees. The Multi-layer Perceptron (MLP) [23] is a type of artificial neural network used for classification and regression. Its interconnected nodes are organized into an input layer, hidden layers, and an output layer. Each node in the network processes the input information using weights and biases. MLPs are trained to adjust the weights and biases in the model to minimize the difference between predicted and actual outcomes.

### Performance metrics

The metrics used in evaluating the performance of the six algorithms are confusion matrix, precision, recall, F1-score and accuracy. The confusion matrix is a matrix of the form shown in Figure 6. The true positive is the number of classifications that were classified as 0 that truly belong to the class 0, false positive is the number of classifications that were classified as 0 that do not belong to class 0, false negative is the number of classifications that were classified as 1 that does not belong to class 1, true negative is the number of classifications that were classified as 1 that truly belong to class 1.

0	True Positive (TP)	False Positive (FP)
1	False Negative (FN)	True Negative (TN)
	0	1

Figure 6. Confusion matrix general form

The confusion matrices provide a comprehensive view of the model’s performance but precision, recall, F1-score, and support are derived metrics that offer more specific insights about the models. The precision gives an insight into the accuracy of a positive classification and is defined as the ratio of True Positives to the Total Positive Classification i.e.,

$$\text{precision} = \frac{\text{True Positive}}{\text{True Positive} + \text{False Positive}} \tag{5}$$

The recall measures the ability of the model to capture all positive instances and is defined as the ratio of true positive to the total positive

$$\text{recall} = \frac{\text{True Positive}}{\text{True Positive} + \text{False Negative}} \tag{6}$$

The F1 score gives a single metric that provides a balance between false positives and false negatives and is defined as

$$\text{F1 Score} = 2 \times \frac{\text{precision} \times \text{recall}}{\text{precision} + \text{recall}} \tag{7}$$

The accuracy of a model is the metric that measures the overall correctness of the model and is

defined as

$$\text{accuracy} = \frac{\text{True Positive} + \text{recall}}{\text{True Positive} + \text{False Positive} + \text{True Negative} + \text{False Negative}}. \quad (8)$$

In this study, all codes were executed using Spyder on Anaconda distribution. The machine used is a 64-bit operating system, x64-based processor, Intel(R) Core(TM) i7-8565U CPU @ 1.80GHz 1.99 GHz HP laptop.

### 3 Analysis and discussion of results

The dataset was split into two; 80 percent for training and 20 percent for testing. The machine learning algorithms learned from the training dataset to build a model for Classification. By using the models to predict the classes of the testing dataset, the confusion matrix and other metrics can be used to evaluate each of the algorithms. The confusion matrices for all six algorithms are shown in [Figure 7](#). All six models classify 83 instances into class 0 and 117 instances into class 1. The k-NN model classifies 78 instances accurately into class 0 and 109 instances correctly into class 1 while it wrongly classifies 5 instances into class 0 and 8 instances into class 1 (see [Figure 7\(a\)](#)). The SVM model classifies 79 instances accurately into class 0 and 113 instances correctly into class 1 while it wrongly classifies 4 instances into class 0 and 4 instances into class 1 (see [Figure 7\(b\)](#)). The LR model accurately classifies 79 instances into class 0 and 114 instances correctly into class 1 while it wrongly classifies 4 instances into class 0 and 3 instances into class 1 (see [Figure 7\(c\)](#)). The Decision Tree model classifies 78 instances accurately into class 0 and 115 instances correctly into class 1 while it wrongly classifies 5 instances into class 0 and 2 instances into class 1 (see [Figure 7\(d\)](#)). The RF model classifies 81 instances accurately into class 0 and 115 instances correctly into class 1 while it wrongly classifies 2 instances into class 0 and 2 instances into class 1 (see [Figure 7\(e\)](#)). The MLP model classifies 82 instances accurately into class 0 and 115 instances correctly into class 1 while it wrongly classifies 1 instance into class 0 and 2 instances into class 1 (see [Figure 7\(a\)](#)). Checking through the confusion matrices, MLP outperforms all the remaining 5 models while k-NN performs the least among all the models.

The superior performance of the Multi-layer Perceptron (MLP) Classifier in this study could be attributed to several factors. MLP is a type of neural network capable of learning complex, non-linear decision boundaries due to its multiple layers and non-linear activation functions. This property of MLP is particularly advantageous if the relationships in the data are not linearly separable. Also, MLP can automatically capture and model interactions between features which other algorithms (such as Logistic Regression) might require manual feature engineering to capture such interactions effectively. MLPs benefit from advanced optimization algorithms like Adam or RMSprop, which help in efficiently navigating the complex loss landscape and converging to a good solution.

[Table 3](#) shows the precision, recall, F1-score, and accuracy of the six algorithms. MLP has 98 percent precision in classifying class 0 correctly, 99 percent precision in classifying class 1 correctly and 99 percent accuracy in any classification. RF has a precision of 98 percent in classifying into either class 0 or 1 and an accuracy of 98 percent in any classification. However, k-NN has 91 percent precision in classifying an instance into class 0, 96 percent precision in classifying an instance into class 1 and an accuracy of 94 percent in any classification. Hence, the MLP outperforms all the other algorithms and can therefore be used in this context to discuss the effects of the features on the chance of heart disease in any patient.

It is important to note that the correlation matrix indicates that the slope and chest pain are very significant in determining the chance of a patient having a heart disease. However, the outcome

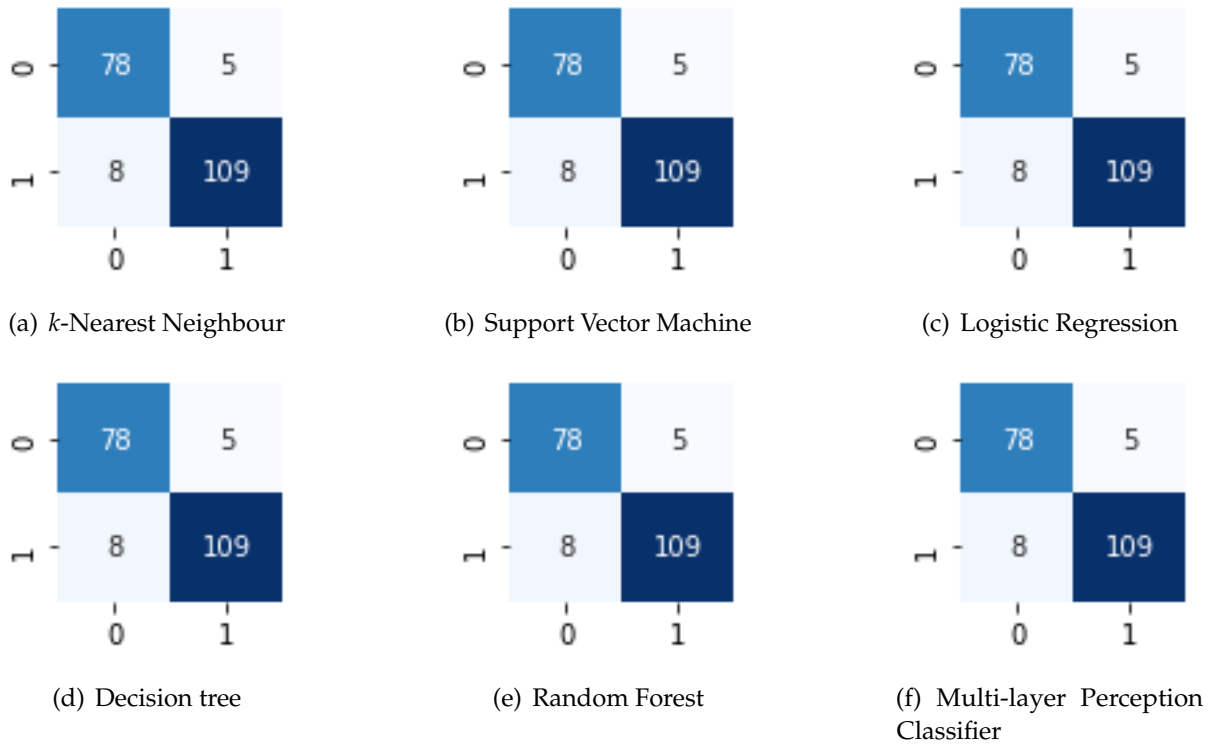


Figure 7. Confusion matrices for the six algorithms

Table 3. Performance metrics for the six models

		0	1	accuracy			0	1	accuracy
MLP	precision	98%	99%	99%	Random Forest	precision	98%	98%	98%
	recall	99%	98%	99%		recall	98%	98%	98%
	f1-score	98%	99%	99%		f1-score	98%	98%	98%
Decision Tree	precision	98%	96%	97%	Logistic Regression	precision	96%	97%	97%
	recall	94%	98%	97%		recall	95%	97%	97%
	f1-score	96%	97%	97%		f1-score	96%	97%	97%
SVC	precision	95%	97%	96%	KNN	precision	91%	96%	94%
	recall	95%	97%	96%		recall	94%	93%	94%
	f1-score	95%	97%	96%		f1-score	92%	94%	94%

only showed the correlation of a feature against the target without considering other features. A more detailed observation is carried out using the Random Forest to estimate the importance of each feature in determining the chance of heart disease in a patient. The Feature Importance is shown in Figure 8. The slope remains at the top of the chart, with the highest importance in determining whether a patient has heart disease or not. The resting blood pressure, old peak, serum cholesterol and chest pain are also significant in determining the heart condition of a patient.

#### 4 Conclusion, recommendations and future research

##### Conclusion

Twelve features that are considered to be associated with heart disease were recorded for 1000 patients. Each patient was tested for any heart disease and the record is taken as 0 (if they have no heart disease) and 1 (if they have a heart disease). Out of the 1000 patients, 420 have heart disease and 580 do not have any heart disease. The data description shows that both typical

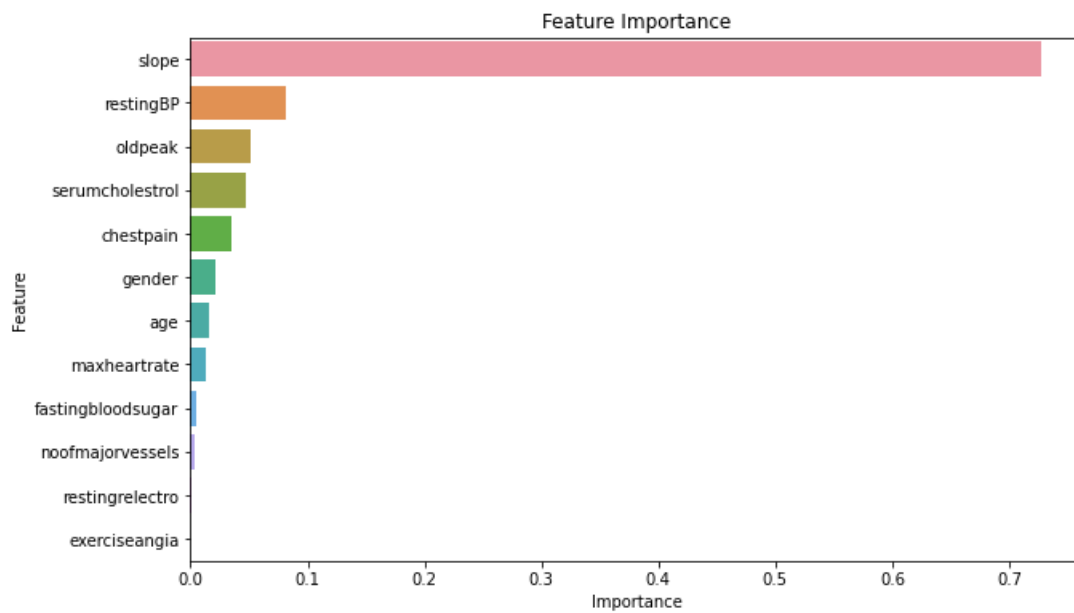


**Figure 8.** Feature importance

and atypical angina types of chest pain are features that are common among patients with heart diseases and hence, patients suffering from atypical angina chest pain are prone to heart disease and this agrees with the findings of Cubukcu et al. [24]. Furthermore, the male gender suffers from heart disease more than the females do. By drawing the correlation matrix, it is observed that the slope upon which a patient exercises is highly indicative of whether they will have heart disease or not. The Slope is found to have the strongest positive correlation coefficient of 0.80 with the heart disease condition of the patients, followed by chest pain (0.55). The KDE plot however showed that exercises up the slope is a good preventive measure for heart disease.

Machine learning classifiers are used to analyse the dataset to identify patterns and classify the instances. Performances of the classifiers were measured by using the confusion matrix, precision, recall, F1-score and accuracy. The results indicate the superiority of MLP over the other classifiers with an accuracy of 99 percent. The Random Forest algorithm follows with an accuracy of 98 percent. In furtherance to the analytics, the feature importance is estimated using the Random Forest. The result indicates that the slope upon which the patient carries out exercises is of the highest importance in determining whether a patient has heart disease or not. The resting blood pressure, old peak, serum cholesterol and chest pain are also significant in determining the heart condition of a patient.

### Practical recommendations for patients and healthcare providers

The insights from this study highlight several key features associated with heart disease. Practical recommendations for patients and healthcare providers include:

- **Regular Monitoring and Screening:** The study showed that resting BP, serum cholesterol, and fasting blood sugar are significant factors in heart disease. Patients should regularly monitor their blood pressure, cholesterol levels, and blood sugar. Healthcare providers should prioritise these screenings during routine check-ups, especially for high-risk groups such as older adults.
- **Chest Pain Evaluation:** The study identified chest pain as a significant feature associated with heart disease. Any form of chest pain, particularly atypical angina, should be promptly evaluated by healthcare providers. Early detection and management of chest pain can prevent the progression to heart disease.

- **Exercise Recommendations:** The slope of exercise was found to be the most critical factor in determining heart disease. Engaging in regular physical activity, especially exercises that involve varying slopes, can be beneficial. Providers should encourage patients to incorporate such exercises into their routines as they are shown to be good preventive measures against heart disease.
- **Gender-Specific Approaches:** The study found that males suffer from heart disease more than females. Given that males are more prone to heart disease than females in this study, tailored intervention programs should be developed to address specific risk factors prevalent in men.

### Implications for public health initiatives

The findings from the study have several implications for public health initiatives aimed at preventing cardiovascular disease:

- **Targeted Screening Programs:** Resting BP, serum cholesterol, and chest pain were significant factors identified. Public health campaigns should promote regular health screenings for high-risk individuals, focusing on monitoring blood pressure, cholesterol, and chest pain.
- **Health Education and Awareness:** The study highlighted the importance of chest pain and exercise slope. Increase public awareness about the importance of recognizing symptoms such as atypical angina and understanding their risks. Educational campaigns can inform the public about the significance of regular exercise, particularly on varied slopes, as a preventive measure.
- **Promotion of Physical Activity:** The slope of exercise was found to be highly indicative of heart disease presence. Encourage communities to create and maintain spaces where people can engage in physical activities that include varied terrain to promote heart health. Public health initiatives can include organized exercise programs that emphasize the benefits of slope exercises.

### Key behavioural activities

The study identified a lack of regular exercise as a key risk factor for heart disease. The slope of exercise was identified as the most critical factor. The findings underscore the importance of regular physical activity, especially exercises involving varied slopes, as a preventive measure against heart disease. Inactivity or insufficient exercise can increase the risk. By addressing these key behavioural activities, both patients and healthcare providers can better manage and mitigate the risks associated with heart disease.

### Future direction

The risk factors identified in this study by considering the demographic information (age and gender), clinical information (resting BP, serum cholesterol, fasting blood sugar, maximum heart rate and old peak), symptom information (chest pain and exercise angina) and diagnostic test results (resting electro, slope and the number of major vessels). Further research is required to include the Lifestyle Factors (Diet, Physical activity level, Smoking status, and Alcohol consumption), Genetic Factors (Family history of heart disease and Genetic predispositions), Environmental Factors (Air quality exposure, Noise pollution exposure and Socioeconomic status), Psychological Factors (Stress levels, Mental health status and Sleep quality) and Healthcare Access (Frequency of medical check-ups, Accessibility to healthcare facilities and Health insurance status). Including these factors will increase the reliability of the outcomes.

## Declarations

### Use of AI tools

The authors declare that they have not used Artificial Intelligence (AI) tools in the creation of this article.

### Data availability statement

The dataset used for this study was obtained from Kaggle website:

<https://www.kaggle.com/datasets/jocelyndumlao/cardiovascular-disease-dataset>

### Ethical approval (optional)

Not applicable

### Consent for publication

Not applicable

### Conflicts of interest

The authors declare that they have no conflict of interest.

### Funding

No funding was received for this research.

### Author's contributions

J.A.: Conceptualization, Methodology, Data Curation, Writing - Original Draft, Writing - Review & Editing. A.S.O.: Methodology, Software, Validation, Writing - Review & Editing, Visualization, Supervision. B.A.J.: Validation, Formal Analysis, Writing - Original Draft, Writing - Review & Editing, Visualization. All authors discussed the results and contributed to the final manuscript.

### Acknowledgements

All authors want to show thankfulness to each contribution for accomplishing this research work.

### References

- [1] WHO, Cardiovascular diseases, (2023). <https://www.who.int/health-topics/cardiovascular-diseases>.
- [2] Allen, L.A., Stevenson, L.W., Grady, K.L., Goldstein, N.E., Matlock, D.D., Arnold, R.M. et al. Decision making in advanced heart failure: a scientific statement from the American Heart Association. *Circulation*, 125(15), 1928–1952, (2012). [[CrossRef](#)]
- [3] Mori, S., Tretter, J.T., Spicer, D.E., Bolender, D.L. and Anderson, R.H. What is the real cardiac anatomy? *Clinical Anatomy*, 32(3), 288–309, (2019). [[CrossRef](#)]
- [4] Buijtendijk, M.F.J., Barnett, P. and Van Den Hoff, M.J.B. Development of the human heart. *American Journal of Medical Genetics Part C: Seminars in Medical Genetics*, 184(1), 7-22, (2020). [[CrossRef](#)]
- [5] Gumpangseth, T., Mahakkanukrauh, P. and Das, S. Gross age-related changes and diseases in human heart valves. *Anatomy & Cell Biology*, 52(1), 25-33, (2019). [[CrossRef](#)]
- [6] Gumpangseth, T., Lekawanvijit, S. and Mahakkanukrauh, P. Histological assessment of the

- human heart valves and its relationship with age. *Anatomy & Cell Biology*, 53(3), 261–271, (2020). [[CrossRef](#)]
- [7] Niklason, L.E. and Lawson, J.H. Bioengineered human blood vessels. *Science*, 370(6513), (2020). [[CrossRef](#)]
- [8] Padala, S.K., Cabrera, J.A. and Ellenbogen, K.A. Anatomy of the cardiac conduction system. *Pacing and Clinical Electrophysiology*, 44(1), 15–25, (2021). [[CrossRef](#)]
- [9] Hochman-Mendez, C., Mesquita, F.C.P., Morrissey, J., Da Costa, E.C., Hulsmann, J., Tang-Quan, K. et al. Restoring anatomical complexity of a left ventricle wall as a step toward bioengineering a human heart with human induced pluripotent stem cell-derived cardiac cells. *Acta Biomaterialia*, 141, 48–58, (2022). [[CrossRef](#)]
- [10] Khan, M.A.B., Hashim, M.J., Mustafa, H., Baniyas, M.Y., Al Suwaidi, S.K.B.M., AlKatheeri, R. et al. Global epidemiology of ischemic heart disease: results from the global burden of disease study. *Cureus*, 12(7), (2020). [[CrossRef](#)]
- [11] Khairy, P. Arrhythmias in adults with congenital heart disease: what the practicing cardiologist needs to know. *Canadian Journal of Cardiology*, 35(12), 1698–1707, (2019). [[CrossRef](#)]
- [12] Shah, D., Patel, S. and Bharti, S.K. Heart disease prediction using machine learning techniques. *SN Computer Science*, 1, 345, (2020). [[CrossRef](#)]
- [13] Saboor, A., Usman, M., Ali, S., Samad, A., Abrar, M.F. and Ullah, N. A method for improving prediction of human heart disease using machine learning algorithms. *Mobile Information Systems*, 2022(1), 1410169, (2022). [[CrossRef](#)]
- [14] Ramesh, T.R., Lilhore, U.K., Poongodi, M., Simaiya, S., Kaur, A. and Hamdi, M. Predictive analysis of heart diseases with machine learning approaches. *Malaysian Journal of Computer Science*, 132–148, (2022). [[CrossRef](#)]
- [15] Chang, V., Bhavani, V.R., Xu, A.Q. and Hossain, M.A. An artificial intelligence model for heart disease detection using machine learning algorithms. *Healthcare Analytics*, 2, 100016, (2022). [[CrossRef](#)]
- [16] Boukhatem, C., Youssef, H.Y. and Nassif, A.B. Heart disease prediction using machine learning. In *Proceedings, 2022 Advances in Science and Engineering Technology International Conferences (ASET)*, pp. 1-6, Dubai, United Arab Emirates, (2022, February). [[CrossRef](#)]
- [17] Ahmadini, A.A.H. A novel technique for parameter estimation in intuitionistic fuzzy logistic regression model. *Ain Shams Engineering Journal*, 13(1), 101518, (2022). [[CrossRef](#)]
- [18] José R. Berrendero, Beatriz Bueno-Larraz, and Antonio Cuevas. On functional logistic regression: some conceptual issues. *Test*, 32, 321-349, (2023). [[CrossRef](#)]
- [19] Joshi, A.V. Support vector machines. In *Machine Learning and Artificial Intelligence* (pp. 89–99). Cham, Switzerland: Springer International Publishing, (2023). [[CrossRef](#)]
- [20] Nino-Adan, I., Landa-Torres, I., Portillo, E. and Manjarres, D. Influence of statistical feature normalisation methods on K-Nearest Neighbours and K-Means in the context of industry 4.0. *Engineering Applications of Artificial Intelligence*, 111, 104807, (2022). [[CrossRef](#)]
- [21] Meng, L., Bai, B., Zhang, W., Liu, L. and Zhang, C. Research on a decision tree classification algorithm based on granular matrices. *Electronics*, 12(21), 4470, (2023). [[CrossRef](#)]
- [22] Bai, J., Li, Y., Li, J., Yang, X., Jiang, Y. and Xia, S.T. Multinomial random forest. *Pattern Recognition*, 122, 108331, (2022). [[CrossRef](#)]
- [23] Al Bataineh, A., Kaur, D. and Jalali, S.M.J. Multi-layer perceptron training optimization using

nature inspired computing. *IEEE Access*, 10, 36963–36977, (2022). [[CrossRef](#)]

[24] Cubukcu, A., Murray, I. and Anderson, S. What's the risk? Assessment of patients with stable chest pain. *Echo Research & Practice*, 2(2), 41–48, (2015). [[CrossRef](#)]

Mathematical Modelling and Numerical Simulation with Applications (MMNSA)  
(<https://dergipark.org.tr/en/pub/mmnsa>)



**Copyright:** © 2024 by the authors. This work is licensed under a Creative Commons Attribution 4.0 (CC BY) International License. The authors retain ownership of the copyright for their article, but they allow anyone to download, reuse, reprint, modify, distribute, and/or copy articles in MMNSA, so long as the original authors and source are credited. To see the complete license contents, please visit (<http://creativecommons.org/licenses/by/4.0/>).

**How to cite this article:** Almushayqih, J., Oke, A.S. & Juma, B.A. (2024). Analysis of patient data to explore cardiovascular risk factors. *Mathematical Modelling and Numerical Simulation with Applications*, 4(2), 133-148. <https://doi.org/10.53391/mmnsa.1412304>



RESEARCH PAPER

## Approximate solution of integral equations based on generalized sampling operators

Fuat Usta <sup>1,\*</sup> ‡

<sup>1</sup>Department of Mathematics, Faculty of Science and Arts, Düzce University, 81620 Düzce, Türkiye

\* Corresponding Author

‡ fuatusta@duzce.edu.tr (Fuat Usta)

### Abstract

In this manuscript, we present and test a numerical scheme with an algorithm to solve Volterra and Abel's integral equations utilizing generalized sampling operators. Illustrative computational examples are included to indicate the validity and practicability of the proposed technique. All of the computational examples in this research have been computed on a personal computer implementing some programs coded in MATLAB.

**Keywords:** Generalized sampling operators; integral equations; numerical results

**AMS 2020 Classification:** 65R20; 94A20; 45D05; 47N20

### 1 Introduction

Integral equations have an important place in the application of mathematical analysis to today's problems. Since integral equations are a vast field of research, a theory that will include all integral equations cannot be established. Therefore, they are examined separately according to their characteristics. Considering these separate examinations, integral equations are divided into Volterra and Fredholm integral equations. In the conducted studies, Volterra integral equations are in the foreground and the relationship between differential equations is established in detail. A variable or constant coefficient differential equation with initial conditions can be converted to a Volterra integral equation or an integral equation can be converted to a differential equation. Therefore, an integral equation can also be considered as a boundary value problem of the differential equation provided for the initial conditions.

It is known that differential equations are not enough to define a problem by itself. Therefore, initial or boundary conditions must be added to the problem in a differential equation. Similarly, initial or boundary conditions are necessary for the problems defined by integral equations. In other words, integral equations include the initial conditions through the Green functions. Thus, it

shows similar aspects of integral and differential equations. In addition, integral equations require integral over the domain space which is defined according to the nature of integral equations. It means that the value of the unknown function at a point is found in terms of expressions containing the integral of that function over the domain space.

The first studies known with integral equations were performed in the first half of the 19th century. Previously, systematic research has not been conducted [1]. However, more methodical researches were carried out towards the end of this century and some results started to be obtained. It is known for the first time that Abel came across an integral equation when he dealt with a mechanical problem of the *tautochrone* in 1823 [2, 3]. Abel presented the general formula for the mechanical problems he worked on as follows:

$$\varphi(\eta) = \int_0^\alpha \frac{\phi(\xi)}{(\eta - \xi)^2} d\xi, \quad \varphi(0) = 0, \quad \alpha \in (0, 1),$$

and gave the solution to this problem in 1826 [2]. In this equation, if  $\alpha = 0$  and  $\alpha = 1/2$ , the original equation that Abel encountered was obtained, and the famous *tautochrone* problem related to this equation was first solved by Huygens [4].

In some cases, it may not be possible to find the analytical solution of the integral equation due to their nature. In situations like this, it becomes necessary to investigate the existence of a numerical solution of the integral equation. In order to solve Volterra integral equations numerically, there are a number of proposed techniques in literature such as Taylor-series expansion method, Legendre wavelet method, Adomian decomposition method, Sinc-collection method and power series method [5–13]. In addition to this, in [14], the authors introduced a numerical technique for solving Volterra integral equation of second kind, first kind and even singular types of these equations by using the Bernstein Approximation method. Afterward, Usta et.al. [15] introduced the numerical solution of both second and first-kind Volterra integral equations with the aid of Szasz-Mirakyan operators. Other numerical approaches can be found in [16, 17].

On the other hand, approximation theory is one of the fundamental topics of mathematical analysis. One of the main problems of the approximation theorem is to show the given function  $f$  in the form of a series representation of functions that have better properties than itself. In 1885, Weierstrass was the researcher who made the first studies on the approximation theorem. After the famous theorem of Weierstrass, a number of studies have been conducted on the approximation theorem, [18], such as those involving Bernstein approximations. Furthermore, one of the most significant of those studies is the sampling theorem. The main theorem of generalized sampling theorem was introduced to the literature by Butzer and his colleagues at RWTH Aachen in the late 1970s and has been studied by a number of mathematicians as of this date [19–22]. One of the most important superior features of the generalized sampling theorem is that it converges in an infinite interval rather than converging in a closed interval  $[0, 1]$  like Bernstein operators. In more recent times, generalized sampling theory is a popular subject in approximation theory owing to its great variety of applications, especially in image and signal processing.

In this study, computational solutions of integral equations, which are crucial application areas in several disciplines, are given by making use of the superior features of the generalized sampling theorem. Additionally, we show the applicability and efficiency of the proposed technique both theoretically and numerically. Of course, this work is not a completely new methodology or a new method for the numerical solution of integral equations. However, in the light of existing collocation methods such as projection methods [23, pp. 49-50] which uses the basis functions and unknown constants, it is presented to the attention of the readers as a different alternative. Besides, using the nonideal instantaneous sampling theory and Fourier analysis, another work in

[24] presents a new methodology to solve Fredholm integral equations. In this context, one can argue that the presented technique is the first time that the generalized sampling theory is used to solve Volterra integral equations and can be readily generalized in that direction.

The contents of the article consist of five sections with this section. **Section 2** discusses the preliminaries of both integral equations and the generalized sampling theorems. **Section 3** explains the construction of the proposed method for the numerical solution of various integral equations via the proposed method. **Section 4** provides several computational experiment results to validate the presented technique. Finally, **Section 5** summarizes the paper by adding some conclusions and further research.

## 2 Fundamental facts

In this section, we review some fundamental definitions and theorems that we will benefit from the construction of the proposed method. Therefore, it would be more favorable to give them in two parts systematically.

### Integral equations

As mentioned in the previous sections, it will be useful for us to categorize the integral equations. Since we focus on Volterra and Abel integral equations in this study, it will be sufficient to provide general information about them. For detailed information on other types of integral equations such as Fredholm integral equations, we refer the reader to [25–29].

The standard form of the integral equation is

$$\psi(\eta)\phi(\eta) = \varphi(\eta) + \lambda \int_{\vartheta(\eta)}^{\mu(\eta)} \mathcal{K}(\eta, \xi)\phi(\xi)d\xi, \quad (1)$$

where  $\mathcal{K}(\eta, \xi)$  is a bivariate known kernel,  $\psi(\eta)$  and  $\varphi(\eta)$  are known functions,  $\vartheta(\eta)$ ,  $\mu(\eta)$  are integration limits,  $\lambda$  is a non-zero real or complex parameter and  $\phi(\eta)$  is unknown function needs to be determined. The classical form of Volterra integral equations is [30],

$$\psi(\eta)\phi(\eta) = \varphi(\eta) + \lambda \int_a^\eta \mathcal{K}(\eta, \xi)\phi(\xi)d\xi, \quad a \leq \xi \leq \eta \leq b, \quad [a, b] \subset (-\infty, \infty). \quad (2)$$

On the other hand, when at least one of the limits of integration in an integral equation becomes infinite or when the bivariate kernel of an integral equation becomes infinite at one or more points within the range of integration, in this case, the integral equation is called as a singular integral equation. One of them is Abel integral equation and it is given as follows for  $\eta > 0$ :

$$\frac{1}{\Gamma(\alpha)} \int_a^\eta \frac{1}{(\eta - \xi)^{1-\alpha}} \phi(\xi)d\xi = \varphi(\eta), \quad a \leq \xi \leq \eta \leq b, \quad [a, b] \subset (-\infty, \infty), \quad (3)$$

where  $\Gamma(\cdot)$  is Gamma function defined by  $\Gamma(\alpha) = \int_0^\infty \eta^{\alpha-1} e^{-\eta} d\eta$ , and  $\alpha \in (0, 1)$  [31].

### Generalized sampling operators

Butzer and his students introduced the theory of generalized sampling operators at RWTH Aachen in the late 1970s. Then it turned out that this study was very interesting both in terms of theory and practice. Before summarizing generalized sampling operators, readers who want to get detailed information on this topic can refer to the following studies [19–22, 32].

A generalized sampling operators generated by a suitable kernel function  $\chi \in L^1(\mathbb{R}) \cap C(\mathbb{R})$  is defined for a uniformly continuous and bounded functions  $\phi \in C(\mathbb{R})$  as follows:

$$\left(\mathcal{S}_w^\chi \phi\right)(\eta) = \sum_{k=-\infty}^{\infty} \phi\left(\frac{k}{w}\right) \chi(w\eta - k), \quad (4)$$

for  $\eta \in \mathbb{R}$  and  $w > 0$ . It is worth noting that the values  $\phi(k/w)_{k=-\infty}^{\infty}$  are called sampled values taken at the nodes  $k/w$  for  $k \in \mathbb{Z}$ , which are a uniform grid on  $\mathbb{R}$ . Additionally, the generalized sampling operators are well-defined when the following conditions are held for any  $s \in \mathbb{R}$ :

$$\sum_{k=-\infty}^{\infty} |\chi(s - k)| < \infty,$$

the absolute convergence being uniform on compact subsets of  $\mathbb{R}$ , and

$$\sum_{k=-\infty}^{\infty} \chi(s - k) = 1.$$

In addition to these facts, one can say that  $\mathcal{S}_w^\chi$  are linear and bounded operators mapping  $C(\mathbb{R})$  into itself, having the operator norm

$$\|\mathcal{S}_w^\chi\|_{[C(\mathbb{R}), C(\mathbb{R})]} = \sup_{s \in \mathbb{R}} \sum_{k \in \mathbb{Z}} |\chi(s - k)|,$$

and

$$\lim_{w \rightarrow \infty} \|\mathcal{S}_w^\chi \phi - \phi\|_{C(\mathbb{R})} = 0.$$

Recently, a number of progressions were observed for the development of the generalized sampling operators, focusing on certain aspects of both theory and applications. In more detail, in [33], the authors considered a new definition of generalized sampling type series utilizing an approach defined by Durrmeyer for the Bernstein polynomials. On the other hand, in [34], the authors introduced appropriate linear combinations for a multivariate version of the generalized sampling series. Both studies provide a better order of approximation theoretically proved. Along with these, in [35], the authors proposed some solutions to solve the problems encountered in real-life signal processing.

One of the most significant generalizations of the generalized sampling theorem is sampling Kantorovich operators which use the integral mean of  $\phi$  on small intervals around the sample nodes in place of the exact value of the function at these nodes, [36–39]. In other words, the sampling Kantorovich operators can be obtained by replacing the sampled values with the Steklov mean of  $f$  on the interval  $[k/w, (k+1)/w]$ , which is,

$$\bar{\phi}\left(\frac{k}{w}\right) = w \int_{k/w}^{(k+1)/w} \phi(s) ds.$$

This is a point where the sampling Kantorovich operators are bounded in  $L^p(\mathbb{R})$ , and also, as a

general idea, in Orlicz spaces, under classical singularity presumptions on the kernel  $\chi$ .

In recent times, the asymptotic behaviour of the generalized sampling operators has been studied, which yields precise estimates of the pointwise and uniform convergence of these operators to  $\phi$  [33, 40, 41]. Particularly, in [41], the Voronovskya type formula for the generalized sampling operators, under appropriate singularity presumptions on the kernel function  $\chi$ , has been given as follows for at least twice differentiable function  $\phi$  at the point  $\eta$ ,

$$\lim_{w \rightarrow \infty} w^2 \left[ \left( \mathcal{J}_w^\chi \phi \right) (\eta) - \phi(\eta) \right] = \mathcal{A}_\chi \phi''(\eta), \quad (5)$$

where  $\mathcal{A}_\chi$  is an absolute constant depending only on  $\chi$ .

### 3 Construction of the numerical method

In this part, we construct a numerical scheme to find a numerical solution to the second and the first kind Volterra integral equations and Abel integral equations with the presented method. In line with this objective, we use the truncated type operators. In other words, whenever the operators (4) converge, for the positive integer  $N$ ,  $f$  can be approximated by,

$$\left( \mathcal{J}_w^{\chi, N} \phi \right) (\eta) = \sum_{k=-N}^N \phi \left( \frac{k}{w} \right) \chi(w\eta - k). \quad (6)$$

Thus one can find the approximate solution of given integral equations for the arbitrary interval. Throughout this and the next sections, we take the integral equations defined in  $\tilde{I} := [a, b]$  such that  $-\infty < a \leq \eta \leq b < \infty$ .

#### Numerical scheme for the second kind Volterra integral equations

So as to solve the second kind Volterra integral equations, firstly, we approximate the unknown function in (2) via (6) as follows:

$$\phi(\eta) \simeq \mathcal{J}_w^{\chi, N}(\phi(\eta)) = \sum_{k=-N}^N \phi \left( \frac{k}{w} \right) \chi(w\eta - k), \quad (7)$$

for properly selected kernel  $\chi$ . Then substituting (7) into (2) in case of  $\psi(\eta) = 1$ , one readily deduces the following equation, that is to say

$$\mathcal{J}_w^{\chi, N}(\phi(\eta)) = \phi(\eta) + \lambda \int_a^\eta \mathcal{K}(\eta, \xi) \mathcal{J}_w^{\chi, N}(\phi(\xi)) d\xi, \quad \eta \in \tilde{I}, \quad (8)$$

which yields

$$\sum_{k=-N}^N \phi \left( \frac{k}{w} \right) \chi(w\eta - k) = \phi(\eta) + \lambda \int_a^\eta \mathcal{K}(\eta, \xi) \sum_{k=-N}^N \phi \left( \frac{k}{w} \right) \chi(w\xi - k) d\xi.$$

The point to note here is that it is possible to benefit the interchangeability properties of the integral and the sum by using the result that the generalized sampling operators are uniformly convergent,

proved in [42]. Thereupon by re-composition the above equation, we deduce that

$$\varphi(\eta) = \sum_{k=-N}^N \phi\left(\frac{k}{w}\right) \left[ \chi(w\eta - k) - \lambda \int_a^\eta \mathcal{K}(\eta, \xi) \chi(w\xi - k) d\xi \right].$$

The point to be noted here is that we ignore the endpoints of the approximation interval which compute the solution in order to avoid the singularity issue by manipulating the endpoints with any arbitrary small number  $\varepsilon$ . In addition, we need to replace  $\eta$  with  $\eta_l = l/w + \varepsilon$ , for  $l = -N, \dots, N$  before calculating the unknown coefficients  $f(k/w)$ . That is,

$$\varphi(\eta_l) = \sum_{k=-N}^N \phi\left(\frac{k}{w}\right) \left[ \chi(w\eta_l - k) - \lambda \int_a^{\eta_l} \mathcal{K}(\eta_l, \xi) \chi(w\xi - k) d\xi \right].$$

This equation can be expressed in the matrix form as follows:

$$[\mathbf{P}][\mathbf{X}] = [\mathbf{S}],$$

where

$$[\mathbf{P}] = \left[ \chi(w\eta_l - k) - \lambda \int_a^{\eta_l} \mathcal{K}(\eta_l, \xi) \chi(w\xi - k) d\xi \right]_{(2N+1) \times (2N+1)}, \quad l, k = -N, \dots, N, \quad (9)$$

$$[\mathbf{S}] = \left[ \varphi(\eta_{-N}), \varphi(\eta_{-N+1}), \dots, \varphi(\eta_{N-1}), \varphi(\eta_N) \right]_{(2N+1) \times 1}^T, \quad (10)$$

$$[\mathbf{X}] = \left[ \phi(-N/w), \phi((-N+1)/w), \dots, \phi((N-1)/w), \phi(N/w) \right]_{(2N+1) \times 1}^T. \quad (11)$$

---

**Algorithm 1:** Generalized sampling operators method for solving second kind Volterra integral equations

---

**Input:**  $\eta_l, l = -N \dots, N$

```

1 for  $i \leftarrow -N$  to  $N$  do
2   for  $k \leftarrow -N$  to  $N$  do
3     Compute  $[\mathbf{P}]_{(2N+1) \times (2N+1)}$ 
4   end
5 end
6 Calculate  $[\mathbf{P}^{-1}]$ 
7 for  $k \leftarrow -N$  to  $N$  do
8   Compute  $[\mathbf{S}]_{(2N+1) \times (2N+1)}$ 
9 end
10 Calculate  $[\mathbf{X}] = [\mathbf{P}^{-1}][\mathbf{S}]$ .
```

**Output:** Compute  $\sum_{k=-N}^N \phi\left(\frac{k}{w}\right) \chi(w\eta - k)$ , using  $[\mathbf{X}]$ .

---

The matrix equation  $[\mathbf{P}][\mathbf{X}] = [\mathbf{S}]$  can be computed as long as the matrix  $[\mathbf{P}]$  must be an invertible matrix. Then, to do this it is necessary to compute the matrix  $[\mathbf{P}]$  and the vector  $[\mathbf{S}]$  as an initial act. Then, one can easily deduce the matrix  $[\mathbf{X}]$  utilizing  $[\mathbf{X}] = [\mathbf{P}^{-1}][\mathbf{S}]$ . Finally, the approximate

solution of the second kind Volterra integral equation can be obtained by substituting the matrix  $[X]$  in Eq. (7). Now we summarize the algorithm of the presented method above.

**Numerical scheme for the first kind Volterra integral equations**

Now we use (2) to obtain the first kind Volterra integral equations in case of  $\psi(\eta) = 0$ . Then if we approximate the unknown function  $\phi_w(\eta)$  with (7), we obtain the following equality,

$$\phi(\eta) = \int_a^\eta \mathcal{K}(\eta, \xi) \mathcal{I}_w^{\chi, N}(\phi(\xi)) d\xi, \quad \eta \in \tilde{I}. \tag{12}$$

By following the similar steps in the previous subsection, a method for numerical solution of the first kind Volterra integral equations via generalized sampling operators can be developed. The matrix equation obtained here in this circumstance is,

$$[R][X] = [S],$$

where

$$[R] = \left[ \int_a^{\eta_l} \mathcal{K}(\eta_l, \xi) \chi(w\xi - k) d\xi \right]_{(2N+1) \times (2N+1)}, \quad l, k = -N, \dots, N, \tag{13}$$

and the vectors  $[S]$  and  $[X]$  given in Eq. (10) and Eq. (11), respectively. Similarly, we need to compute the matrix  $[R]$  and the vector  $[S]$  as a beginning. Then, one can smoothly deduce the matrix  $[X]$  with the help of  $[X] = [R^{-1}][S]$ . In the end, the approximate solution of the first kind of Volterra integral equation can be deduced by substituting the matrix  $[X]$  in Eq. (7).

**Numerical scheme for the Abel’s integral equations**

In this subsection, we provide a numerical scheme for the numerical solution of Abel’s integral equation with the proposed method. For this purpose, we approximate the unknown function in (3) via (6), which yields

$$\frac{1}{\Gamma(\alpha)} \int_a^\eta \frac{1}{(\eta - \xi)^{1-\alpha}} \mathcal{I}_w^{\chi, N}(\phi(\xi)) d\xi = \phi(\eta), \quad \eta \in \tilde{I}.$$

Then this equality gives us the following equation,

$$\phi(\eta_l) = \sum_{k=-N}^N \phi\left(\frac{k}{w}\right) \left[ \frac{1}{\Gamma(\alpha)} \int_a^{\eta_l} \frac{1}{(\eta_l - \xi)^{1-\alpha}} \chi(w\xi - k) d\xi \right],$$

where  $l = -N, \dots, N$ . Ultimately, this equation can be converted to a matrix equation, that is

$$[K][X] = [S],$$

where

$$[K] = \left[ \frac{1}{\Gamma(\alpha)} \int_a^{\eta_l} \frac{1}{(\eta_l - \xi)^{1-\alpha}} \chi(w\xi - k) d\xi \right]_{(2N+1) \times (2N+1)}, \quad l, k = -N, \dots, N, \tag{14}$$

and the vectors  $[S]$  and  $[X]$  given in Eq. (10) and Eq. (11), respectively.

**Remark 1** It is possible to write an algorithm similar to Algorithm 1, where only the content of the matrix  $[P]$  will change and the matrices  $[S]$  and  $[K]$  will be replaced by it for the first kind Volterra and Abel's integral equations, respectively.

It is noted that we can show  $\phi(k/w)$ ,  $k = -N, \dots, N$  by  $\phi_w(k/w)$ ,  $k = -N, \dots, N$  that are our solution in nodes  $k/w$ ,  $k = -N, \dots, N$  and by substituting them in Eq. (6), we can find  $\mathcal{S}_w^{\lambda, N}(\phi_w(\eta_k))$ ,  $k = -N, \dots, N$  that is the proposed method solution for the integral equation.

#### 4 Numerical examples

In this section of this paper, three numerical examples are provided and tested to demonstrate the practicability and accuracy of the proposed method. The first example is related to the second kind Volterra integral equations, the second example is related to the first kind Volterra integral equations, and the last one related to Abel's integral equation. In all examples the package of *MATLAB 2020a* has been used to implement the algorithm to calculate numerical solution of the test equations considered in this study. The error is reported on the following grid points

$$\rho = \{\eta_{-N}, \dots, \eta_N\}, \quad \eta_l = l/w \quad l = -N, \dots, N.$$

In addition to these, we set the following notations to analyze the error of the proposed method:

$$E_w(\eta) = |\phi(\eta) - \mathcal{S}_w^{\lambda, N}(\phi_w(\eta))|,$$

and

$$\|E_w\|_\infty = \max\{E_w(\eta_l), l = -N, \dots, N\},$$

where  $\phi(\eta)$  and  $\mathcal{S}_w^{\lambda, N}(\phi_w(\eta))$  are exact solution and approximate solution of the test integral equations respectively and  $\eta_l$  are the uniform grids on  $\tilde{I}$ . Moreover, we summarize the root mean square error as follows i.e.

$$RMSE = \sqrt{\frac{\sum_{l=-N}^N [\phi(\eta_l) - \mathcal{S}_w^{\lambda, N}(\phi_w(\eta_l))]^2}{2N + 1}}.$$

*Time* represents the CPU time consumed in each numerical examples. Moreover, we summarize the root mean square error with RMSE.

##### Example 1

For the following second kind Volterra integral equation, we take the following equation,

$$\phi(\eta) = e^{-\eta^2} - \frac{1}{2} \left( \frac{1}{e} - e^{-\eta^2} \right) \eta + \int_{-1}^{\eta} \eta \xi \phi(\xi) d\xi, \quad \text{on } \tilde{I},$$

with the exact solution  $\phi(\eta) = e^{-\eta^2}$  on  $\tilde{I} = [-1, 1]$ . In this example,  $\varphi(\eta) = e^{-\eta^2} - \frac{1}{2} \left( \frac{1}{e} - e^{-\eta^2} \right) \eta$ ,  $\mathcal{K}(\eta, \xi) = \eta \xi$  and  $\lambda = 1$ .

Additionally, for this experiment we use the univariate Fejer kernel defined by

$$\chi(\eta) = \frac{1}{2} \operatorname{sinc}^2\left(\frac{\eta}{2}\right),$$

for  $\eta \in \mathbb{R}$ , where the sinc function is given by

$$\operatorname{sinc}(\eta) := \begin{cases} \frac{\sin(\pi\eta)}{\pi\eta}, & \text{if } \eta \in \mathbb{R} - \{0\}, \\ 1, & \text{if } \eta = 0. \end{cases}$$

In [Figure 1](#), the Fejer kernel can be shown.

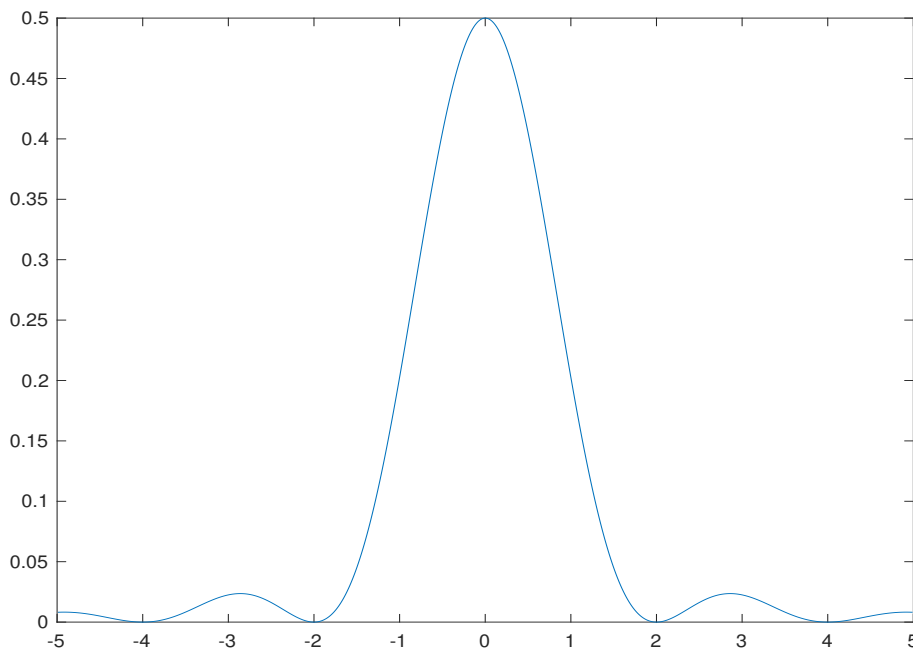


**Figure 1.** The univariate Fejer kernel  $\chi(\eta)$

Thus, we have the following generalized sampling operator by substituting univariate Fejer kernel to (6), that is to say

$$\left(\mathcal{J}_w^{\chi, N} \phi\right)(\eta) = \frac{1}{2} \sum_{k=-N}^N \phi\left(\frac{k}{w}\right) \operatorname{sinc}^2\left(\frac{w\eta - k}{2}\right).$$

In [Table 1](#), numerical results of solution of the second kind Volterra integral equation which obtained by the proposed technique are presented. These results confirm that the proposed method is an approximation process for the second kind Volterra integral equation. In addition to this, in [Figure 2](#), computational solution and exact solution of test problem have been provided. This graph shows the convergence properties of the presented method as well.

**Table 1.**  $\|E_w\|_\infty$ , RMSE and Time for the numerical solution of the second kind integral equation, with  $\varepsilon = 0.01$ , on equally spaced grid on  $\tilde{I}$

N	Proposed method		
	$\ E_n\ _\infty$	RMSE	Time
5	1.295605e-03	6.074132e-04	< 1
10	1.189609e-03	4.919707e-04	< 1
25	6.622351e-04	2.514840e-04	< 1
50	3.686320e-04	1.357361e-04	< 1
100	1.944992e-04	7.046801e-05	3.483948
150	1.320756e-04	4.759612e-05	6.669202
200	9.986052e-05	3.592332e-05	11.948382

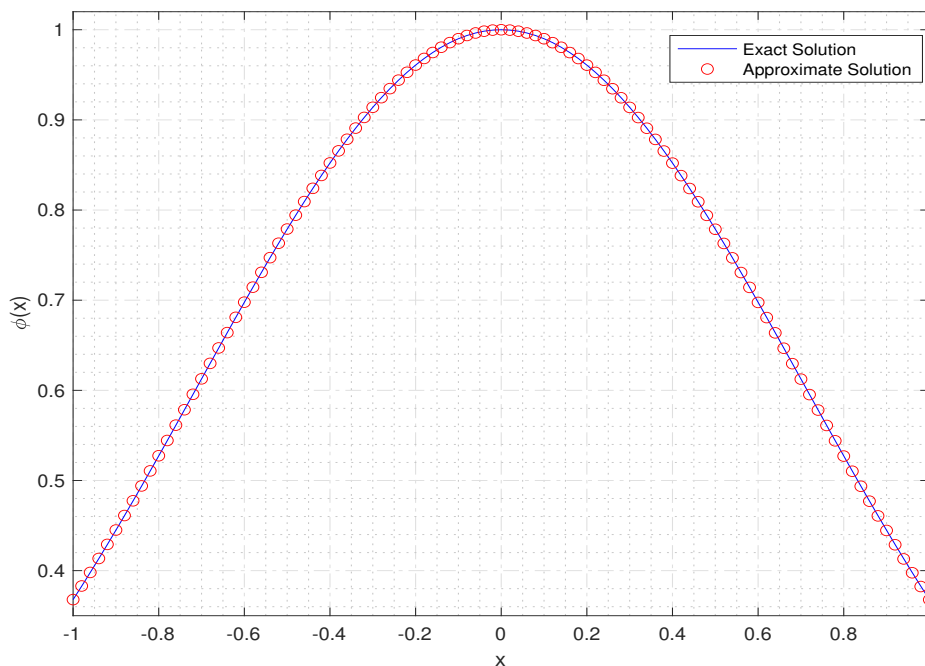


**Figure 2.** While the blue line represents the exact solution, the red squares represent the proposed method. The figure illustrates the accuracy of the proposed method

### Example 2

In this example, we solve the first kind Volterra integral equation numerically. For that, we take the following equation,

$$-\sin(\eta) - \cos(\eta) + e^{\eta+2}(\cos(2) - \sin(2)) = \int_{-2}^{\eta} 2e^{\eta-\xi} \phi(\xi) d\xi, \text{ on } \tilde{I},$$

with the exact solution  $\phi(\eta) = \sin(\eta)$  on  $\tilde{I} = [-2, 2]$ . In this example,  $\varphi(\eta) = -\sin(\eta) - \cos(\eta) + e^{\eta+2}(\cos(2) - \sin(2))$  and  $\mathcal{K}(\eta, \xi) = 2e^{\eta-\xi}$ . Moreover, for this experiment we use the univariate Blackman-Harris kernel defined by

$$\chi(\eta) = \frac{1}{2} \text{sinc}(\eta) + \frac{9}{32} (\text{sinc}(\eta + 1) + \text{sinc}(\eta - 1)) - \frac{1}{32} (\text{sinc}(\eta + 3) + \text{sinc}(\eta - 3)),$$

for  $\eta \in \mathbb{R}$ , where the sinc function defined above. In Figure 3, the Blackman-Harris kernel can be seen.

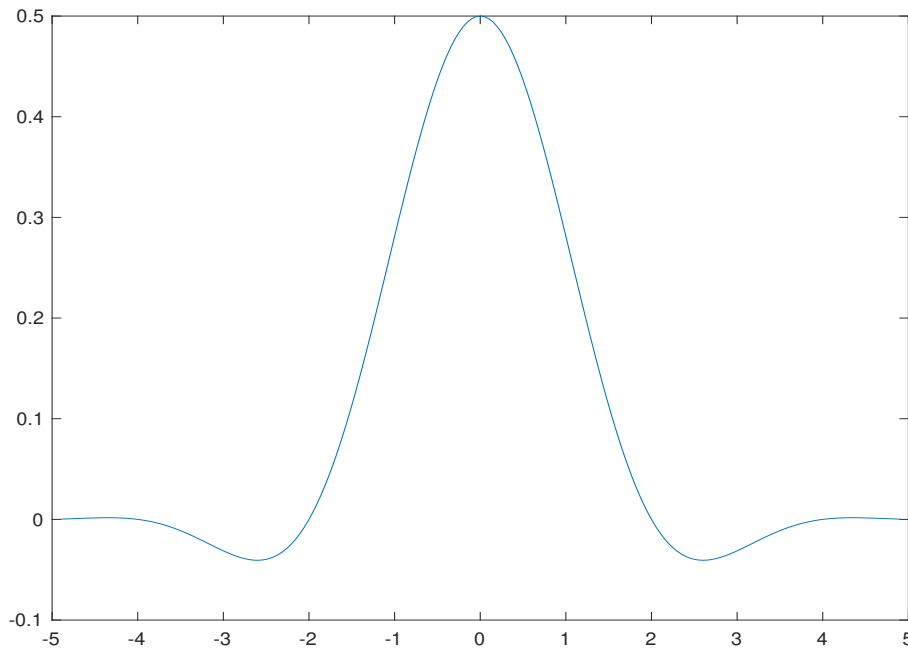


**Figure 3.** The univariate Blackman-Harris kernel  $\chi(\eta)$

Thus, we have the following generalized sampling operator by substituting univariate Blackman-Harris kernel to (6), that is to say

$$\begin{aligned} \left( \mathcal{J}_w^{\chi, N} \phi \right) (\eta) = & \sum_{k=-N}^N \phi \left( \frac{k}{w} \right) \left[ \frac{1}{2} \operatorname{sinc}(w\eta - k) + \frac{9}{32} (\operatorname{sinc}(w\eta - k + 1) + \operatorname{sinc}(w\eta - k - 1)) \right. \\ & \left. - \frac{1}{32} (\operatorname{sinc}(w\eta - k + 3) + \operatorname{sinc}(w\eta - k - 3)) \right]. \end{aligned}$$

In Table 2, numerical results of the solution of the first kind Volterra integral equation which computed by the proposed method are presented. These results confirm the approximation properties of the presented method. In addition to this, in Figure 4, computational solution and exact solution of test problem have been provided. This graph also shows the convergence properties of the presented method.

**Table 2.**  $\|E_w\|_\infty$ , RMSE and Time for the numerical solution of the second kind integral equation, on equally spaced grid on  $\tilde{I}$

N	Proposed method		
	$\ E_n\ _\infty$	RMSE	Time
5	5.619397e-02	1.270206e-02	< 1
10	3.012573e-02	5.103643e-03	< 1
15	1.384453e-02	2.111580e-03	< 1
20	4.580176e-03	8.216078e-04	< 1

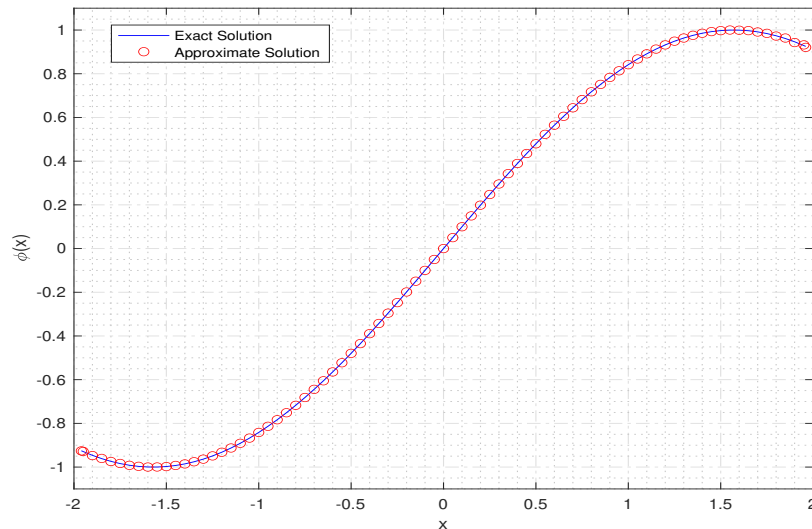


**Figure 4.** Numerical solution of the first kind Volterra integral equation via generalized sampling operators method. While the blue line represents the exact solution, the red squares represent the proposed method. The figure illustrates the accuracy of the proposed method

### Example 3

Finally, we present a numerical example for the Abel’s integral equation which is

$$\frac{4}{15} \sqrt{\eta + 1} (4\eta^2 - 2\eta + 9) = \int_{-1}^{\eta} \frac{1}{\sqrt{\eta - \xi}} \phi(\xi) d\xi, \text{ on } \tilde{I},$$

with the exact solution  $\phi(\eta) = \eta^2 + 1$  on  $\tilde{I} = [-1, 1]$ . In this example,  $\varphi(\eta) = \frac{4}{15} \sqrt{\eta + 1} (4\eta^2 - 2\eta + 9)$ . Moreover, we use the univariate Blackman-Harris kernel for this example.

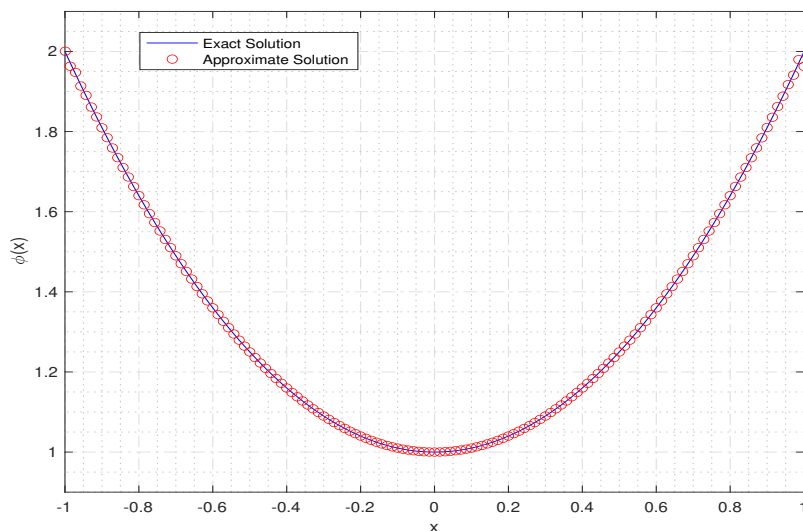


**Figure 5.** While the blue line represents the exact solution, the red squares represent the proposed method. The figure illustrates the accuracy of the proposed method

In **Figure 5**, we can observe how the proposed method converges the exact solution of Abel's integral equations.

The three numerical examples given above show that the generalized sampling operators method can be an alternative to other computational methods for numerical solutions of integral equations.

## 5 Concluding remarks

In this paper, we have proposed and tested a numerical scheme to solve integral equations utilizing generalized sampling operators. For this, firstly, we construct the numerical scheme for the solution. Then we provide the convergence analysis of the proposed method with the aid of Voronovskaya type formula for the generalized sampling operators. Finally, in order to validate our theoretical result, we present some numerical experiments with different kernels.

## Declarations

### Use of AI tools

The author declares that he has not used Artificial Intelligence (AI) tools in the creation of this article.

### Data availability statement

All data generated or analyzed during this study are included in this article.

### Ethical approval (optional)

The author states that this research complies with ethical standards. This research does not involve either human participants or animals.

### Consent for publication

Not applicable

### Conflicts of interest

The author declares that he has no conflict of interest.

### Funding

No funding

### Author's contributions

The author has read and agreed to the published version of the manuscript.

### Acknowledgements

Not applicable

## References

- [1] Archibald, T. and Tazzioli, R. Integral equations between theory and practice: the cases of Italy and France to 1920. *Archive for History of Exact Sciences*, 68, 547-597, (2014). [[CrossRef](#)]
- [2] Abel, N.H. Aufloesung einer mechanischen Aufgabe. *Journal für die Reine und Angewandte Mathematik (Crelle)*, 1, 153-157, (1826). [[CrossRef](#)]
- [3] Gorenflo, R. and Mainardi, F. *Fractional Calculus: Integral and Differential Equations of Fractional Order*. Springer: Vienna, (1997).

- [4] Moiseiwitsch, B.L. *Integral Equations*. Longman: London and New York, (1977).
- [5] Babolian, E. and Davari, A. Numerical implementation of Adomian decomposition method for linear Volterra integral equations of the second kind. *Applied Mathematics and Computation*, 165, 223-227, (2005). [[CrossRef](#)]
- [6] Izadian, J., Salahshour, S. and Soheil, S. A numerical method for solving Volterra and Fredholm integral equations using homotopy analysis method. *AWER Procedia Information Technology & Computer Science*, 1, 406-411, (2012).
- [7] Rashidinia, J. and Zarebnia, M. Solution of a Volterra integral equation by the Sinc-collocation method. *Journal of Computational and Applied Mathematics*, 206(2), 801-813, (2007). [[CrossRef](#)]
- [8] Atkinson, K.E. *The Numerical Solution of Integral Equations of the Second Kind* (Vol. 4). Cambridge University Press: England, (1997).
- [9] Maleknejad, K. and Aghazadeh, N. Numerical solution of Volterra integral equations of the second kind with convolution kernel by using Taylor-series expansion method. *Applied Mathematics and Computation*, 161(3), 915–922, (2005). [[CrossRef](#)]
- [10] Maleknejad, K., Tavassoli Kajani, M. and Mahmoudi, Y. Numerical solution of linear Fredholm and Volterra integral equation of the second kind by using Legendre wavelets. *Kybernetes*, 32(9/10), 1530–1539, (2003). [[CrossRef](#)]
- [11] Maleknejad, K., Mollapourasl, R. and Alizadeh, M. Numerical solution of Volterra type integral equation of the first kind with wavelet basis. *Applied Mathematics and Computation*, 194(2), 400-405, (2007). [[CrossRef](#)]
- [12] Shoukralla, E.S. and Markos, M.A. The economized monic Chebyshev polynomials for solving weakly singular Fredholm integral equations of the first kind. *Asian-European Journal of Mathematics*, 13(01), 2050030, (2020). [[CrossRef](#)]
- [13] Wang, W. A mechanical algorithm for solving the Volterra integral equation. *Applied Mathematics and Computation*, 172(2), 1323-1341, (2006). [[CrossRef](#)]
- [14] Maleknejad, K., Hashemizadeh, E. and Ezzati, R. A new approach to the numerical solution of Volterra integral equations by using Bernstein's approximation. *Communications in Nonlinear Science and Numerical Simulation*, 16(2), 647–655, (2011). [[CrossRef](#)]
- [15] Usta, F., İlkan, M. and Kara, E.E. Numerical solution of Volterra integral equations via Szász-Mirakyan approximation method. *Mathematical Methods in the Applied Sciences*, 44(9), 7491-7500, (2021). [[CrossRef](#)]
- [16] Usta, F. Numerical analysis of fractional Volterra integral equations via Bernstein approximation method. *Journal of Computational and Applied Mathematics*, 384, 113198, (2021). [[CrossRef](#)]
- [17] Usta, F. Bernstein Approximation technique for numerical solution of Volterra integral equations of the third kind. *Computational and Applied Mathematics*, 40, 161, (2021). [[CrossRef](#)]
- [18] Acar, T., Cappelletti Montano, M., Garrancho, P. and Leonessa, V. On sequence of J. P. King type operators. *Journal of Function Spaces*, 2019, 2329060, (2019). [[CrossRef](#)]
- [19] Butzer, P.L. and Stens, R.L. Sampling theory for not necessarily band-limited functions: a historical overview. *SIAM Review*, 34(1), 40-53, (1992). [[CrossRef](#)]
- [20] Butzer, P.L., Fischer, A. and Stens, R.L. Generalized sampling approximation of multivariate signals: general theory. *Atti Sem. Mat. Fis. Univ. Modena*, 41(1), 17-37, (1993). [[CrossRef](#)]
- [21] Butzer, P.L., Ries, S. and Stens, R.L. Approximation of continuous and discontinuous functions by generalized sampling series. *Journal of Approximation Theory*, 50, 25-39, (1987). [[CrossRef](#)]

- 
- [22] Butzer, P.L. and Stens, R.L. Prediction of non-bandlimited signals from past samples in terms of splines of low degree. *Mathematische Nachrichten*, 132(1), 115-130, (1987). [[CrossRef](#)]
- [23] Atkinson, K.E. *The Numerical Solution of Integral Equations of the Second Kind*, Cambridge University Press: Cambridge, (1997).
- [24] Paez-Rueda, C.I. and Bustamante-Miller, R. Novel computational approach to solve convolutional integral equations: method of sampling for one dimension, *Pontificia Universidad Javeriana: Engineering for Development*, 23(2), 1-32, (2019). [[CrossRef](#)]
- [25] Wazwaz, A.M. *A First Course in Integral Equations*, World Scientific: Singapore, (1997).
- [26] Ansari, K.J., Sessa, S. and Alam, A. A class of relational functional contractions with applications to nonlinear integral equations. *Mathematics*, 11(15), 3408, (2023). [[CrossRef](#)]
- [27] Say, F. Asymptotics of singularly perturbed Volterra type integro-differential equation. *Konuralp Journal of Mathematics*, 8(2), 365-369, (2020).
- [28] Wang, Q. and Zhou, H. Two-grid iterative method for a class of Fredholm functional integral equations based on the radial basis function interpolation. *Fundamental Journal of Mathematics and Applications*, 2(2), 117-122, (2019). [[CrossRef](#)]
- [29] Zhou, H., Wang, Q. The Nyström method and convergence analysis for system of Fredholm integral equations. *Fundamental Journal of Mathematics and Applications*, 2(1), 28-32, (2019). [[CrossRef](#)]
- [30] Shestopalov, Y.V. and Smirnov, Y.G. *Integral Equations*. Karlstad University, 2002.
- [31] S. G. Samko, A. A. Kilbas, O. I. Marichev, *Fractional Integrals and Derivatives Theory and Applications*, Amsterdam: Gordon and Breach Science Publishers, 1993.
- [32] P.L. Butzer, W. Splettstößer, R.L. Stens, *The sampling theorem and linear prediction*, Jahresberichte Dt. Math.-Verein, 90 (1988), 1-70.
- [33] Bardaro, C. and Mantellini, I. Asymptotic expansion of generalized Durrmeyer sampling type series. *Jaen Journal on Approximation*, 6(2), 143-165, (2014).
- [34] Bardaro, C. and Mantellini, I. On linear combinations of multivariate generalized sampling type series. *Mediterranean Journal of Mathematics*, 10, 1833-1852, (2013). [[CrossRef](#)]
- [35] Bardaro, C., Butzer, P.L., Stens, R.L. and Vinti, G. Prediction by samples from the past with error estimates covering discontinuous signals. *IEEE Transactions on Information Theory*, 56(1), 614-633, (2010). [[CrossRef](#)]
- [36] Bardaro, C., Vinti, G., Butzer, P.L. and Stens, R. Kantorovich-type generalized sampling series in the setting of Orlicz spaces. *Sampling Theory in Signal and Image Processing*, 6, 29-52, (2007). [[CrossRef](#)]
- [37] Costarelli, D. and Vinti, G. Approximation by multivariate generalized sampling Kantorovich operators in the setting of Orlicz spaces. *Bollettino dell'Unione Matematica Italiana*, 4(3), 445-468, (2011).
- [38] Costarelli, D. and Vinti, G. Approximation by nonlinear multivariate sampling Kantorovich type operators and applications to image processing. *Numerical Functional Analysis and Optimization*, 34(8), 819-844, (2013). [[CrossRef](#)]
- [39] Costarelli, D. and Vinti, G. Degree of approximation for nonlinear multivariate sampling Kantorovich operators on some function spaces. *Numerical Functional Analysis and Optimization*, 36(8), 964- 990, (2015). [[CrossRef](#)]
- [40] Bardaro, C. and Mantellini, I. Asymptotic formulae for linear combinations of generalized

- sampling operators. *Zeitschrift für Analysis und ihre Anwendungen*, 32, 279-298, (2013). [[CrossRef](#)]
- [41] Bardaro, C. and Mantellini, I. A quantitative Voronvoskaja formula for generalized sampling operators. *East Journal on Approximations*, 15(4), 459-471, (2009).
- [42] Bardaro, C. and Vinti, G. Uniform convergence and rate of approximation for a nonlinear version of the generalized sampling operator. *Results in Mathematics*, 34, 224-240, (1998). [[CrossRef](#)]

Mathematical Modelling and Numerical Simulation with Applications (MMNSA)  
(<https://dergipark.org.tr/en/pub/mmnsa>)



**Copyright:** © 2024 by the authors. This work is licensed under a Creative Commons Attribution 4.0 (CC BY) International License. The authors retain ownership of the copyright for their article, but they allow anyone to download, reuse, reprint, modify, distribute, and/or copy articles in MMNSA, so long as the original authors and source are credited. To see the complete license contents, please visit (<http://creativecommons.org/licenses/by/4.0/>).

**How to cite this article:** Usta, F. (2024). Approximate solution of integral equations based on generalized sampling operators. *Mathematical Modelling and Numerical Simulation with Applications*, 4(2), 149-164. <https://doi.org/10.53391/mmnsa.1487545>



RESEARCH PAPER

## An approach to stochastic differential equations for long-term forecasting in the presence of $\alpha$ -stable noise: an application to gold prices

Bakary D. Coulibaly <sup>1,\*</sup>, Chaibi Ghizlane <sup>1,†</sup> and Mohammed El Khomssi <sup>1,‡</sup>

<sup>1</sup>Department of Mathematics, Laboratory of Modeling and Mathematical Structures, Sidi Mohamed Ben Abdellah University, Route d'Ilmouzzar, 30000 Fez, Morocco

\* Corresponding Author

‡ bakocly@gmail.com (Bakary D. Coulibaly); ghizlane.chaibi@usmba.ac.ma (Chaibi Ghizlane); khomsixmath@yahoo.fr (Mohammed El Khomssi)

### Abstract

This article introduces a novel approach to forecasting gold prices over an extended period by leveraging a sophisticated stochastic process. Departing from traditional models, our proposed framework accommodates the non-Gaussian and non-homogeneous nature of gold market dynamics. Rooted in the  $\alpha$ -stable distribution, our model captures time-dependent characteristics and exhibits flexibility in handling the distinctive features observed in real gold prices. Building upon prior research, we present a comprehensive methodology for estimating time-dependent parameters and validate its efficacy through simulations. The results affirm the universality of our stochastic model, showcasing its applicability for accurate and robust long-term predictions in gold prices.

**Keywords:** Stochastic differential equation; modeling  $\alpha$ -stable distribution; parameters estimation; forecasting; gold prices; long-term prediction

**AMS 2020 Classification:** 60G15; 60G52; 60J65; 62M10

### 1 Introduction

Forecasting metal prices poses a significant challenge due to their intricate dependencies. The volatility and unpredictability of metal prices stem not only from fundamental factors such as supply-demand dynamics but also from macroeconomic conditions and investor sentiment. For mining companies, price assumptions are crucial not only for estimating revenue streams from metal sales but also for determining the optimal extraction plan in mines. This extraction plan forms the foundation for the entire budgeting and planning process. In the mining industry,

forecasting extends beyond the short term and focuses on a horizon spanning several years, adding complexity to the task. Employing stochastic modeling proves invaluable in comprehensively gauging and understanding the magnitude and likelihood of potential price movements. This becomes a pivotal undertaking for companies, enabling them to formulate effective business strategies in case base-case price scenarios deviate from expectations. The most critical metal risk factors for KGHM, one of the largest mining companies globally, include copper, silver, and gold. In the literature, various approaches have been employed to model mineral commodity prices. While our focus in this paper primarily revolves around the stochastic-based approach, alternative methodologies exist, such as time series modeling [1–6] and econometric-based methods [7, 8]. Utilizing the stochastic approach for forecasting market prices stems from the widespread belief that market fluctuations have random origins [9, 10]. Analyzing real data through continuous-time models involves the discrete-time approximation of the theoretical stochastic process, proving more effective for long-term predictions. One of the classical continuous-time stochastic processes applied in describing financial data is the Ornstein–Uhlenbeck model, introduced by Uhlenbeck and Ornstein [11] as a suitable system for velocity in classical Brownian diffusion. Also known as the Vasicek model [12], the Ornstein–Uhlenbeck process was among the earliest stochastic systems used for term structure. It demonstrates the mean-reversion property, indicating that over time, the process tends towards its long-term mean. This behavior is observable in mineral commodity price data.

The classical Ornstein–Uhlenbeck process follows a Gaussian distribution and is represented by the following stochastic differential equation:

$$dX_t = (\psi_1 + \psi_2 X_t)dt + \delta_1 dB_t, \quad (1)$$

where  $\psi_1$ ,  $\psi_2$ , and  $\delta_1$  are constants, and  $\{B_t\}_{t \geq 0}$  represents standard Brownian motion. The process defined in Eq. (1) can be viewed as a modification of the random walk in continuous time. It is also recognized as the continuous version of the discrete-time autoregressive model of order 1 (**AR(1)**) time series [13, 14]. However, some authors [9, 15] argue that financial variables exhibit non-Gaussian distributions, emphasizing that assuming a Gaussian distribution of prices is inappropriate. Consequently, in the literature, many researchers propose modifying the process defined in Eq. (1) by using processes other than Brownian motion as noise [16, 17].

In this paper, we follow this approach and replace the standard Brownian motion with a process of stationary independent increments having a  $\alpha$ -stable distribution [18, 19]. Models based on the  $\alpha$ -stable distribution have been employed to model various phenomena [18, 20].

The second characteristic observed in financial data, in addition to non-Gaussian behavior, is its inhomogeneous nature. Consequently, model (1) with constant coefficients is unsuitable for modeling data with a time-dependent mean and time-dependent scale parameter, especially variance. To address this, various modifications of the classical Ornstein–Uhlenbeck process use time-dependent coefficients instead of constants. Well-known examples include the Ho–Lee [21] and Hull–White [22] models.

In this study, we propose the application of a stochastic model to describe metals' prices, taking into account the aforementioned characteristics of real data. This new model is, in a sense, an extension of the Chan–Karolyi–Longstaff–Sander process based on the  $\alpha$ -stable distribution, as described in [23], which has been utilized for currency exchange rate modeling. The model assumes time-dependent coefficients, capturing the crucial property of the analyzed real prices. These time-varying coefficients represent the time-dependent mean and time-dependent scale parameters of the theoretical process, reflecting the observed behavior in real-time series. Furthermore, the adoption of the general class of  $\alpha$ -stable distributions appears more suitable than

the Gaussian distribution. The  $\alpha$ -stable distribution is more versatile than the Gaussian one, serving as a generalization of the classical distribution. For specific parameter values, it reduces to the normal distribution. Additionally, the  $\alpha$ -stable distribution can describe leptokurtic (like Student's t) or platykurtic (like uniform) distributions, depending on parameter values, enhancing its universality. These considerations suggest that the new stochastic model can effectively capture the specific behavior exhibited by real data.

However, the utilization of the stochastic model with time-dependent parameters and a non-Gaussian distribution necessitates employing more sophisticated parameter estimation techniques. While the literature offers various approaches to estimate the parameters of model (1) [24, 25], only a limited number of research papers propose techniques for estimating the time-dependent parameters of stochastic models [26, 27]. Therefore, one of the main objectives of this paper is to present a step-by-step estimation procedure for the proposed stochastic model. Through Monte Carlo simulations, we demonstrate the efficiency of the developed methodology. The applied section of the paper is dedicated to the analysis of real data. We consider three real datasets representing the daily prices of Gold. These analyzed prices are regarded as the main risk factors in the KGHM mining company, making their long-term prediction a crucial task from a risk management perspective.

The remaining part of the paper is structured as follows:

**Section 2** provides a brief overview of the main characteristics of the  $\alpha$ -stable distribution and introduces the stochastic model with time-dependent parameters, which will be subsequently employed for the description of real data.

In **Section 3**, we outline a step-by-step procedure for estimating the parameters of the introduced model. This procedure involves more advanced techniques compared to the case of fixed coefficients, and the assumption of the  $\alpha$ -stable distribution necessitates non-standard approaches.

Moving on to **Section 4**, we showcase the efficacy of the new estimation procedure using simulated data. **Section 4** is dedicated to the analysis of real data, specifically examining the datasets of gold prices. The obtained results suggest that the proposed stochastic model is versatile and can successfully predict long-term trends in gold prices. The concluding **Section 5** summarizes the paper.

## 2 General stochastic model based on the $\alpha$ -stable distribution

Generally, the discovery of  $\alpha$ -stable laws is attributed to [28], in this article, Lévy explores the central limit theorem and notes that when imposing an infinite variance, the limit law is an  $\alpha$ -stable law. Lévy then sets out to determine the expression of the Fourier transform of all  $\alpha$ -stable probability densities. The probability density of an  $\alpha$ -stable distribution is often characterized as a "heavy-tailed" distribution, indicating that the tail of the distribution decreases asymptotically more slowly than the Gaussian law. It also distinguishes itself by an asymmetry coefficient, reflecting the fact that the probability density is not symmetric about its mode, and it exhibits leptokurtic behavior, indicating that most events are situated near the mean.

The concept of stability arises from the fact that any linear combination of  $\alpha$ -stable random variables also generates an  $\alpha$ -stable law. However, the main obstacle to the use of  $\alpha$ -stable laws lies in the lack of an exact analytical expression for their probability density.

Several application domains (such as finance, including stock market, stock market variation, financial returns, etc.) using  $\alpha$ -stable distributions are listed in the literature, with detailed bibliographies provided by [23, 29–34]. This category of processes plays a major role and exhibits heavy-tailed distributions. It is involved in stochastic modeling in applied sciences, particularly in financial mathematics, and also in the theoretical motivation for the study of their properties [20, 35].

[28] mathematically described the definition of  $\alpha$ -stable laws as an extension of Gaussian laws used in error theory. However, the challenge with the definition of  $\alpha$ -stable laws lies in the absence of an analytical expression, except for special cases such as the Gaussian law, the Cauchy law, or the Lévy law. Therefore,  $\alpha$ -stable laws remained relatively unknown until the work done by [36] in the 1960s, at a time when financial markets were primarily based on the principles of [37], respecting the three principles of the law of large numbers, the central limit theorem, and the independence of present action from its past. However, these mathematical models proved invalid during financial crises. Then, [36] suggested modeling cotton price variations using an  $\alpha$ -stable distribution. Stable laws are now used to represent stock market speculation fluctuations, interest rates, and other aspects of financial markets, providing a robust alternative during crisis periods.

**Definition 1** Let  $X$  be a random variable,  $X$  is called to be a stable law or  $\alpha$ -stable distribution random variable if  $\forall (a, b) \in \mathbb{R}_+^* \times \mathbb{R}_+^*, \exists c > 0$  and  $k \in \mathbb{R}$  such that:

$$aX_1 + bX_2 \stackrel{d}{=} cX + k, \tag{2}$$

where  $X_1$  and  $X_2$  are two random independent variable copies of  $X$ ;

$\stackrel{d}{=}$ : designates convergence in distribution.

If  $k = 0$  then, the distribution is strictly stable.

**Definition 2** A random variable  $X$  is said to have a  $\alpha$ -stable distribution if and only if, for any integer  $n \geq 1$  and for any family  $X_1, X_2, \dots, X_n$  of i.i.d random variables of the same law as  $X$ ,  $\exists (a_n, b_n) \in \mathbb{R}_+^* \times \mathbb{R}$  such that:

$$\frac{(X_1 + X_2 + \dots + X_n) - b_n}{a_n} \stackrel{d}{=} X. \tag{3}$$

Variables with a Levy-stable distribution have the disadvantage of not having (except in three cases) explicit forms for the probability density and the distribution function.

**Definition 3** A random variable  $X$  with a  $\alpha$ -stable law is typically described by its characteristic function  $\Delta_X$  defined on  $\mathbb{R}$  by:

$$\Delta_X(t) = E[\exp(itx)] = \exp(i\mu t - g_{\alpha,\beta,\sigma}(t)), \tag{4}$$

where

$$g_{\alpha,\beta,\sigma}(t) = \begin{cases} \sigma^\alpha |t|^\alpha [1 - i\beta \text{sign}(t) \tan(\frac{\pi\alpha}{2})] & \text{if } \alpha \neq 1 \\ \sigma |t| [1 + \frac{2}{\pi} i\beta \text{sign}(t) \log |t|] & \text{if } \alpha = 1, \end{cases} ; \quad \text{sign}(t) = \frac{t}{|t|} = \begin{cases} 1 & \text{if } t > 0 \\ 0 & \text{if } t = 0 \\ -1 & \text{if } t < 0, \end{cases}$$

and having several representations according to the different parameterizations of the stable laws. The most famous of these representations is given in [23, 33].

The  $\alpha$ -stable law is thus characterized by four real parameters  $\Psi = (\alpha, \beta, \mu, \sigma)$ . The parameter  $\alpha$ , called characteristic exponent or stability index, is an indicator of the degree of thickness of the tails of the distribution: the smaller it is, the thicker the tails are which corresponds to very large fluctuations. It is the most important parameter, it is between 0 and 2 ( $0 < \alpha \leq 2$ ). Its maximum value  $\alpha = 2$ , corresponds to a particular stable law: the Gaussian law or normal law.  $\beta$

is the parameter of dissymmetry, it varies between -1 and 1 ( $-1 \leq \beta \leq 1$ ) and when it is null, the distribution is symmetrical with respect to  $\mu$ . When  $\alpha$  approaches 2,  $\beta$  loses its effect leading to a trend towards the normal distribution. The parameters  $\mu \in \mathbb{R}$  and  $\sigma > 0$  represent the usual characteristics of position and scale respectively with the remark that for the Gaussian distribution, the standard deviation is  $\sigma\sqrt{2}$ . A random variable  $X$  of stable distribution will be noted, according to [33], by:  $X \sim S_\alpha(\beta, \mu, \sigma)$ . The three exceptions mentioned above are the very famous Gaussian law  $S_2(0, \mu, \sigma)$  and the less known Cauchy's law  $S_1(0, \mu, \sigma)$ . and Lévy's law  $S_{\frac{1}{2}}(1, \mu, \sigma)$ . The stable law has an additivity property according to which the sum of two independent stable random variables of the same stability index  $\alpha$  is still stable with the same characteristic exponent  $\alpha$ . This very interesting property is used in finance to study portfolios where two assets with the same value for  $\alpha$  can be considered together. One of the particularities of the stable distribution is that it has infinite variance as soon as  $\alpha$  is strictly less than 2. In fact, the moments of order  $p$  of  $X \sim S_\alpha(\beta, \mu, \sigma)$  are such that for  $\alpha = 2$ ,  $E|X|^p < +\infty, \forall p \in \mathbb{N}$ .

$$E|X|^p = \begin{cases} < \infty & \text{if } 0 < \alpha < p, \\ = \infty & \text{if } p \geq \alpha. \end{cases}$$

More precisely, it is shown that (see for example [33])

$$\lim_{t \rightarrow \infty} t^\alpha \mathbb{P}(X > t) = C_\alpha \frac{1 + \beta}{2} \sigma^\alpha; \quad \lim_{t \rightarrow \infty} t^\alpha \mathbb{P}(X < -t) = C_\alpha \frac{1 - \beta}{2} \sigma^\alpha,$$

where  $C_\alpha$  is a constant given by:

$$C_\alpha = \left( \int_0^\infty x^{-\alpha} \sin x dx \right)^{-1} = \begin{cases} \frac{1-\alpha}{\Gamma(2-\alpha) \cos(\frac{\pi\alpha}{2})} & \text{if } \alpha \neq 1, \\ \frac{2}{\pi} & \text{if } \alpha = 1, \end{cases}$$

with  $\Gamma(\theta)$  is the Euler gamma function defined for  $\theta > 0$ , by:

$$\Gamma(\theta) = \int_0^{+\infty} x^{\theta-1} e^{-x} dx. \tag{5}$$

**Figure 1** illustrates the influence of each parameter of the  $\alpha$ -stable distribution on its probability density function (PDF).

We can thus see that the stable law takes into account the distribution tails which are often carriers of essential information, whereas the Gaussian law neglects these tails thus leading to an error which can be fatal for the investor. The disadvantage of the characteristic function 4 is that it is not continuous if  $\alpha = 1$  which makes it not adapted to numerical calculations and for these reasons [19] proposed another parameterization called  $S_\alpha^0$  which is usable for numerical calculations. simulate stable laws, there is an algorithm developed by [38]. This one allows to generate a law  $S_\alpha(\beta, 0, 1)$ . To obtain a law  $S_\alpha(\beta, \mu, \sigma)$ , with  $\alpha \in ]0, 2]$  and  $\beta \in [-1, 1]$ .

The parameters  $\alpha$  and  $\sigma$  for this generator are very well estimated by the method of [20]. The parameters  $\mu$  and  $\beta$  are correctly estimated by the method of [20] for small values of  $\beta$ , which is often the case for stock exchange chronicles. A bibliography of methods for estimating the parameters of a  $\alpha$ -stable law has been compiled by [39–42]. The PDF of a standard random variable  $\alpha$ -stable law in the  $S^0$  representation [43] i.e.  $X \sim S_\alpha^0(1, \beta, 0)$ .

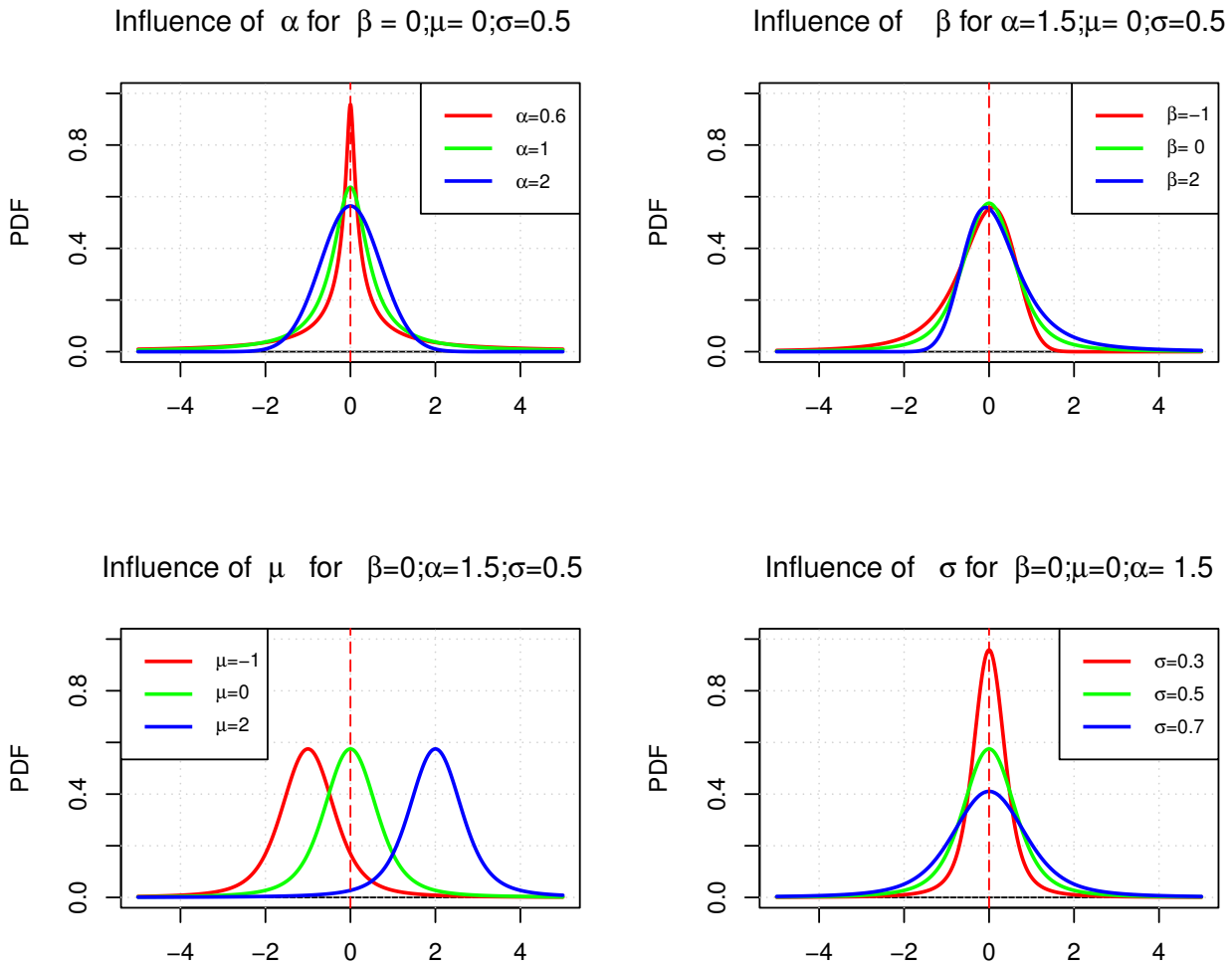


**Figure 1.** Influences of the parameters of the  $\alpha$ -stable distribution on its PDF.

Let’s commence the analysis of the stochastic process described by the following stochastic differential equation [44]:

$$dX_t = \psi(X_t, t)dt + \delta(X_t, t)dB_t. \tag{6}$$

In general,  $\psi(\cdot)$  and  $\delta(\cdot)$  are functions defined as  $\psi(\cdot), \delta(\cdot) : \mathbb{R} \times [0, T] \longrightarrow \mathbb{R}$ , and  $\{B_t\}_{t \geq 0}$  represents standard Brownian motion.

Consequently,  $dB_t = B_{t+dt} - B_t$  follows a Gaussian distribution, denoted as  $dB_t \sim \mathcal{N}(0, dt)$  [45]. The conditional distribution of the increments of the process defined in Eq. (6) is outlined in **Lemma 2**.

Several well-known examples that conform to Model (6), where the functions  $\psi(\cdot)$  and  $\delta(\cdot)$  are constant, include Merton [46], Vasicek [12], Brennan–Schwartz ([47]), Dothan [48], and Cox–Ingersoll–Ross [49] processes. Notable models with non-constant functions  $\psi(\cdot)$  and  $\delta(\cdot)$  comprise Ho–Lee [21], Hull–White [22], and Black–Kraśiński [50], as detailed in Table 1.

However, in numerous real-world applications, the Gaussian distribution in model (6) may prove inadequate. Therefore, we propose modifying the model and assuming that the considered process satisfies the subsequent stochastic differential equation:

$$dX_t = \psi(X_t, t)dt + \delta(X_t, t)dS_t. \tag{7}$$

Similar to the previous scenario, in the general case,  $\psi(\cdot)$  and  $\delta(\cdot): \mathbb{R} \times [0, T] \rightarrow \mathbb{R}$  are appropriate functions. In this context, we assume that  $\{S_t\}$  is a process with stationary independent increments, following the  $\alpha$ -stable distribution. In this case, the increment process  $\{dS_t\} = \{S_{t+dt} - S_t\}$  constitutes a sequence of independent identically distributed (iid) random variables of the  $\alpha$ -stable distribution, with the assumption  $\mathbb{E}(dS_t) = 0$  and  $\mathbb{E}(dS_t^2) = dt$ .

In the subsequent calculations, we assume specific forms for the functions  $\psi(\cdot)$  and  $\delta(\cdot)$ , and ultimately, the analyzed process is described by the stochastic differential equation:

$$dX_t = (\psi_1(t) + \psi_2(t)X_t)dt + (\delta_1(t) + \delta_2(t)X_t)dS_t, \tag{8}$$

for the general functions  $\psi_1(\cdot), \psi_2(\cdot), \delta_1(\cdot)$  and  $\delta_2(\cdot): [0, T] \rightarrow \mathbb{R}$ . Additionally, we restrict our consideration to the case where  $0 < \alpha < 2$ . Further constraints on the functions are provided in the subsequent section.

**Table 1.** Classical models described by Eq. (6)

Model	$\psi(X_t, t)$	$\delta(X_t, t)$
Merton	$\psi_1$	$\delta_1$
Vasicek	$\psi_1 + \psi_2 X_t$	$\delta_1$
Dothan	$\psi_1 X_t$	$\delta_1 X_t$
Brennan–Schwartz	$\psi_1 + \psi_2 X_t$	$\delta_1 X_t$
Cox–Ingersoll–Ross	$\psi_1 + \psi_2 X_t$	$\delta_1 \sqrt{X_t}$
Ho–Lee	$\psi_1(t)$	$\delta_1(t)$
Hull–White	$\psi_1(t) + \psi_2(t)X_t$	$\delta_1(t)$
Black–Derman–Toy	$\psi_1(t) + \psi_2(t) \ln X_t$	$\delta_1(t)$
Black–Kraśniński	$\psi_1(t) + \psi_2(t)X_t \ln X_t$	$\delta_1(t)$

**Proposition 1** Let  $X_1, X_2$  be two random variables  $\alpha$ -stable with  $X_1 \sim S_\alpha(\beta, \mu, \sigma)$  and  $X_2 = \frac{X_1 - \mu}{\sigma^{\frac{1}{\alpha}}}$ . For  $\alpha \neq 1$  then, we have the following equivalences:

- i.  $X_1 \sim S_\alpha(\beta, \mu, \sigma)$ ;
- ii.  $X_2 = \frac{X_1 - \mu}{\sigma^{\frac{1}{\alpha}}} \sim S_\alpha(\beta, 0, 1)$ .

For  $\alpha = 1$  then, we have the following equivalences:

- i.  $X_1 \sim S_1(\beta, \mu, \sigma)$ ;
- ii.  $X_2 = \frac{X_1 - \mu}{\sigma} \sim S_1(\beta, \frac{2}{\pi}\beta \log(\sigma), 1)$ .

**Proof** For  $\alpha \neq 1$  then, we have (1) $\implies$  (2):

$$\begin{aligned} \Delta_{X_2}(r) &= E \left[ \exp \left( ir \left( \frac{X_1 - \mu}{\sigma^{\frac{1}{\alpha}}} \right) \right) \right] = E \left[ \exp \left( \frac{irX_1}{\sigma^{\frac{1}{\alpha}}} \right) \exp \left( \frac{-ir\mu}{\sigma^{\frac{1}{\alpha}}} \right) \right] \\ &= \exp \left( \frac{-ir\mu}{\sigma^{\frac{1}{\alpha}}} \right) E \left[ \exp \left( \frac{irX_1}{\sigma^{\frac{1}{\alpha}}} \right) \right] = \exp \left( \frac{-ir\mu}{\sigma^{\frac{1}{\alpha}}} \right) \Delta_{X_1} \left( \frac{r}{\sigma^{\frac{1}{\alpha}}} \right) \\ &= \exp \left( \frac{-ir\mu}{\sigma^{\frac{1}{\alpha}}} \right) \exp \left( \frac{ir\mu}{\sigma^{\frac{1}{\alpha}}} - \sigma \left| \frac{r}{\sigma^{\frac{1}{\alpha}}} \right|^\alpha \left[ 1 - i\beta \operatorname{sign} \left( \frac{r}{\sigma^{\frac{1}{\alpha}}} \right) \tan \left( \frac{\pi\alpha}{2} \right) \right] \right). \end{aligned}$$

Such as  $\sigma > 0$  so:  $\operatorname{sign} \left( \frac{r}{\sigma^{\frac{1}{\alpha}}} \right) = \operatorname{sign}(r) \cdot \operatorname{sign} \left( \frac{1}{\sigma^{\frac{1}{\alpha}}} \right) = \operatorname{sign}(r)$ .

Subsequently:

$$\begin{aligned} \Delta_{X_2}(r) &= \exp \left( \frac{-ir\mu}{\sigma^{\frac{1}{\alpha}}} \right) \exp \left( \frac{ir\mu}{\sigma^{\frac{1}{\alpha}}} - \sigma \left| \frac{r}{\sigma^{\frac{1}{\alpha}}} \right|^\alpha \left[ 1 - i\beta \operatorname{sign}(r) \tan \left( \frac{\pi\alpha}{2} \right) \right] \right) \\ &= \exp \left( -|r|^\alpha \left[ 1 - i\beta \operatorname{sign}(r) \tan \left( \frac{\pi\alpha}{2} \right) \right] \right). \end{aligned}$$

So  $Y \sim S_\alpha(\beta, 0, 1)$ .

(2) $\implies$  (1) is proven in the same way as (1) $\implies$  (2).

For  $\alpha = 1$  then, (1) $\implies$  (2) we have:

$$\begin{aligned} \Delta_{X_2}(r) &= E \left[ \exp \left( ir \left( \frac{X_1 - \mu}{\sigma} \right) \right) \right] = E \left[ \exp \left( \frac{irX_1}{\sigma} \right) \exp \left( \frac{-ir\mu}{\sigma} \right) \right] \\ &= \exp \left( \frac{-ir\mu}{\sigma} \right) E \left[ \exp \left( \frac{irX_1}{\sigma} \right) \right] \\ &= \exp \left( \frac{-ir\mu}{\sigma} \right) \exp \left( \frac{ir\mu}{\sigma} - \sigma \left| \frac{r}{\sigma} \right| \left( 1 + i\frac{2}{\pi} \beta \operatorname{sign} \left( \frac{r}{\sigma} \right) \log \left| \frac{r}{\sigma} \right| \right) \right) \\ &= \exp \left( -|r| \left[ 1 + i\frac{2}{\pi} \beta \operatorname{sign}(r) \log \left( \left| \frac{r}{\sigma} \right| \right) \right] \right) \\ &= \exp \left( i\frac{2}{\pi} \beta |r| \operatorname{sign}(r) \log(\sigma) - |r| \left[ 1 + i\frac{2}{\pi} \beta \operatorname{sign}(r) \log(|r|) \right] \right) \\ &= \exp \left( i\frac{2}{\pi} \beta \log(\sigma)r - |r| \left[ 1 + i\frac{2}{\pi} \beta \operatorname{sign}(r) \log(|r|) \right] \right). \end{aligned}$$

So  $X_2 = \frac{X_1 - \mu}{\sigma^{\frac{1}{\alpha}}} \sim S_\alpha(\beta, \frac{2}{\pi} \beta \log(\sigma), 1)$ .

(2) $\implies$  (1) is demonstrated in the same way as (1) $\implies$  (2). This completes the proof of this **Proposition 1**.

**Lemma 1** Let  $X_1$  and  $X_2$  two random variables  $\alpha$ -stable.

For  $\alpha \neq 1$ , if  $X_1 \sim S_\alpha(\beta, 0, 1)$  and  $X_2 \sim S_\alpha(\beta, \mu, \sigma)$ . Then,

$$\sigma X_1 + \mu \stackrel{d}{=} X_2.$$

**Proof** Let us define  $X_1 \sim S_\alpha(\beta, 0, 1)$  and  $X_2 \sim S_\alpha(\beta, \mu, \sigma)$ . We will show that:

$$\mathcal{P}(\sigma X_1 + \mu < r) = \mathcal{P}(X_2 < r). \tag{9}$$

If  $f$  is the probability density function of the  $\alpha$ -stable random variable  $X_1$  then, we have:

$$f(r, \alpha, \beta, \mu, \sigma) = \frac{1}{\sigma} f\left(\frac{r - \mu}{\sigma}, \alpha, \beta, 0, 1\right). \tag{10}$$

We use the formula from Eq. (10) for the PDF of  $\alpha$ -stable distribution given in Eq. (9):

$$\begin{aligned} \mathcal{P}(\sigma X_1 + \mu < r) &= \mathcal{P}\left(X_1 < \frac{r - \mu}{\sigma}\right) \\ &= \int_{-\infty}^{\frac{r - \mu}{\sigma}} f(t, \alpha, \beta, 0, 1) dt \\ &= \int_{-\infty}^r \frac{1}{\sigma} f\left(\frac{t - \mu}{\sigma}, \alpha, \beta, 0, 1\right) dt \\ &= \int_{-\infty}^r f(t, \alpha, \beta, \mu, \sigma) dt \\ &= \mathcal{P}(X_2 < r). \end{aligned}$$

**Lemma 2** For the stochastic process  $\{X_t\}$  as defined in Eq. (6), the increment  $dX_t = X_{t+dt} - X_t$  follows the subsequent relationship:

$$dX_t | X_t \sim \mathcal{N}\left(\psi(X_t, X_t)dt, \delta^2(X_t, t)dt\right).$$

**Proof** Initially, we will demonstrate that:

$$\mathbb{E}(dX_t | X_t) = \psi(X_t, t)dt; \quad \text{and } \text{Var}(dX_t | X_t) = \delta^2(X_t, X_t)dt.$$

To establish this, we will leverage the properties of standard Brownian motion, where  $\mathbb{E}(dB_t) = 0$  and  $\mathbb{E}(dB_t^2) = dt$ . Consequently, we derive:

$$\begin{aligned} \mathbb{E}(dX_t | X_t) &= \mathbb{E}(\psi(X_t, t)dt + \delta(X_t, t)dB_t | X_t) \\ &= \mathbb{E}(\psi(X_t, t)dt | X_t) + \mathbb{E}(\delta(X_t, t)dB_t | X_t) \\ &= \psi(X_t, t)dt + \delta(X_t, t)\mathbb{E}(dB_t) \\ &= \psi(X_t, t)dt. \end{aligned}$$

The second moment of  $dX_t | X_t$  is expressed as:

$$\begin{aligned} \mathbb{E}(dX_t^2 | X_t) &= \mathbb{E}((\psi(X_t, t)dt + \delta(X_t, t)dB_t)^2 | X_t) \\ &= \mathbb{E}(\psi^2(X_t, t)dt^2 | X_t) + 2\mathbb{E}(\psi(X_t, t)dt\delta(X_t, t)dB_t | X_t) + \mathbb{E}(\delta^2(X_t, t)dB_t^2 | X_t) \\ &= \psi^2(X_t, t)dt^2 + 2\psi(X_t, t)dt\delta(X_t, t)\mathbb{E}(dB_t | X_t) + \delta^2(X_t, t)\mathbb{E}(dB_t^2 | X_t) \\ &= \psi^2(X_t, t)dt^2 + \delta^2(X_t, t)dt. \end{aligned}$$

Thus, the variance of  $dX_t | X_t$  can be expressed as:

$$\begin{aligned} \text{Var}(dX_t | X_t) &= \mathbb{E}(dX_t^2 | X_t) - [\mathbb{E}(dX_t | X_t)]^2 \\ &= \psi^2(X_t, t)dt^2 + \delta^2(X_t, t)dt - [\psi(X_t, t)dt]^2 \\ &= \delta^2(X_t, t)dt. \end{aligned}$$

Due to the Gaussian distribution of  $dB_t$  and the property  $\mathbb{E}(X + c) = \mathbb{E}(X) + c$  for any random variable  $X$ , as well as  $\text{Var}(cX) = c^2\text{Var}(X)$ , we can express  $dX_t | X_t$  as:

$$dX_t | X_t \sim \mathcal{N} \left( \psi(X_t, t)dt, \delta^2(X_t, t)dt \right).$$

### 3 Estimation of the parameters for general model based on $\alpha$ -stable distribution

In this section, we outline a method for estimating the parameters of the stochastic process described in Eq. (8).

Let's assume we have a vector of realizations of the stochastic process given by Eq. (8), denoted as  $X_0, X_2, \dots, X_n$ , with corresponding time points  $t_0, t_1, \dots, t_n$ , such that  $\forall_{j \in \{1, 2, \dots, n\}}$

$$t_j - t_{j-1} = \Theta.$$

For the sake of simplicity, we assume  $\Theta = 1$ .

Consequently, we represent the increments of the observed data as  $y_0, y_1, \dots, y_{n-1}$ , where  $y_j = X_{j+1} - X_j$  for  $j = 0, 1, \dots, n - 1$ . To achieve this, we initially transform Eq. (8) into its discrete form.

$$\begin{aligned} y_j &= X_{j+1} - X_j \\ &= \psi_1(t_j) + \psi_2(t_j)X_j + (\delta_1(t_j) + \delta_2(t_j)X_j)S_j; \quad j = 0, 1, \dots, n - 1. \end{aligned} \tag{11}$$

In this context,  $\{s_j\}$  represents a time series of independent and identically distributed (iid) random variables following the  $\alpha$ -stable distribution  $S_\alpha(\beta, \mu = 0, \sigma = 1)$ .

In this paper, we employ the local regression approach [51], following a similar methodology as in [27], to derive estimates for the functions  $\psi_1(\cdot)$  and  $\psi_2(\cdot)$  within Model (8). We make the assumption that  $\psi_1(\cdot) \in C^{d_1^\psi}$  and  $\psi_2(\cdot) \in C^{d_2^\psi}$ , allowing them to be expanded into Taylor's polynomials [52] at every time point  $t^* \in \{t_0, t_1, \dots, t_{n-1}\}$  of degrees  $d_1^\psi$  and  $d_2^\psi$ , respectively:

$$\psi_l(t_j) = \sum_{k=0}^{d_l^\psi} \frac{\psi_l^{(k)}(t^*)}{k!} (t_j - t^*)^k + R_{d_l^\psi}(t_j); \quad l = 1, 2, \tag{12}$$

where  $R_{d_l^\psi}(\cdot)$  represents Peano's remainder, which we, in further considerations, neglect. After expanding (12) and consolidating constants for common  $t_j^k$ , we arrive at the following approximation:

$$\psi_l(t_j) \approx \sum_{k=0}^{d_l^\psi} k \psi_l t_j^k; \quad l = 1, 2. \tag{13}$$

To obtain  ${}_k\psi_l$  estimates for all  $t_j$  in the vicinity of  $\rho$  from Eq. (13), we formulate the loss function as a weighted sum of squared errors. It's important to emphasize that  $\{{}_k\psi_l\}$  is estimated independently for each time point  $t^* \in \{t_0, t_1, \dots, t_{n-1}\}$ . Deriving from Eq. (11), we derive the following:

$$\begin{aligned}
 S_j &= \frac{y_j - (\psi_1(t_j) + \psi_2(t_j)X_j)}{\delta_1(t_j) + \delta_2(t_j)X_j} \\
 &\approx \frac{y_j - \left(\sum_{k=0}^{d_1^\psi} {}_k\psi_1 t_j^k + \sum_{k=0}^{d_2^\psi} {}_k\psi_2 t_j^k X_j\right)}{\delta_1(t_j) + \delta_2(t_j)X_j} \\
 &=: \tilde{S}_j; \quad j = 0, 1, \dots, n-1.
 \end{aligned}
 \tag{14}$$

In this paper, we posit that the loss function, utilized in the estimation algorithm for each  $t^* \in \{t_0, t_1, \dots, t_{n-1}\}$ , adopts the following form:

$$G_{\tilde{\Omega}}^* (\{X_j\}, \{t_j\}; \{{}_k\psi_l\}) = \sum_{j=0}^{n-1} \tilde{S}_j^2 K_{\rho^\psi, \rho_r^\psi} (t_j - t^*) + \eta \left( \sum_{k=0}^{d_1^\psi} {}_k\psi_1^2 + \sum_{k=0}^{d_2^\psi} {}_k\psi_2^2 \right), \tag{15}$$

with  $\tilde{\Omega} = (t^*, \delta, \eta, d_1^\psi, d_2^\psi, \rho^\psi, \rho_r^\psi)$ .

The first component of the loss function, specifically  $\tilde{S}_j^2 K_{\rho^\psi, \rho_r^\psi} (t_j - t^*)$ , is linked to the fact that the estimators are fitted locally (rather than globally). Additionally, akin to Ridge regression [53], we have incorporated into the loss function a second component.

Tikhonov regularization [54] (with parameter  $\eta$ ). This regularization compensates for the potentially non-unique solution and high variance of the estimators. In this paper, we utilized a single-valued parameter  $\eta$ ; however, it can be replaced with a vector  $\{\eta_j\}$ . This substitution results in improved estimates but requires the entire vector  $\{\eta_j\}$  to be determined. In this paper, we suggest using the asymmetric kernel function  $K_{\rho, \rho_r}(\cdot)$  in Eq. (15), defined as follows:

$$K_{\rho, \rho_r} (t) = \frac{2K\left(\frac{t}{\rho - \rho_r}\right) \mathbb{1}_{t \leq 0} + K\left(\frac{t}{\rho_r}\right) \mathbb{1}_{t > 0}}{\rho}. \tag{16}$$

In this context, " $\rho$ " represents the width of the kernel function  $K_{\rho, \rho_r}(\cdot)$ , denoting the distance from the left root to the right, while " $\rho_r$ " represents the distance to the right root from 0. This specific form of the kernel provides the flexibility to strike a balance between the traditional symmetric and causal kernel functions, resulting in estimators with reduced variance. The parameters  $\rho^\psi, \rho_r^\psi, d_1^\psi, d_2^\psi$  and  $\eta$  in the estimation process are referred to as hyperparameters. In practical applications, three commonly utilized kernel functions  $K(\cdot)$  in Eq. (16) are [27, 51, 55, 56]:

- Gaussian kernel:  $K(t) = \frac{1}{\sqrt{2\pi}} \exp(-\frac{t^2}{2})$ ;
- Epanechnikov kernel:  $K(t) = \frac{3}{4}(1 - t^2) \mathbb{1}_{t \in (-1,1)}$ ;
- Tricube kernel:  $K(t) = \frac{70}{81}(1 - |t|^3)^3 \mathbb{1}_{t \in (-1,1)}$ .

Because of their compact support, the Epanechnikov and tricube kernels are commonly employed in modeling financial data problems [27, 51, 56]. In our applications, we opted for the tricube kernel.

To streamline the calculations, the initial step of the estimation procedure involves treating the  $\delta_1(\cdot)$  and  $\delta_2(\cdot)$  functions in model (8) as known. We utilize an iterative method to derive estimates,

commencing with a predefined starting condition:

$$\zeta_{j,\eta}^{(0)} := \hat{\delta}_1(t_j) + \hat{\delta}_2(t_j)X_j \equiv 1. \tag{17}$$

Nevertheless, the optimal values for  $d_1^\psi, d_2^\psi$  (refer to Eq. (13)), as well as the kernel widths  $\rho^\psi, \rho_r^\psi$ , remain unknown. We determine the optimal values for hyperparameters  $\rho^\psi, \rho_r^\psi, d_1^\psi, d_2^\psi$  and  $\eta$  (refer to Eq. (15)) by selecting those that result in the lowest mean squared error (MSE) statistics:

$$MSE_Y = \sum_{j=0}^{n-1} \left( y_j - \left( \sum_{k=0}^{d_1^\psi} k \hat{\psi}_1 t_j^k + \sum_{k=0}^{d_2^\psi} k \hat{\psi}_2 t_j^k X_j \right) \right)^2 \omega_j, \tag{18}$$

$$MSE_X = \sum_{j=1}^n \left( X_j - X_0 - \sum_{h=1}^j \left( \sum_{k=0}^{d_1^\psi} k \hat{\psi}_1 t_h^k + \sum_{k=0}^{d_2^\psi} k \hat{\psi}_2 t_h^k X_h \right) \right)^2 \omega_j, \tag{19}$$

and the Augmented Dickey–Fuller test statistic [57] (where the null hypothesis assumes the presence of a unit root in the time series data) for the vector

$$\left\{ y_j - \left( \sum_{k=0}^{d_1^\psi} k \hat{\psi}_1 t_j^k + \sum_{k=0}^{d_2^\psi} k \hat{\psi}_2 t_j^k X_j \right) \right\}.$$

The weights  $\{\omega_j\}$  in Eqs. (18) and (19) are computed using the exponential smoothing method [58]. Once the optimal values for hyperparameters are determined, we can express the loss function  $G^*(\cdot)$  defined in Eq. (15) using matrices:

$$Y = \begin{pmatrix} y_0 \\ y_1 \\ \vdots \\ y_{n-1} \end{pmatrix}; \quad \Psi = \begin{pmatrix} 0\psi_1 \\ 1\psi_1 \\ 2\psi_1 \\ \vdots \\ d_1^\psi\psi_1 \\ 0\psi_2 \\ 1\psi_2 \\ \vdots \\ d_2^\psi\psi_2 \end{pmatrix}; \quad T = \begin{pmatrix} 1 & 1 & \cdots & 1 \\ t_0 & t_1 & \cdots & t_{n-1} \\ t_0^2 & t_1^2 & \cdots & t_{n-1}^2 \\ \vdots & \vdots & \ddots & \vdots \\ t_0^{d_1^\psi} & t_1^{d_1^\psi} & \cdots & t_{n-1}^{d_1^\psi} \\ X_0 & X_1 & \cdots & X_{n-1} \\ t_0 X_0 & t_1 X_1 & \cdots & t_{n-1} X_{n-1} \\ \vdots & \vdots & \ddots & \vdots \\ t_0^{d_2^\psi} X_0 & t_1^{d_2^\psi} X_1 & \cdots & t_{n-1}^{d_2^\psi} X_{n-1} \end{pmatrix};$$

$$K_{t^*} = \begin{pmatrix} \frac{K_{\rho^{\psi}, \rho_r^{\psi}} \psi(t_0 - t^*)}{(\zeta_{0,\eta}^{(0)})^2} & 0 & 0 & \dots & 0 \\ 0 & \frac{K_{\rho^{\psi}, \rho_r^{\psi}} \psi(t_1 - t^*)}{(\zeta_{1,\eta}^{(0)})^2} & 0 & \dots & 0 \\ \vdots & \vdots & \vdots & \ddots & \vdots \\ 0 & 0 & \dots & 0 & \frac{K_{\rho^{\psi}, \rho_r^{\psi}} \psi(t_{n-1} - t^*)}{(\zeta_{n-1,\eta}^{(0)})^2} \end{pmatrix}.$$

Then, the loss function from Eq. (15) takes the form:

$$G^* = (Y - T'\Psi)'K_{t^*}(Y - T'\Psi) + \eta\Psi'\Psi; \tag{20}$$

which we minimize Eq. (20) with respect to the vector  $\Psi$ :

$$\frac{\partial G^*}{\partial \Psi} = -2TK_{t^*}(Y - T'\Psi) + 2\eta I\Psi = 0. \tag{21}$$

Then,

$$(TK_{t^*}T' + \eta I)\Psi = TK_{t^*}Y \implies \hat{\Psi} = (TK_{t^*}T' + \eta I)^{-1}TK_{t^*}Y. \tag{22}$$

With the estimation of  $\psi_1(\cdot)$  and  $\psi_2(\cdot)$  functions from model (8), we can proceed to estimate the functions  $\delta_1(\cdot)$  and  $\delta_2(\cdot)$ . In a manner similar to the estimation of  $\psi_1(\cdot)$  and  $\psi_2(\cdot)$  functions, we will employ Taylor's polynomials [52] to approximate the functions  $\delta_1(\cdot)$  and  $\delta_2(\cdot)$  from model (8):

$$\delta_l(t_j) \approx \sum_{k=0}^{d_l^\delta} k\delta_l t_j^k, l = 1, 2. \tag{23}$$

Subsequently, the parameters  $\{\delta_l\}$  can be determined through the maximum likelihood method [51]. Leveraging properties established in Lemma 1 and considering the independence and identically distributed (iid) nature of  $\{S_j\}$ , the log-likelihood function can be expressed as:

$$l_{\tilde{\Omega}_\delta}^*(\tilde{\Omega}_{par}) = \sum_{j=0}^{n-1} \ln \left( f \left( \hat{e}_j; \sum_{k=0}^{d_1^\delta} k\delta_1 t_j^k + \sum_{k=0}^{d_2^\delta} k\delta_2 t_j^k, \alpha, \beta, 0, \sigma \right) \right) K_{\rho^\delta, \rho_r^\delta}(t_j - t^*); \tag{24}$$

with:  $\tilde{\Omega}_\delta = (t^*, \delta, \eta, d_1^\delta, d_2^\delta, \rho^\delta, \rho_r^\delta)$ ;  $\tilde{\Omega}_{par} = (\{\hat{e}_j\}, \{t_j\}; \{\delta_l\}, \alpha, \beta, \sigma)$ .

where  $\hat{e}_j$  is derived by transforming Eq. (11) in the following manner:

$$\hat{e}_j := y_j - (\hat{\psi}_1(t_j) + \hat{\psi}_2(t_j)X_j) \approx (\delta_1(t_j) + \delta_2(t_j)X_j)S_j; j = 0, 1, 2, \dots, n - 1. \tag{25}$$

In this scenario, additional optimal hyperparameters, namely  $d_j^\delta$  ( $j = 1, 2$ ),  $\rho^\delta$  and  $\rho_r^\delta$ , must be determined. We suggest employing the Breusch-Pagan test statistic [59] with the null hypothesis

that the variance is independent of descriptive (independent) variables, indicating homoscedasticity in the time series. We aim to identify the set of hyperparameters  $d_j^\delta$  ( $j = 1, 2$ ),  $\rho^\delta$  and  $\rho_r^\delta$  that minimizes the test statistic calculated for the time series:

$$\{\hat{S}_j\} = \frac{y_j - \left( \sum_{k=0}^{d_1^\psi} k \hat{\psi}_1 t_j^k + \sum_{k=0}^{d_2^\psi} k \hat{\psi}_2 t_j^k X_j \right)}{\hat{\delta}_1(t_j) + \hat{\delta}_2(t_j) X_j}. \quad (26)$$

Once hyperparameters are determined, we optimize the log-likelihood function (Eq. 24) with respect to  $\{k\delta_j\}$  (as defined in Eq. 23) and the unknown parameters  $\alpha, \beta, \sigma$  associated with residuals. Since there is no analytical solution for maximizing the function (Eq. 24), numerical algorithms are required to find the function's maximum. To streamline the computations, we exploit the invariance property of maximum likelihood estimators [23, 30, 60, 61].

Note that  $\alpha \in ]0, 2]$ ,  $\beta \in [-1, 1]$ , and  $\sigma > 0$ . We aim to maximize the function  $l^*(.)$  (Eq. 24) with respect to the parameters:  $k\delta_j \in \mathbb{R}$  ( $j = 1, 2$ ; and  $k = 0, \dots, d_j^\delta$ );  $\hat{\alpha} \in ]0, 2]$ ,  $\hat{\beta} \in [-1, 1]$ , and  $\hat{\sigma} \in \mathbb{R}_+^*$ . Optimization can be achieved using a broader and more straightforward class of algorithms, such as the Broyden–Fletcher–Goldfarb–Shanno algorithm [62].

The initial proposition of  $\zeta_{j,\delta}^{(0)} \equiv 1$  (refer to Eq. (17)) can be highly questionable, particularly in cases of evident heteroskedasticity in time series.

To address this concern, we employ an iterative method for estimating  $\psi_1(.), \psi_2(.), \delta_1$  and  $\delta_2(.)$ . In the subsequent step of the estimation, we set:

$$\{\zeta_{j,\psi}^{(1)}\} = \{\hat{\psi}_1(t_j) + \hat{\psi}_2(t_j) X_j\}; \quad \text{and} \quad \{\zeta_{j,\delta}^{(1)}\} = \{\hat{\delta}_1(t_j) + \hat{\delta}_2(t_j) X_j\};$$

and repeat the entire estimation procedure until the changes in the estimated functions become negligible, that is, until:

$$\exists_j \left\| \zeta_{j,\psi}^{(\gamma)} - \zeta_{j,\psi}^{(\gamma-1)} \right\| > \epsilon_\psi \quad \text{or} \quad \exists_j \left\| \zeta_{j,\delta}^{(\gamma)} - \zeta_{j,\delta}^{(\gamma-1)} \right\| > \epsilon_\delta,$$

where  $\epsilon_\psi$  and  $\epsilon_\delta$  are defined thresholds, and  $\gamma$  represents the current iteration number (or after a specified number of iterations).

After estimating the  $\psi_1(.), \psi_2(.), \delta_1$  and  $\delta_2(.)$  functions, we can ultimately estimate the global parameters of residuals  $\{\hat{S}_j\}$  (defined in Eq. (26)) modeled by the  $\alpha$ -stable distribution. In the previous steps of the estimation procedure, only local estimates of the parameters are obtained. We find  $\hat{\alpha}, \hat{\beta}$ , and  $\hat{\sigma}$  by numerically maximizing the likelihood function with respect to  $\hat{\alpha}, \hat{\beta}$ , and  $\hat{\sigma}$  refer to [30, 60]:

$$L(\{\hat{S}_j\}, \hat{\alpha}, \hat{\beta}, \hat{\sigma}) = \prod_{j=0}^{n-1} \frac{1}{\sigma} f(\hat{S}_j, \alpha, \beta, 0, 1). \quad (27)$$

An algorithm describing the parameter estimation procedure is shown in [Figure 2](#).

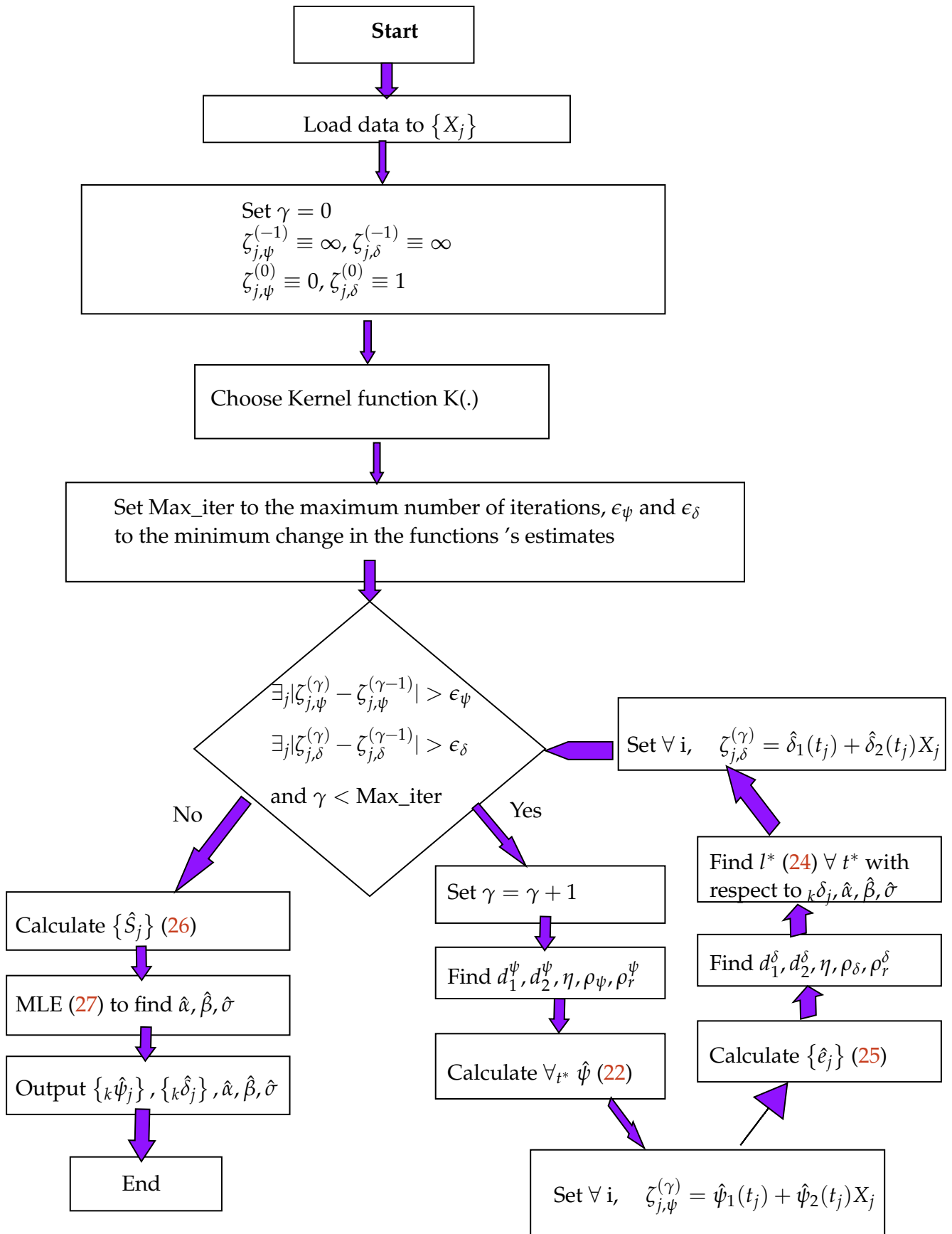


Figure 2. Algorithm describing the parameter estimation procedure

## 4 Numerical simulation

### Simulated data analysis

Utilizing the methodology outlined in Section 3, we evaluate the efficacy of the estimation procedure through the analysis of simulated data. Employing Euler’s method, Runge Kutta’s method and Milstein’s method [63], we simulate the trajectory of the process governed by the stochastic differential equation:

$$dX_t = (0.1 + 0.025t - 0.015X_t)dt + (0.03 + 0.001t)dS_t, \quad (28)$$

under the assumption:  $dS_t \sim S_\alpha(\beta, \mu, \sigma)$  with  $\alpha = 1.8, \beta = 0.8, \mu = 0$  and  $\sigma = 1$ .

The illustration of the  $\{dS_t\}$  and  $\{X_t\}$  processes is depicted in Figure 3 as an exemplary representation. Model parameters are intentionally selected in a manner that allows them to be, in some sense, comparable to the parameters derived from real data.

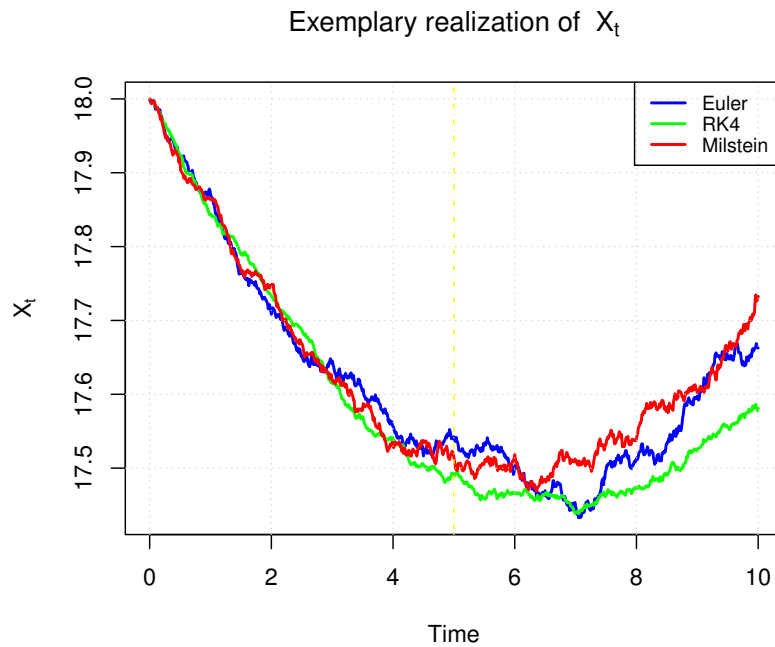


**Figure 3.** The illustrative realizations of the stochastic process defined by Eq. (28) with residuals following the  $\alpha$ -stable distribution

Applying the outlined methodology, we have computed the  $\psi_1(\cdot)$ ,  $\psi_2(\cdot)$ ,  $\delta_1(\cdot)$ , and  $\delta_2(\cdot)$  functions based on model (8). In Figure 4 and Figure 5, we display both the estimated functions and the theoretical counterparts from Model (28). It is evident from the observation that the estimates align well with the theoretical functions. The estimated parameters for the  $\alpha$ -stable distribution (using the method for estimating [20]) are  $\hat{\alpha} = 1.84385$ ,  $\hat{\beta} = 0.7672$ ,  $\hat{\mu} = 0$ , and  $\hat{\sigma} = 0.9873$  demonstrating close proximity to the theoretical parameters  $\alpha = 1.8, \beta = 0.8, \mu = 0$  and  $\sigma = 1$ . Additionally, the Kolmogorov–Smirnov test [64] resulted in a statistic  $K = 0.00586$  and a p-value of 0.930, leading to the conclusion that the model parameters have been accurately estimated.

Moreover, we have conducted Monte-Carlo simulations [65] for the process defined by Eq. (28). Specifically, we have generated 100 realizations of the process and applied the estimation methodology outlined in the preceding section. Subsequently, we have obtained estimates

for  $[0.05, 0.25, 0.5, 0.75, 0.95]$  quantiles of the  $\psi_1(\cdot)$ ,  $\psi_2(\cdot)$ ,  $\delta_1(\cdot)$ , and  $\delta_2(\cdot)$  functions' estimators.

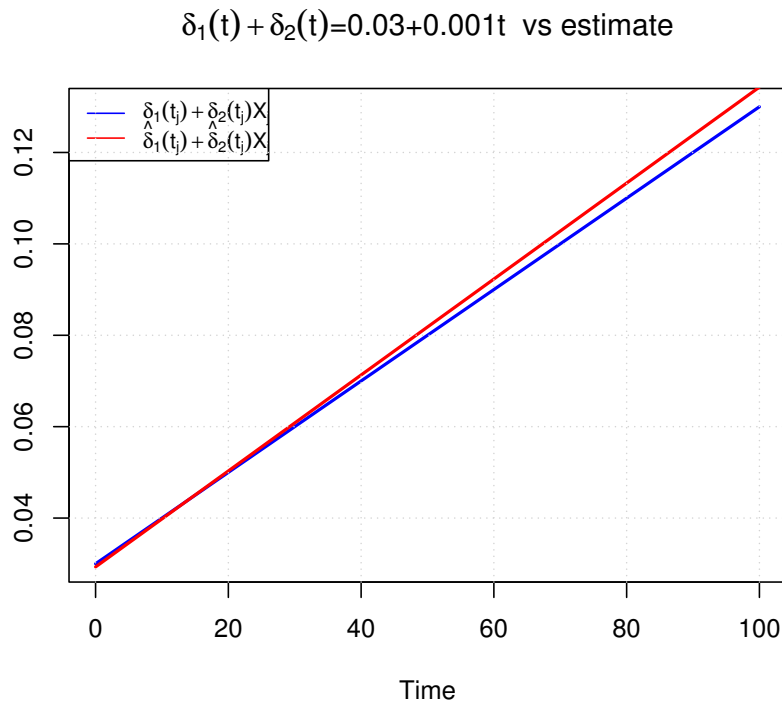


**Figure 4.** Comparison of the theoretical functions  $\delta_1(t) + \delta_2(t) = 0.03 + 0.001t$  with its estimate

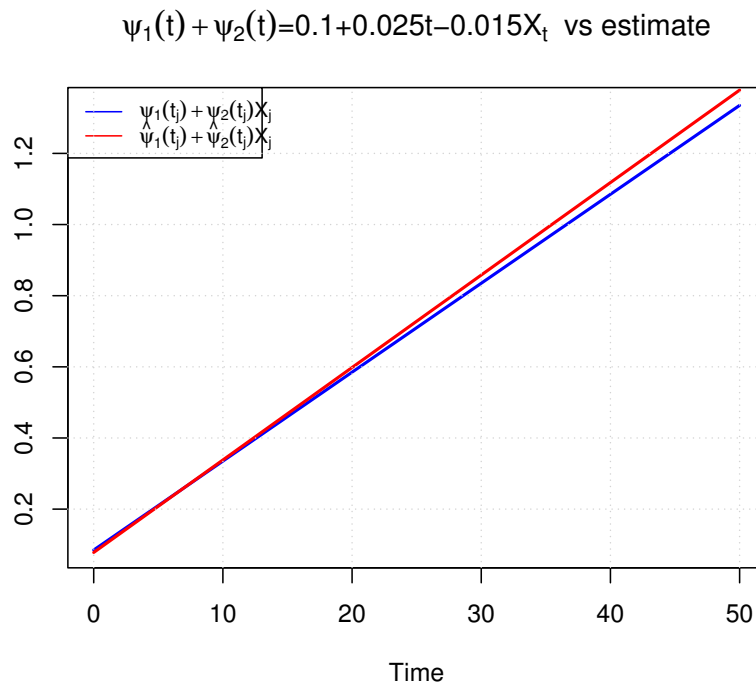


**Figure 5.** Comparison of the theoretical functions  $\psi_1(t) + \psi_2(t)x_t = 0.1 + 0.025t - 0.015x_t$  with its estimate

The results are illustrated in [Figure 6](#) and [Figure 7](#). In both [Figure 6](#) and [Figure 7](#), we observe that the initial points of the functions' estimators exhibit significant variance, attributed to the limited number of samples employed in the estimation process.

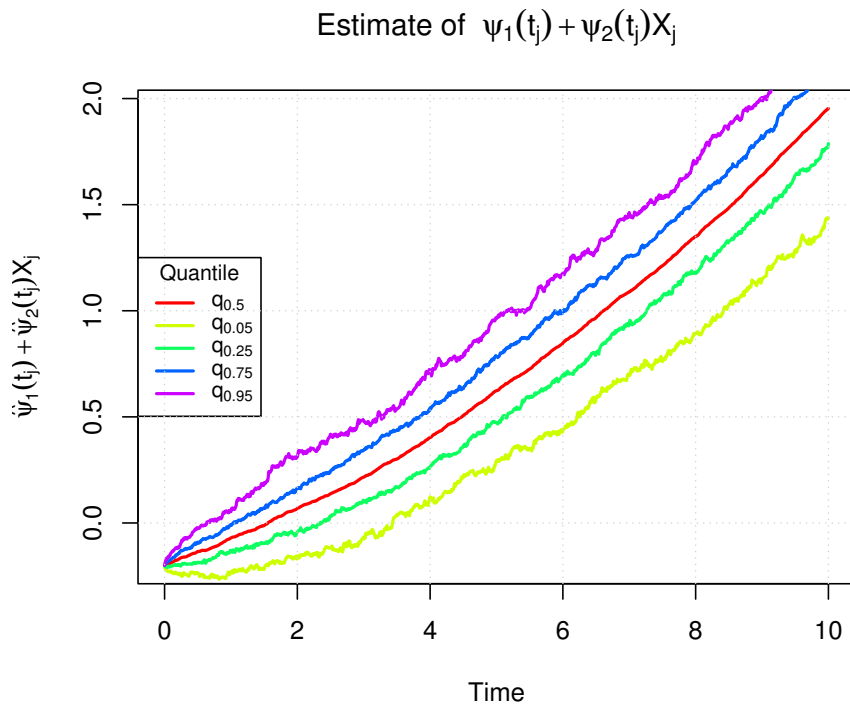


**Figure 6.** Estimation of  $\psi_1(\cdot)$  and  $\psi_2(\cdot)$  functions

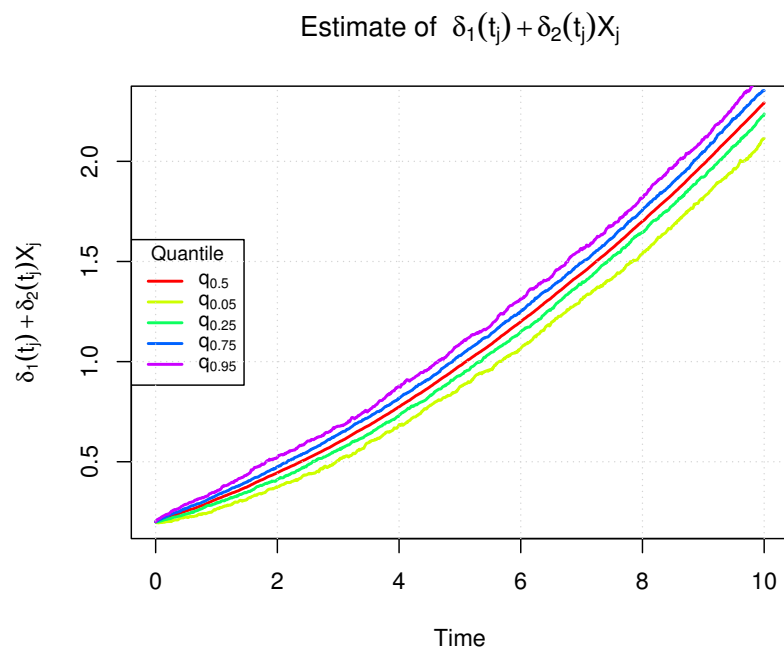


**Figure 7.** Estimation of  $\delta_1(\cdot)$  and  $\delta_2(\cdot)$  functions

Additionally, we depicted box-plots of the estimated parameters for the  $\alpha$ -stable distribution, as shown in Figure 8. For each estimated parameter, we note that the medians closely align with the theoretical values, and the variance of the estimated parameters is minimal.

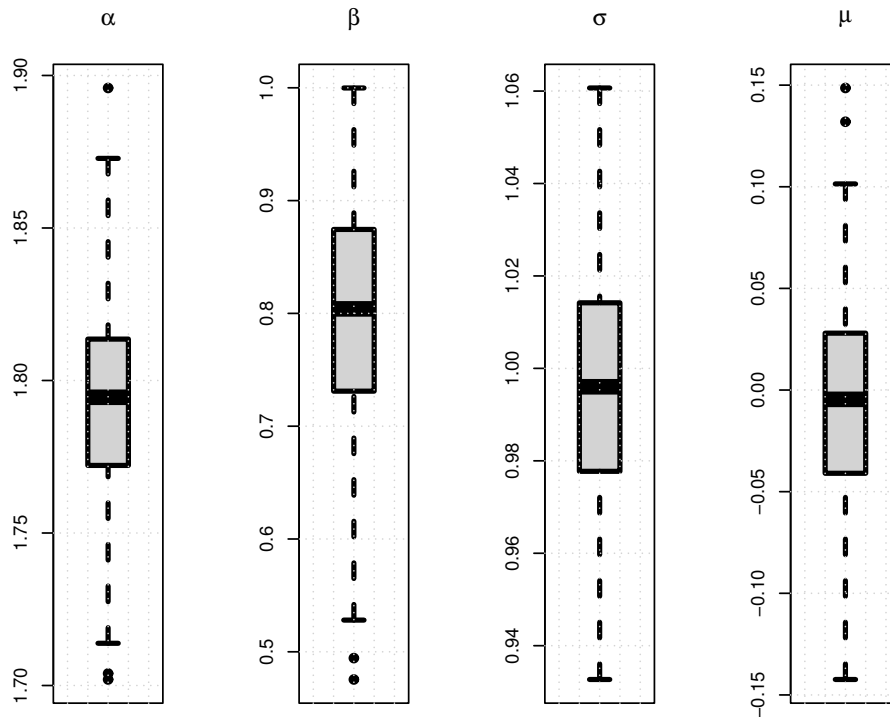


**Figure 8.** Box-plots of  $\alpha$ -stable distribution's parameters' estimates for 100 Monte Carlo simulations

## Real data analysis

In this section, we examine the real-time series that depict the prices of metals, specifically focusing on the price of gold. Our analysis aims to showcase the acceptability of the proposed model (designated as Model (8)), which is based on the  $\alpha$ -stable distribution, for all the examined time series. Additionally, we present the outcomes of long-term predictions derived from the model we have developed.

Furthermore, in the process of estimation, we set  $Max_{iter}$  to be 2, indicating two iterations of estimation. We employed the tricube as the kernel function  $K(\cdot)$  in Eq. (16). It is important to emphasize that the actual data pertaining to metals' prices is utilized solely for illustrating the introduced methodology in this context. We posit that the versatility of the proposed model extends beyond metals' prices and can be effectively applied to real data originating from diverse domains.

We examine the time series associated with the gold price, comprising a dataset with 4274 observations spanning from January 01, 2007, to December 22, 2023. Figure 9 visually represents the considered data. Observing the non-stable variance apparent in the observation vector, we address this issue by transforming the data through the Box-Cox transformation [49]:

$$\forall_t \quad X_t = \ln(X_t^*).$$

Here,  $X_t^*$  represents the vector of gold price data. The transformed vector is illustrated in Figure 9. The dataset is partitioned into a training time series, covering the period from the start of 2007 to the conclusion of December 31, 2018 (utilized for model parameter estimation), and a testing time series, spanning from 2019 to December 22, 2023 (utilized for model validation). The training time series comprises 3020 observations, while the validation time series consist of 1254 observations. In the initial phase, we determine the optimal hyperparameters, namely  $d_1^\psi, d_2^\psi, \rho_\psi, \rho_r^\psi$  and  $\eta$ , essential for minimizing the loss function (15). Following the approach outlined in Section 3, we employ MSE<sub>x</sub> (19), MSE<sub>y</sub> (18), and the Augmented Dickey–Fuller test statistic. We obtain weights  $\{\omega_j\}$  (for statistics MSE<sub>x</sub> and MSE<sub>y</sub>, as per Eqs. (18) and (19)) using the exponential smoothing method [58] with a smoothing parameter  $\phi = 8 \times 10^{-4}$ . The calculation of weights  $\{\omega_j\}$  is based on the following formula:

$$\omega_j = \frac{1 - \exp(-\phi)}{1 - \exp(-n\phi)} \exp(\phi(j - n)); \quad j = 1, \dots, n. \tag{29}$$

Utilizing specified hyperparameters ( $d_1^\psi = 0, d_2^\psi = 1, \rho_\psi = 750, \rho_r^\psi = 237.5, \eta = 0.7$ ), we proceed to estimate the  $\psi_1(\cdot)$  and  $\psi_2(\cdot)$  functions based on Model (8) employing Eq. (22).

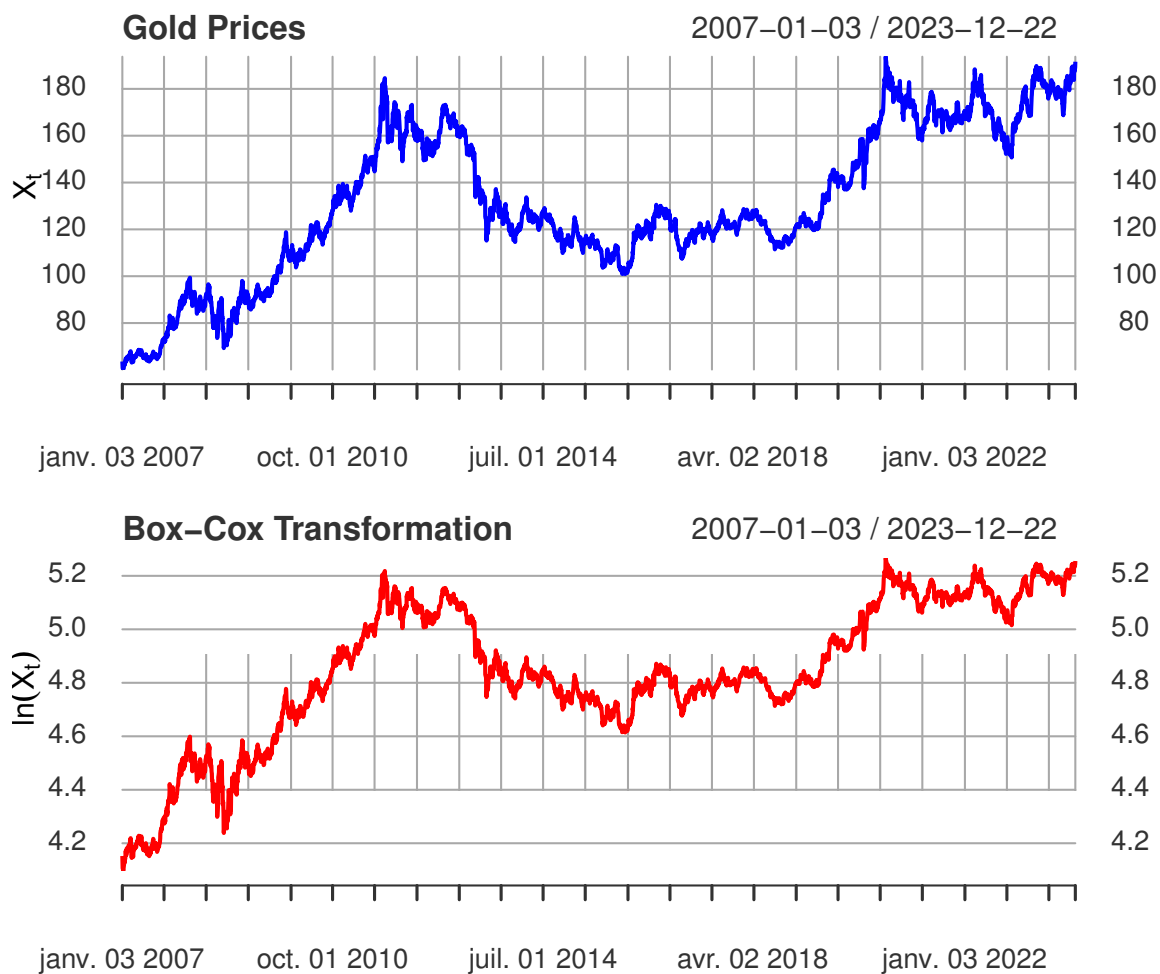


**Figure 9.** Evolution of Gold prices from January 01, 2007 to December 22, 2023

**Table 2.** Descriptive statistics Gold prices from January 01, 2007 to December 22, 2023

Data	Values						
	Min.	1st Qu.	Median	Mean	3rd Qu.	Max	S.d
Gold	60.14	113.26	125.17	131.04	161.10	193.74	31.79816

**Table 3.**  $\alpha$ -Stable law parameters extracted from the GOLD prices data

Data	$\alpha$ -Stable law parameters			
	$\alpha$	$\beta$	$\sigma$	$\mu$
GOLD	1.85150999	0.76486510	93.81960439	0.07620218

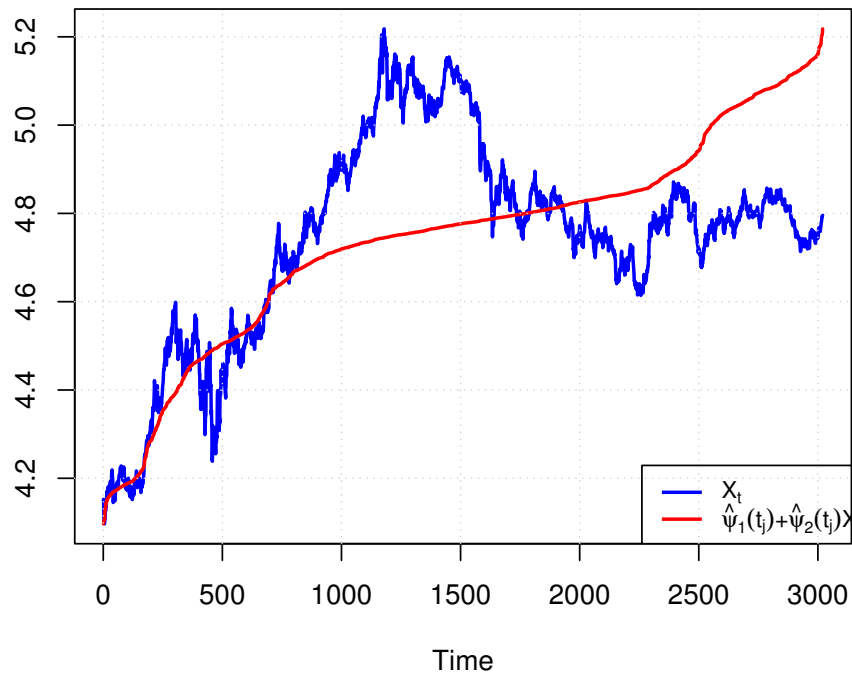


**Figure 10.** Comparison of estimated trend line to the examined time series from the first iteration of estimation of  $\psi_1(\cdot)$  and  $\psi_2(\cdot)$  functions

The resulting estimates are depicted in [Figure 10](#), demonstrating a well-fitted alignment with the observed data. However, it is noteworthy that such a fit may suggest potential overfitting. The presence of heteroskedasticity in the time series introduces complexities, as changes in the process’s variance during the initial iteration may be erroneously attributed to the  $\psi_1(\cdot)$  and  $\psi_2(\cdot)$  functions. To mitigate this challenge, we leverage an iterative estimation method, as discussed in [Section 3](#).

We computed the vector  $\{\hat{\epsilon}_j\}$  using formula (25) and determined the optimal hyperparameters for estimating the  $\delta_1(\cdot)$  and  $\delta_2(\cdot)$  functions as follows:  $d_1^\delta = 0, d_2^\delta = 0, \rho_\delta = 1000, \rho_r^\delta = 10$ . The optimal estimates were obtained by maximizing the function (24).

Subsequently, based on these estimates, their composition was calculated and visually presented in **Figure 11**, alongside a series of  $\{\hat{e}_j\}$  for comparative analysis. The results reveal that the composition of the estimates for  $\delta_1(\cdot)$  and  $\delta_2(\cdot)$  functions serves as a reliable approximation of the standard deviation of the observed time series.

Continuing, we iterate through the previously outlined steps, incorporating:

$$\zeta_{j,\delta}^{(1)} = \hat{\delta}_1(t_j) + \hat{\delta}_2(t_j)X_j.$$

The ensuing results are as follows:

i. The chosen hyperparameters for estimating  $\psi_1(\cdot)$  and  $\psi_2(\cdot)$  functions:

$$d_1^\psi = 0, d_2^\psi = 0, \rho_\psi = 937.5, \rho_r^\psi = 1.25, \eta = 8 \times 10^{-3};$$

ii. The resulting estimates for  $\psi_1(\cdot)$  and  $\psi_2(\cdot)$  functions (refer to **Figure 12**);

iii. Selected hyperparameters for estimating  $\delta_1(\cdot)$  and  $\delta_2(\cdot)$  functions

$$d_1^\delta = 1, d_2^\delta = 0, \rho_\delta = 1437.5, \rho_r^\delta = 60;$$

iv. The estimated  $\delta_1(\cdot)$  and  $\delta_2(\cdot)$  functions (see **Figure 13**).

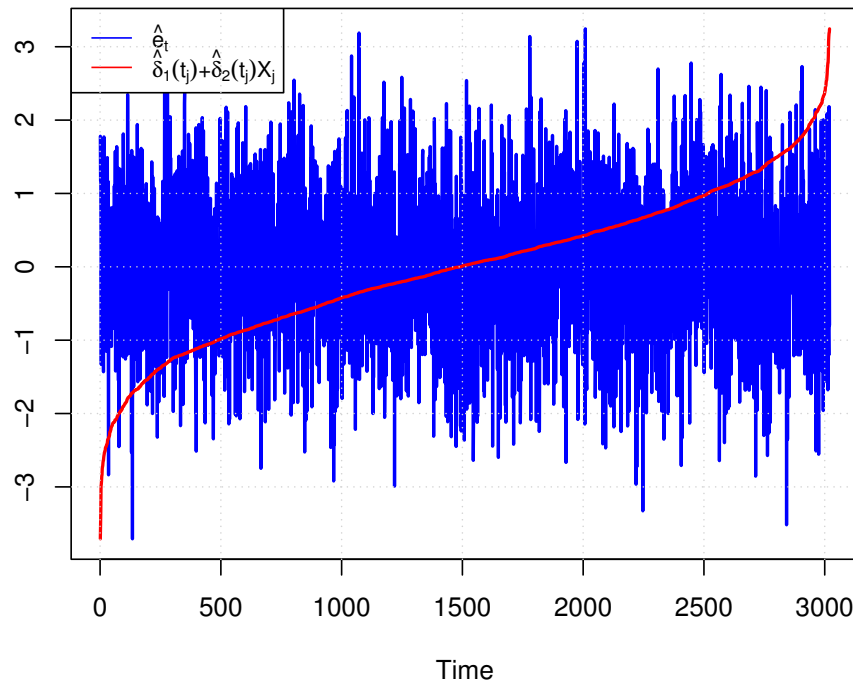


**Figure 11.** Comparison of composition  $\{\delta_1(t_j) + \delta_2(t_j)X_j\}$  with  $\{\hat{e}_j\}$  series from the first iteration of estimation of  $\delta_1(\cdot)$  and  $\delta_2(\cdot)$  functions

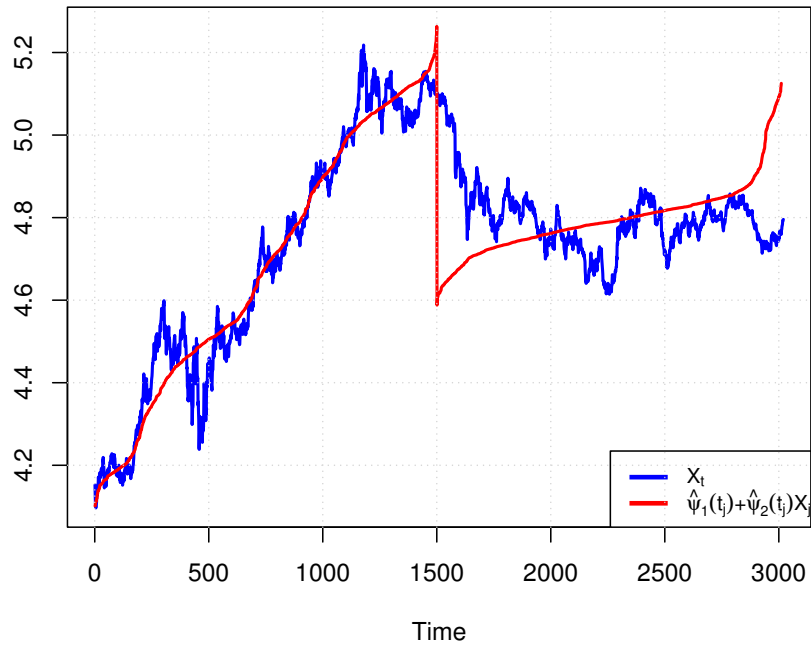


**Figure 12.** Comparison of the estimated trend line to the examined time series from the second iteration of estimation of  $\psi_1(\cdot)$  and  $\psi_2(\cdot)$  functions

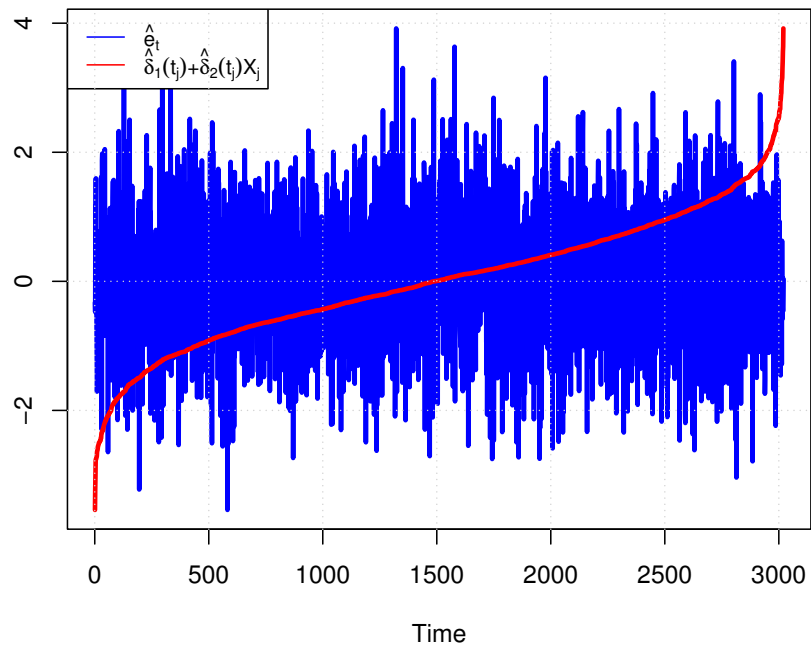


**Figure 13.** Comparison of composition  $\{\delta_1(t_j) + \delta_2(t_j)X_j\}$  with  $\{\hat{\epsilon}_j\}$  series from the second iteration of estimation of  $\delta_1(\cdot)$  and  $\delta_2(\cdot)$  functions

## 5 Conclusion

In this study, our focus has been on modeling the prices of metals for long-term predictions, specifically addressing the significant risk factors associated with metals, such as the price of gold, relevant to the KGHM mining company. We have delved into the analysis of a general time-inhomogeneous stochastic process grounded in the  $\alpha$ -stable distribution. This model serves as an extension of the classical Ornstein–Uhlenbeck process and the CKLS model previously investigated in our prior work [66].

Within the examined model, we incorporate time-dependent parameters and exhibit non-Gaussian behavior, aligning with the observed characteristics in metals' prices—namely, time-dependent features (mean and scale) and a heavy-tailed (non-Gaussian) distribution. Consequently, the proposed stochastic model is anticipated to outperform classical models with fixed coefficients and Gaussian behavior.

The primary objective of this research has been to introduce a model with time-dependent coefficients based on the  $\alpha$ -stable distribution and to propose a novel estimation procedure. Through Monte Carlo simulations, we have demonstrated the effectiveness of the proposed estimation algorithm in describing data. Furthermore, to underscore the universality of the proposed stochastic process, we have applied Model to actual data related to metals' prices, using them to illustrate the new methodology.

It is essential to note that while we have utilized metals' prices for illustration, the generality and universality of this model extend beyond financial data description. We recognize significant potential for applying the proposed model to datasets where key characteristics, such as mean or scale, undergo temporal changes, coupled with the presence of non-Gaussian behavior within the observation vector.

### Declarations

#### Use of AI tools

The authors wish to explicitly state that they have not employed any Artificial Intelligence (AI) tools or methodologies during the conception, research, drafting, or any phase of the creation of this article. The entire content has been meticulously crafted by the authors without reliance on AI assistance or automation.

#### Data availability statement

The real dataset used in this work is available online and free of charge. The R codes for the simulation study are available from the author on reasonable request.

#### Ethical approval (optional)

The authors state that this research complies with ethical standards. This research does not involve either human participants or animals.

#### Consent for publication

Not applicable

#### Conflicts of interest

The authors declare that they have no conflict of interest.

## Funding

No funding was obtained for this study.

## Author's contributions

C.D.B.: Conceptualization, Methodology, Software, Validation, Data Curation, Writing - Original. C.G. and M.E.K.: Writing - Review & Editing, Supervision. All authors have read and agreed to the published version of the manuscript.

## Acknowledgements

The authors express their sincere gratitude to the associate editor and referees for their thorough review and valuable comments and suggestions, which significantly contributed to enhancing the quality of the paper.

## References

- [1] Din, A., Sabbar, Y. and Wu, P. A novel stochastic Hepatitis B virus epidemic model with second-order multiplicative  $\alpha$ -stable noise and real data. *Acta Mathematica Scientia*, 44, 752-788, (2024). [[CrossRef](#)]
- [2] Zhang, G.P. Time series forecasting using a hybrid ARIMA and neural network model. *Neurocomputing*, 50, 159–175, (2003). [[CrossRef](#)]
- [3] Nisar, K.S. and Sabbar, Y. Long-run analysis of a perturbed HIV/AIDS model with antiretroviral therapy and heavy-tailed increments performed by tempered stable Lévy jumps. *Alexandria Engineering Journal*, 78, 498-516, (2023). [[CrossRef](#)]
- [4] Sabbar, Y., Khan, A., Din, A. and Tilioua, M. New method to investigate the impact of independent quadratic  $\alpha$ -stable Poisson jumps on the dynamics of a disease under vaccination strategy. *Fractal and Fractional*, 7(3), 226, (2023). [[CrossRef](#)]
- [5] Sabbar, Y. Asymptotic extinction and persistence of a perturbed epidemic model with different intervention measures and standard Lévy jumps. *Bulletin of Biomathematics*, 1(1), 58-77, (2023). [[CrossRef](#)]
- [6] Ru, Y. and Ren, H.J. Application of ARMA model in forecasting aluminum price. in: *Applied Mechanics and Materials*, Vol. 155, Trans Tech Publ, pp. 66-71, (2012). [[CrossRef](#)]
- [7] Rossen, A. What are metal prices like? Co-movement, price cycles and long-run trends. *Resources Policy*, 45, 255–276, (2015). [[CrossRef](#)]
- [8] Haque, M.A., Topal, E. and Lilford, E. Iron ore prices and the value of the Australian dollar. *Mining Technology*, 124(2), 107-120, (2015). [[CrossRef](#)]
- [9] Cortez, C.T., Saydam, S., Coulton, J. and Sammut, C. Alternative techniques for forecasting mineral commodity prices. *International Journal of Mining Science and Technology*, 28(2), 309-322, (2018). [[CrossRef](#)]
- [10] Lee, J., List, J.A. and Strazicich, M.C. Non-renewable resource prices: Deterministic or stochastic trends?. *Journal of Environmental Economics and Management*, 51(3), 354–370, (2006). [[CrossRef](#)]
- [11] Uhlenbeck, G.E. and Ornstein, L.S. On the theory of the Brownian motion. *Physical Review*, 36(5), 823, (1930). [[CrossRef](#)]
- [12] Vasicek, O. An equilibrium characterization of the term structure. *Journal of Financial Economics*, 5(2), 177-188, (1977). [[CrossRef](#)]

- [13] Wylomanska, A. The dependence structure for symmetric  $\alpha$ -stable CARMA (p, q) processes. In *Proceedings, Workshop on Cyclostationary Systems and Their Applications (CSTA)*, pp. 189-206, Springer, (2014, February).
- [14] Brockwell, P.J. Continuous-time ARMA processes. *HandBook of Statistics*, 19, 249-276, (2001). [[CrossRef](#)]
- [15] Tully, E. and Lucey, B.M. A power GARCH examination of the gold market. *Research in International Business and Finance*, 21(2), 316-325, (2007). [[CrossRef](#)]
- [16] Wyłomańska, A. Measures of dependence for Ornstein–Uhlenbeck process with tempered stable distribution. *Acta Physica Polonica B*, 42(10), 2049-2062, (2011). [[CrossRef](#)]
- [17] Obuchowski, J. and WYŁOMANSKA, A. The Ornstein–Uhlenbeck process with non-Gaussian structure. *Acta Physica Polonica B*, 44(5), 1123-1136, (2013). [[CrossRef](#)]
- [18] Nolan, J.P. Computational aspects of stable distributions. *Wiley Interdisciplinary Reviews: Computational Statistics*, 14(4), e1569, (2021). [[CrossRef](#)]
- [19] Zolotarev V.M., On representation of stable laws by integrals. *Selected Translation in Mathematical Statistics and Probability*, 6, 84-88, (1966).
- [20] McCulloch, J.H. Simple consistent estimators of stable distribution parameters. *Communications in Statistics-Simulation and Computation*, 15(4), 1109–1136, (1986). [[CrossRef](#)]
- [21] Ho, T.S.Y., Lee, S.B. Term structure movements and pricing interest rate contingent claims. *The Journal of Finance*, 41(5), 1011-1029, (1986). [[CrossRef](#)]
- [22] Hull, J. and White, A. Pricing interest-rate-derivative securities. *The Review of Financial Studies*, 3(4), 573-592, (1990). [[CrossRef](#)]
- [23] Nolan, J.P. *Univariate Stable Distributions: Models for Heavy Tailed Data*. Springer: Switzerland, (2020). [[CrossRef](#)]
- [24] Zhang, S. and Zhang, X. A least squares estimator for discretely observed Ornstein-Uhlenbeck processes driven by symmetric  $\alpha$ -stable motions. *Annals of the Institute of Statistical Mathematics*, 65, 89-103, (2013). [[CrossRef](#)]
- [25] Hu, Y. and Long, H. Parameter estimation for Ornstein–Uhlenbeck processes driven by  $\alpha$ -stable Lévy motions. *Communications on Stochastic Analysis*, 1(2), 175-192, (2007). [[CrossRef](#)]
- [26] Cui, H. Estimation in partial linear EV models with replicated observations. *Science in China Series A: Mathematics*, 47, 144, (2004). [[CrossRef](#)]
- [27] Fan, J., Jiang, J., Zhang, C. and Zhou, Z. Time-dependent diffusion models for term structure dynamics. *Statistica Sinica*, 13(4), 965-992, (2003). [[CrossRef](#)]
- [28] Lévy P. Théorie des erreurs. La loi de Gauss et les lois exceptionnelles. *Bulletin de la Société Mathématique de France*, 52, 49-85, (1924). [[CrossRef](#)]
- [29] McCulloch, J.H. 13 Financial applications of stable distributions. *Handbook of Statistics*, 14, 393-425, (1996). [[CrossRef](#)]
- [30] Mittnik, S., Rachev, S.T., Doganoglu, T. and Chenyao, D. Maximum likelihood estimation of stable Paretian models. *Mathematical and Computer Modelling*, 29(10-12), 275–293, (1999). [[CrossRef](#)]
- [31] Nolan, J.P. Modeling financial data with stable distributions. In *Handbook of Heavy Tailed Distributions in Finance* (pp. 105–130). North-Holland, Holland: Elsevier, (2003). [[CrossRef](#)]
- [32] Rachev, S.T. and Mittnik, S. *Stable Paretian models in finance*. New York: Wiley: (2000).

- 
- [33] Samorodnitsky, G., Taqqu, M.S. and Linde, R.W. *Stable non-gaussian random processes: stochastic models with infinite variance*. New York; London: Chapman & Hall, (1994).
- [34] Zolotarev, A. *One-Dimensional Stable Distributions*. USA: American Mathematical Society, Providence, (1986).
- [35] Fama, E.F. and Roll, R. Parameter estimates for symmetric stable distributions. *Journal of the American Statistical Association*, 66, 331–338, (1971). [[CrossRef](#)]
- [36] Mandelbrot, B.B. The variation of certain speculative prices. In: *Fractals and Scaling in Finance*. New York: Springer, (1997). [[CrossRef](#)]
- [37] Bachelier, L. *Théorie de la spéculation*. Annales scientifiques de l'École Normale Supérieure, Serie 3, Vol 17, 21-86, (1900). [[CrossRef](#)]
- [38] Chambers, J.M., Mallows, C.L. and Stuck, B.W. A method for simulating stable random variables. *Journal of the American Statistical Association*, 71, 340–344, (1976). [[CrossRef](#)]
- [39] Koutrouvelis, I.A. An iterative procedure for the estimation of the parameters of stable laws. *Communications in Statistics-Simulation and Computation*, 10, 17-28, (1981). [[CrossRef](#)]
- [40] Koutrouvelis, I.A. Regression-type estimation of the parameters of stable laws. *Journal of the American Statistical Association*, 75, 918–928, (1980). [[CrossRef](#)]
- [41] Press, S.J. Estimation in univariate and multivariate stable distributions. *Journal of the American Statistical Association*, 67, 842–846, (1972). [[CrossRef](#)]
- [42] Weron, R. *Performance of the estimators of stable law parameters*. Hugo Steinhaus Center, Wroclaw University of Technology, HSC Research Reports, HSC/95/01, (1995).
- [43] Nolan, J.P. Numerical calculation of stable densities and distribution functions. *Communications in Statistics. Stochastic Models*, 13(4), 759–774, (1997). [[CrossRef](#)]
- [44] Weron, A. and Weron, R. *Inzynieria finansowa*. HSC Books: Wydawnictwo Naukowo-Techniczne, Warszawa, (1998).
- [45] Revuz, D. and Yor, M. *Continuous Martingales and Brownian Motion* (Vol. 293). Springer: Berlin, pp. 14-39, (1991).
- [46] Merton, R.C. Theory of rational option pricing. *The Bell Journal of Economics and Management Science*, 4(1), 141-183, (1973). [[CrossRef](#)]
- [47] Brennan, M.J. and Schwartz, E.S. An equilibrium model of bond pricing and a test of market efficiency. *Journal of Financial and Quantitative Analysis*, 17(3), 301-329, (1982). [[CrossRef](#)]
- [48] Dothan, L.U. On the term structure of interest rates. *Journal of Financial Economics*, 6(1), 59-69, (1978). [[CrossRef](#)]
- [49] Cox, J.C., Ingersoll Jr., J.E. and Ross, S.A. A theory of the term structure of interest rates. *Econometrica*, 53(2), 385-407, (1985).
- [50] Black, F. and Karasinski, P. Bond and option pricing when short rates are lognormal. *Financial Analysts Journal*, 47(4), 52-59, (1991). [[CrossRef](#)]
- [51] Hastie, T., Friedman, J. and Tibshirani, R. *The Elements of Statistical Learning: Data Mining, Inference, and Prediction*. New York: Springer, (2009). [[CrossRef](#)]
- [52] Marsden, J. and Weinstein, A. *Calculus II*, Springer: New York, (1985).
- [53] Saleh, A.M.E., Arashi, M. and Tabatabaey, S.M.M. *Statistical Inference for Models with Multivariate T-Distributed Errors*. John Wiley & Sons: USA, (2014).
- [54] Cont, R. *Encyclopedia of Quantitative Finance*. (Vol. 4). John Wiley & Sons: USA, (2010).

- [55] W Cleveland, W.S. Robust locally weighted regression and smoothing scatterplots. *Journal of the American Statistical Association*, 74(368), 829-836, (1979). [[CrossRef](#)]
- [56] Jaditz, T. and Riddick, L.A. Time-series near-neighbor regression. *Studies in Nonlinear Dynamics & Econometrics*, 4(1), 35-44, (2000). [[CrossRef](#)]
- [57] Elliott, G., Rothenberg, T.J. and Stock, J.H. Efficient tests for an autoregressive unit root. *Econometrica*, 64(4), 813-836, (1996). [[CrossRef](#)]
- [58] Pozzi, F., Di Matteo, T. and Aste, T. Exponential smoothing weighted correlations. *The European Physical Journal B*, 85(175), 1-21, (2012). [[CrossRef](#)]
- [59] Breusch, T.S. and Pagan, A.R. The lagrange multiplier test and its applications to model specifications in econometrics. *The Review of Economic Studies*, 47(1), 239-253, (1980). [[CrossRef](#)]
- [60] Nolan, J.P. Maximum likelihood estimation of stable parameters. In *Levy processes: Theory and applications*. (pp. 379–400). Boston: Birkhauser, (2001).
- [61] Tan, P. and Drossos, C. Invariance properties of maximum likelihood estimators. *Mathematics Magazine*, 48, 37-41, (1975). [[CrossRef](#)]
- [62] Shanno, D.F. Conditioning of quasi-Newton methods for function minimization. *Mathematics of Computation*, 24(111), 647-656, (1970).
- [63] Fox, L. and Mayers, D.F. *Numerical Solution of Ordinary Differential Equations*. Chapman and Hall: London, (1987). [[CrossRef](#)]
- [64] Stephens, M.A. EDF statistics for goodness of fit and some comparisons. *Journal of the American Statistical Association*, 69, 730-737, (1974). [[CrossRef](#)]
- [65] Brandimarte, P. *HandBook in Monte Carlo Simulation: Applications in Financial Engineering, Risk Management, and Economics*. John Wiley & Sons: USA, (2014).
- [66] Sikora, G., Michalak, A., Bielak, Ł., Miśta, P. and Wyłomańska, A. Stochastic modeling of currency exchange rates with novel validation techniques. *Physica A: Statistical Mechanics and its Applications*, 523, 1202-1215, (2019). [[CrossRef](#)]

Mathematical Modelling and Numerical Simulation with Applications (MMNSA)  
(<https://dergipark.org.tr/en/pub/mmnsa>)



**Copyright:** © 2024 by the authors. This work is licensed under a Creative Commons Attribution 4.0 (CC BY) International License. The authors retain ownership of the copyright for their article, but they allow anyone to download, reuse, reprint, modify, distribute, and/or copy articles in MMNSA, so long as the original authors and source are credited. To see the complete license contents, please visit (<http://creativecommons.org/licenses/by/4.0/>).

**How to cite this article:** Coulibaly, B.D., Ghizlane, C. & Khomssi, M.E. (2024). An approach to stochastic differential equations for long-term forecasting in the presence of  $\alpha$ -stable noise: an application to gold prices. *Mathematical Modelling and Numerical Simulation with Applications*, 4(2), 165-192. <https://doi.org/10.53391/mmnsa.1416148>



RESEARCH PAPER

## Finite element static analysis of polyurethane-sandwiched skewed bridge decks

Ashwin Anand <sup>1,†</sup>, Deepak Kumar Singh <sup>1,†</sup> and Preeti Agarwal <sup>2,\*</sup>,<sup>†</sup>

<sup>1</sup>Department of Civil Engineering, Amity School of Engineering and Technology, Amity University Patna, Bihar 801503, India, <sup>2</sup>Department of Civil Engineering, Amity School of Engineering and Technology, Amity University Lucknow Campus, Uttar Pradesh 226010, India

\* Corresponding Author

† ashwin.anand@s.amity.edu (Ashwin Anand); dksingh@ptn.amity.edu (Deepak Kumar Singh); pagarwal@lko.amity.edu (Preeti Agarwal)

### Abstract

Bridge decks are the surface structure of bridges that carry the weight of the vehicles. But nowadays, the need for a sustainable approach is required. So, the use of a sustainable material for construction and retrofitting purposes is the need of the hour. In the present study, a novel synthetic material polyurethane has been used in the sandwiched deck of the bridges. The study deals with the variation in skew angles to determine the response of the sandwiched bridge deck under Indian loading conditions. In this study, the response of deflection, equivalent stress, and stresses in X and Y directions on the bridge deck due to the variation in skewness, the thickness of the steel plate and the thickness of polyurethane deck are analysed using finite element method. Further, the bridge deck is sandwiched using steel and polyurethane having different thicknesses, and the responses are recorded. Afterward, a bridge deck is modelled using only polyurethane, to pursue sustainability and justify the RRR (reduce, reuse, and recycle) concept of waste management. The models are developed and analysed using ANSYS workbench. On increasing the skew angle for the sandwiched deck, the deflection and stresses are decreased; so, the skewed deck is more effective than the straight one. It is found that the deflection and stresses are reduced about 8 times and 4 times respectively, when the thickness of polyurethane is increased from 250 mm to 1500 mm. Therefore, it is a good and effective solution for pedestrian bridges and many other such small-scale applications.

**Keywords:** Sandwiched bridge deck; finite element method; ANSYS workbench; steel; polyurethane

**AMS 2020 Classification:** 74S05; 74-04; 74-10

## 1 Introduction

Bridge structures are an integral part of the transportation network and are essential for connecting different regions, facilitating economic growth, and improving the overall quality of life. Bridge

decks are the surface structures of bridges that carry the weight of the vehicles and pedestrians crossing over them. The design of bridge decks varies depending on the span, traffic volume, material availability, etc. The primary function of the bridge deck is to provide a safe and stable surface for the traffic to cross. Bridge decks can be categorised into cable-stayed, arch, box-girder, truss decks, etc., each with its unique characteristics. Isotropic bridge decks, constructed with homogeneous materials, provide a reliable and cost-effective option for small to medium-span bridges, although they require regular maintenance to prevent corrosion as most of such bridges are steel bridges. Orthotropic decks, made of steel or composite materials, provide strength and durability while reducing the weight of the bridge structure. They are commonly used for long-span bridges and offer advantages such as corrosion resistance and excellent skid resistance. However, they require specialised construction skills and equipment and have lower stiffness compared to isotropic decks. Despite the higher construction cost, orthotropic decks are a popular choice for high-traffic areas due to their durability and load-carrying capacity. Despite extensive research on the impact of skew angle on bridge deck behaviour, the dissimilarities in behaviour between isotropic and orthotropic bridge decks at varying skew angles are not well understood. Isotropic decks have uniform steel plate properties, while orthotropic decks consist of a core with steel faceplates exhibiting distinct mechanical properties in different directions. Examining the disparities in behaviour between these deck types, especially in skewed bridge scenarios, is crucial. Several important literature have been discussed in the next paragraph to show the importance of carrying out analysis on the bridge decks by varying the skewness.

The various RC (reinforced concrete) bridges under dynamic loads are analysed and evaluated the "impact factor" to determine their behaviour [1]. The dynamic effects of vehicles on highway bridge decks are analysed. It considers rough pavement surfaces and employs a probabilistic model and finite element approach [2]. The Finite Prism method for dynamic bridge analysis under moving vehicles, utilising explicit time integration and uncoupled equations is employed [3]. The trapezoidal rib orthotropic bridge deck systems are analysed using the finite element method and found that a non-uniform stress pattern should be employed to address local buckling concerns under negative bending moment and axial forces [4]. The AASHTO (American Association of State Highway and Transportation Officials) specifications and LRFD (Load and Resistance Factor Design) procedures with finite-element analysis results for skewed reinforced concrete bridges are compared and are shown overestimation of the maximum moment and differences in longitudinal moment ratios [5]. Stress concentration found at rib intersections in orthotropic steel bridge decks, with high-stress levels in cut-outs [6].

The effect of skew angle is analysed on bridge deck behaviour, observing changes in reaction force, bending moment, torsional moment, and transverse moment [7]. The steel plate reinforcement systems are studied for orthotropic decks, identifying fatigue damage caused by shear stresses in adhesive and core interfaces [8]. Authors found that deflection and bending moments decrease with increasing skew angle in reinforced concrete bridges [9], also the impact of cross-frame stiffness and spacing on fatigue damage in steel bridges are highlighted [10]. The stiffened plates are analysed using the finite element method, conducting a parametric study on stiffener geometry's influence on deflection and stress while keeping the material volume constant, and verifying results with reported data [11]. The versatile steel bridge alternatives are proposed based on span length [12]. The dynamic behaviour of a hybrid girder bridge is analysed with concrete-filled steel tube arches under moving vehicles. The study highlights the impact effects, ride comfort, and the need for further research on this bridge type [13]. Authors have applied semi-analytical GBT (Generalised Beam Theory) formulation to analyse dynamic behaviour of high-speed railway bridge decks. It investigates a real viaduct, capturing enhanced response due to resonance during high-speed train crossings [14]. The buckling behaviour of steel-polyurethane sandwiched bridge

decks is studied to determine the stress variations across the deck for recommending a specification for deck thickness and stiffening rib spacing [15]. A new orthotropic steel-concrete composite deck system with improved crack control is investigated for high load capacity [16].

The fluid-structure interaction of stiffened lock gates is investigated using free vibration analysis and numerical simulations [17]. The dynamic pressure distribution of rectangular lock gates is studied under harmonic ground acceleration considering fluid effects [18]. The effect of skew angle on reinforced concrete slab bridges is analysed and observed changes in longitudinal and transverse moments [19]. The UHPC (Ultrahigh Performance Concrete)-orthotropic steel composite decks are studied and noted cracks in rib web and shear connection failure [20]. The effect of fluid on the natural frequencies of a vertical lock gate is analysed using computational analysis [21]. The skewness effect on RC box-girder bridge is investigated subjected to IRC loading [22]. The dynamic behaviour of reinforced concrete bridges is analysed with T-beam and I-girder systems. Seismic, soil, and vehicular factors are considered, using response spectrum analysis in CSiBridge software [23]. A response surface methodology-based optimisation approach is proposed for steel bridge deck systems to simplify the design process [24]. Bridges with high skew angles may lead to performance issues [25]. Skew slab bridges are analysed using ANSYS [26]. The flexural performance of pultruded glass fibre reinforced polymer (P-GFRP) composite beams is investigated in this work by combining experimental, theoretical, and finite element analytic techniques, and the results show good agreement between the numerical and experimental approaches [27]. The multiscale analysis of pultruded fiber-reinforced polymer composite beams is presented, demonstrating remarkable consistency between numerical, experimental, and analytical results, therefore confirming the suggested formulations [28]. Finite element analysis is performed to explore the behaviour of dapped end prefabricated concrete purlins (PCPs), proposing a carbon fiber reinforced polymer (CFRP) reinforcement strategy, particularly highlighting the crucial role of CFRP ply orientation in enhancing shear capacity [29].

A parametric study on skewed composite bridges is conducted [30], and the performance of isotropic and orthotropic sandwiched bridge decks under wheel loading is investigated [31]. The dynamic response of stiffened bridge decks is considered under moving loads. Different stiffeners, load velocities, and traversing paths are considered [32]. The effect of surrounding fluid in a dam-reservoir system on a stiffened lock gate structure subjected to external acceleration is investigated [33]. Fibre Metal Laminate (FML) machining technique is used and identifies the optimal parameters to improve hole quality for the benefit of industry and research [34]. The impact of wrapping with GFRP and CFRP composites on the flexural performance of reinforced concrete-filled pultruded GFRP profile hybrid beams is studied. The results demonstrate notable improvements in load-carrying capacities and structural performance ratios [35]. The effects of fatigue cracks on vibration characteristics are studied [36]. Authors have compared the analysis and results of a two-lane simply supported RC T-frame bridge deck. Dynamic analysis is performed at various span lengths, considering different vehicle databases [37]. The free vibration characteristics of box-girder bridges are evaluated [38]. The natural frequencies of a stiffened lock gate structure interacting with an inviscid fluid are determined. Results are compared with an unstiffened lock gate, considering different geometries and fluid extents [39]. An arc-shaped stiffener is proposed for enhanced fatigue resistance in long-span steel bridges [40]. The static behaviour of steel-concrete-steel sandwiched plates is analysed under different loads using ANSYS Workbench [41]. The effect of skewness on prestressed box-girder bridges is studied [42]. The static and dynamic responses of eccentrically stiffened plates are evaluated [43]. The effect of fluid on a locked gate in a dam-reservoir system using Mindlin's plate theory and the method of separation of variables is investigated. The study has considered sinusoidal excitation and examined the dynamic pressure variation [44].

The understanding of the differences between steel and sandwiched decks for different skew angles is very limited. The use of polyurethane in conjunction with steel for deck construction is an innovative method. The manuscript investigates the structural consequences and advantages of this hybrid material, so contributing to a better knowledge of new materials in structural engineering. Also, very few studies are available on Indian loading conditions. The manuscript tackles a specific and critical issue of structural design by focusing on Indian loading conditions. The numerical technique enables a complete analysis of the structural behaviour of the polyurethane steel deck under various loading situations, providing a comprehensive insight that goes beyond what typical analytical methods can provide. So, in this study, steel and sandwiched decks are analysed and compared for various skew angles, viz.,  $0^\circ$ ,  $10^\circ$ ,  $20^\circ$ ,  $30^\circ$ ,  $40^\circ$ ,  $50^\circ$ , and  $60^\circ$  under Indian loading conditions. Also, decks are modelled and analysed using only polyurethane for a better understanding of the material and its usage considering the sustainability and RRR concepts. The displacement and stresses under Indian loading conditions are determined for all bridge models using the finite element method. This comparison gives an insight into the relative advantages and disadvantages of the new material, assisting in structural design project decision-making. The study has been conducted according to the flow diagram as shown in [Figure 1](#).

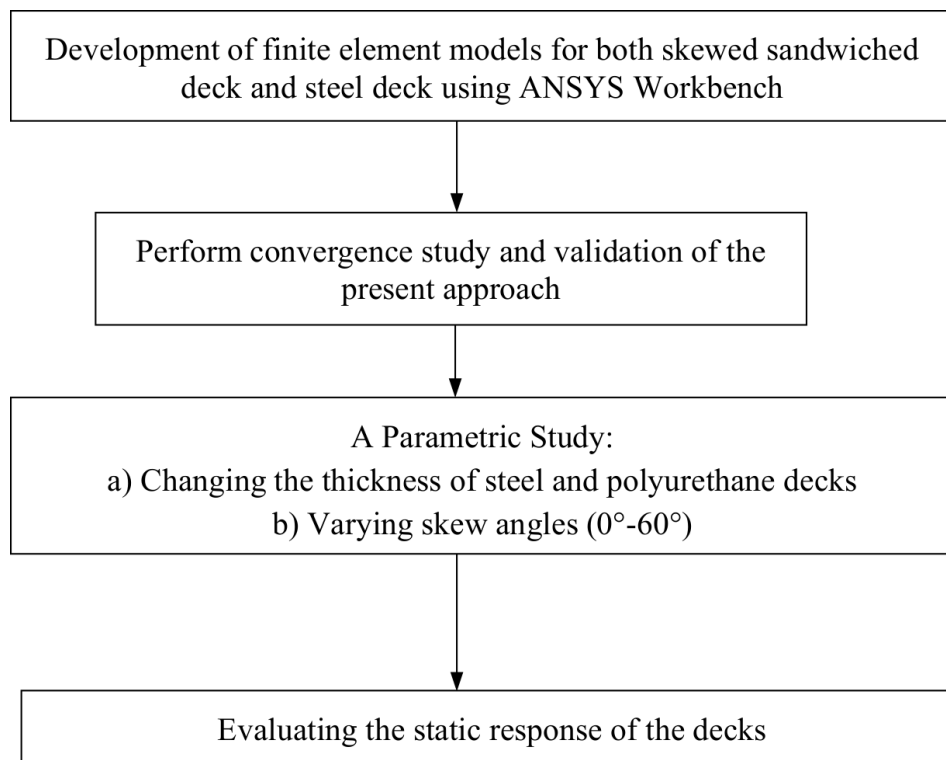


**Figure 1.** Flow diagram of the study

## 2 Modelling process and validation

The finite element method (FEM) is used for the analysis with the help of ANSYS Workbench. FEM involves dividing a structure into discrete elements interconnected at nodal points, with individual element stiffness matrices assembled based on assumed displacement or stress patterns. A model considered by Agarwal et al. [31] is reproduced for validating the present approach, as shown in [Figure 2](#). The model of the bridge deck considered is of length 720 mm, width 350 mm and thickness 4 mm for steel isotropic deck, and for sandwiched deck,  $t_s = 2$  mm (both lower and upper steel plates) and  $t_p = 10$  mm, i.e., total thickness = 14 mm. The results obtained from the

present study are validated with the experimental and numerical results of Shan and Yi (2016) [14], and Agarwal et al. (2021) [31], respectively. The deck is simply supported on all four edges,

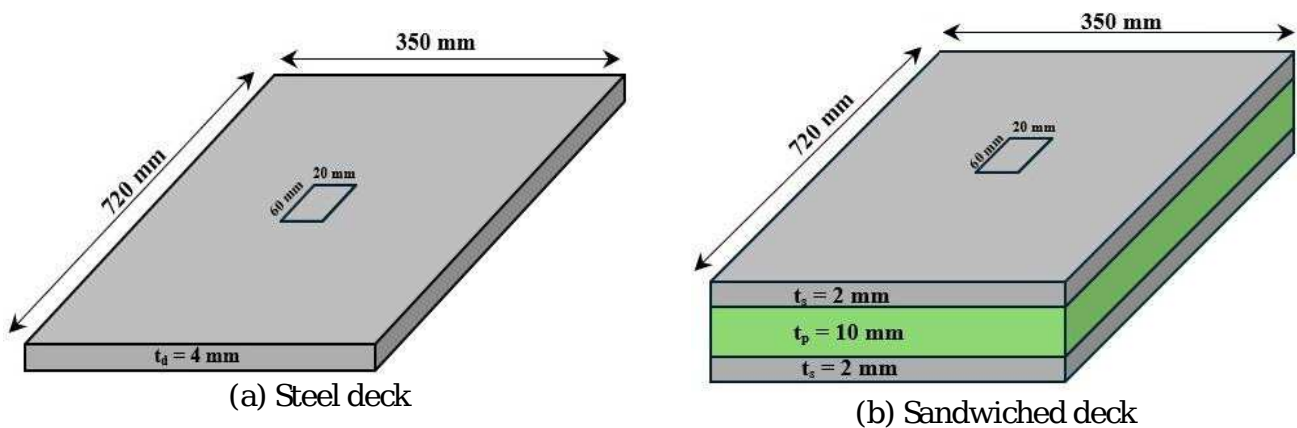


Figure 2. Plan of the deck for validation

and a uniformly distributed area load of 1.667 MPa is applied on 60 mm  $\times$  20 mm area at the centre, as specified in Agarwal et al. (2021) [31]. The mesh size of the element is taken as 10 mm after the conduction of a convergence study. The stresses are evaluated at regular intervals of 10 mm in both the longitudinal and transverse orientations and the location of the points are shown in Figure 3. The results obtained are compared with Agarwal et al. (2021) [31], and Shan and Yi

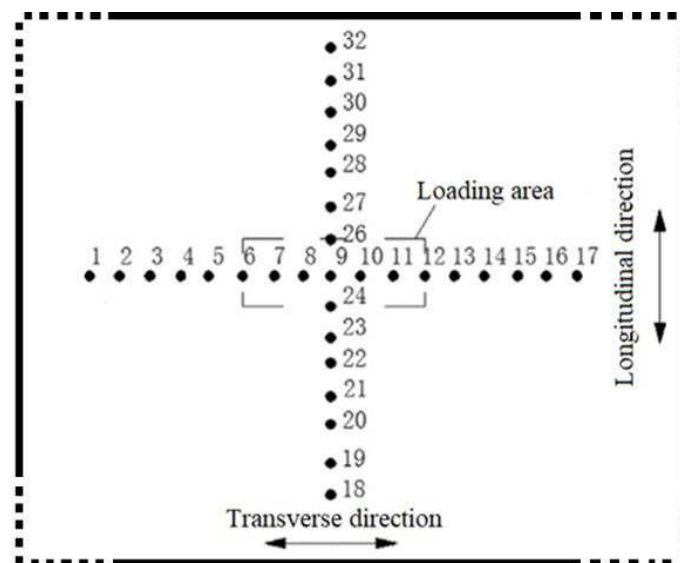


Figure 3. Points of stress calculation on the deck

(2016) [14] and are demonstrated in Figure 4 and Figure 5. The present results were found to be in close agreement with the results reported by Agarwal et al. (2021) [31], and Shan and Yi (2016) [14].

### 3 Bridge deck model

Deflection and stresses are evaluated for simply supported isotropic and sandwiched decks. A bridge deck of length 20 m, and width 5.76 m is modelled for analysis. Then convergence study is carried out to find the optimum mesh size for the present study. It is performed on an isotropic

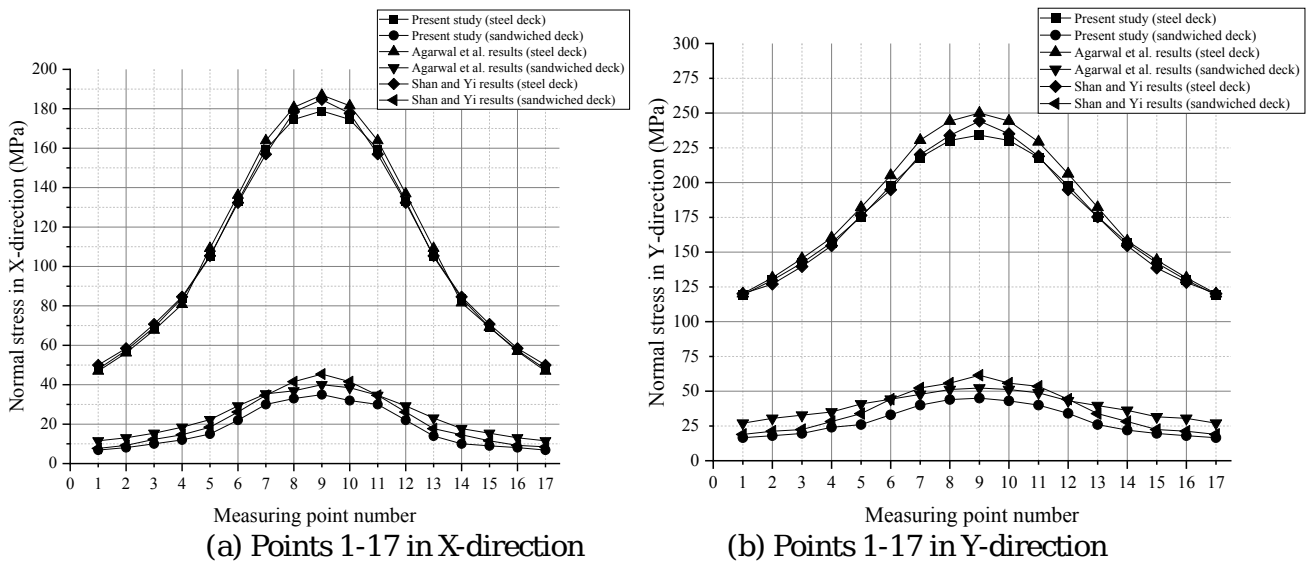


Figure 4. Stresses in X-direction and Y-direction

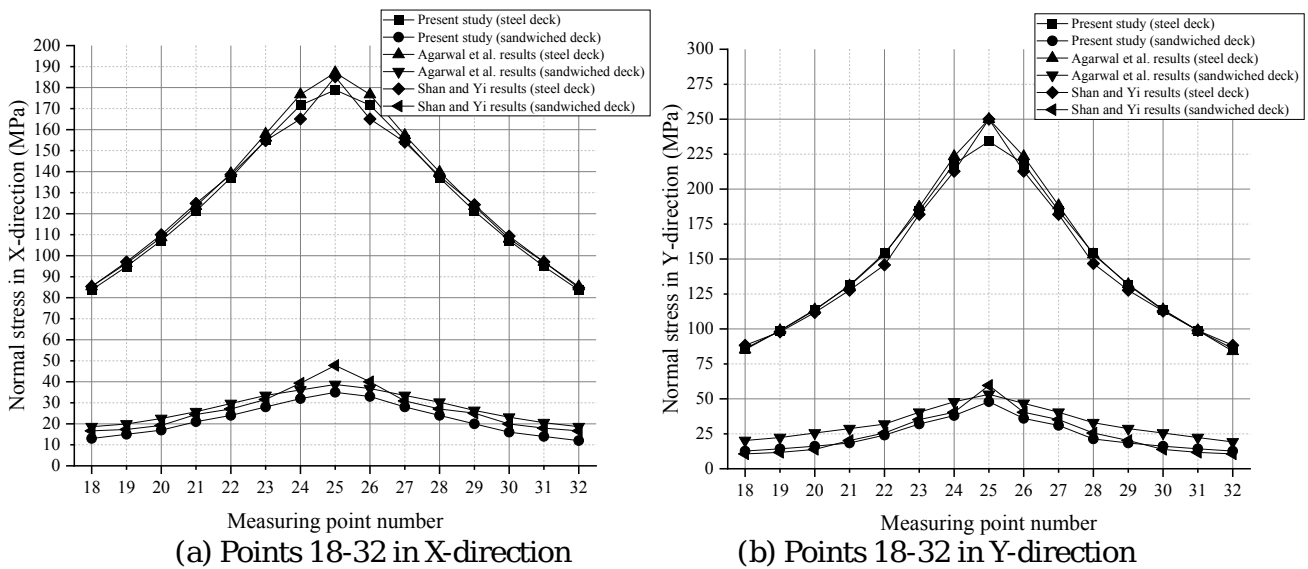


Figure 5. Stresses in X-direction and Y-direction

steel bridge deck of length 20 m, width 5.76 m, and thickness 150 mm, with the evaluation of maximum deflection and maximum equivalent stress by applying 70R wheeled load ‘L’ type (IRC:6-2017) [45]. Maximum deflection and maximum equivalent stress are plotted against mesh size as shown in Figure 6(a), and Figure 6(b), respectively. It is observed that the results converge after the mesh size of 100 mm. So, the mesh size of 100 mm is considered for further analysis. In this study, 3-noded triangular elements and 4-noded rectangular elements with 6 degrees of freedom at each node are used for discretisation. The presence of 4-noded rectangular elements is more, as 3-noded triangular elements accommodate due to the skewness. The details of these elements are shown in Figure 7.

#### 4 Numerical results and discussions

A parametric study has been performed using several examples to estimate the effect of varying skewness in isotropic and sandwiched bridge decks. The materials used in the study are steel and polyurethane, and the properties of these materials are tabulated in Table 1.

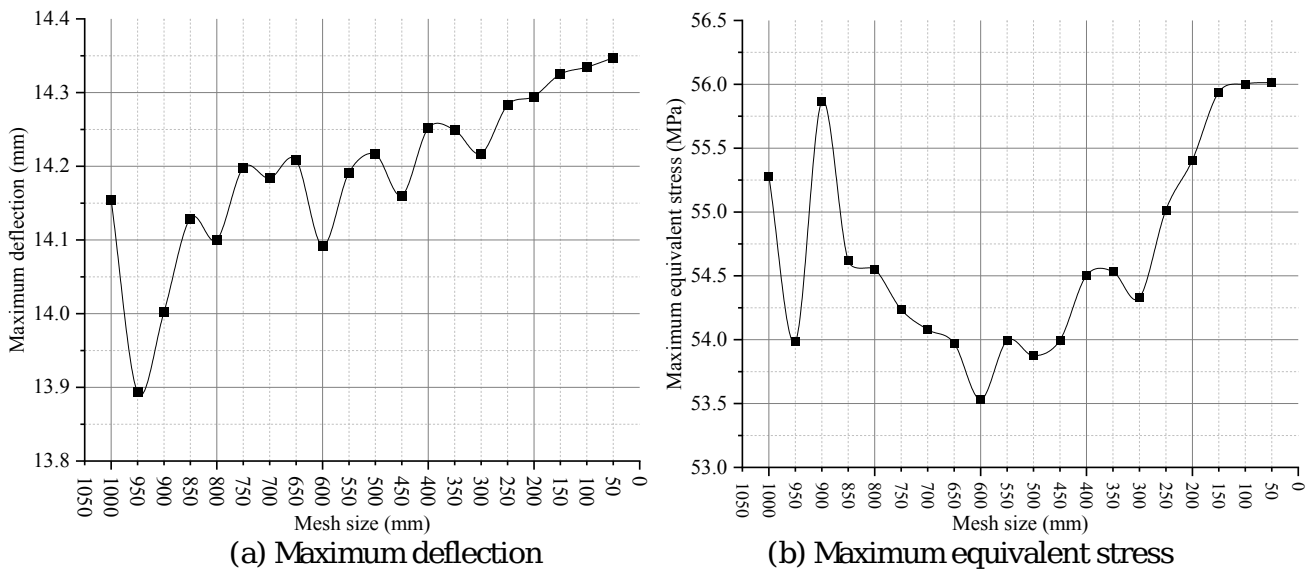
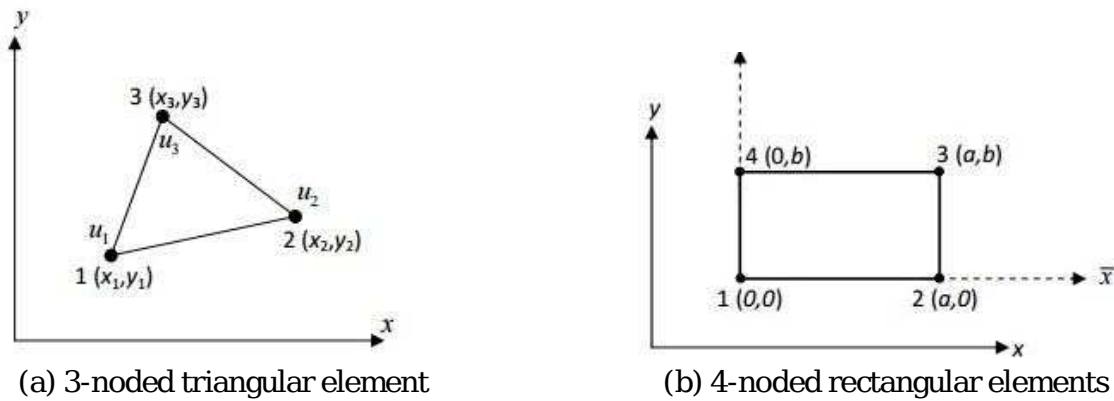


Figure 6. Convergence study



(a) 3-noded triangular element (source: [https://www.brainkart.com/article/2,3-Noded-Linear-Triangular-Element\\_5951/#google\\_vignette](https://www.brainkart.com/article/2,3-Noded-Linear-Triangular-Element_5951/#google_vignette))

(b) 4-noded rectangular elements

Table 1. Properties of steel and polyurethane

Material	Steel	Polyurethane
Density ( $\text{kg/m}^3$ )	7850	1150
Yield strength (MPa)	335	0.1 – 0.8 (approx.)
Poisson's ratio	0.3	0.46
Elastic modulus (MPa)	$2 \times 10^5$	800

The study starts with the selection of load case for the analysis which is further used to analyse deflection and stresses. The anatomies of the steel and sandwiched bridge deck are shown in Figure 8.

### Selection of load case

In this section, the different live loads available in the Indian Codal provisions are applied on the deck to select the load that will provide the maximum effect on the deck. Different live loads specified in IRC:6-2017 are considered on the decks, which are class 70R wheeled load 'L' type, class 70R wheeled load 'M' type, class 70R wheeled load 'N' type, class 70R tracked load, class A load, class B load, class AA wheeled load, and class AA tracked load. Further, the steel bridge

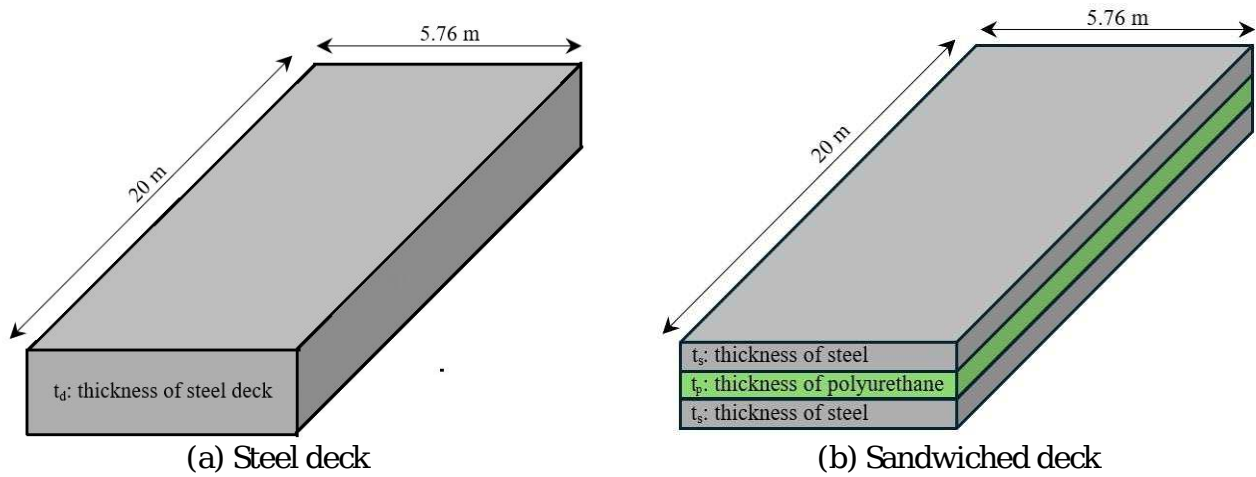


Figure 8. Steel deck anatomy and Sandwiched deck anatomy

deck of length 20 m, width 5.76 m, and 150 mm thick is considered and, analyzed for different live loads mentioned above. The deck is simply supported on all four edges. The results of maximum deflection and stresses are shown in Figure 9. It is clearly observed from the figures that 70R wheeled load ‘N’ type is giving the maximum effect of deflection and stresses. So, the same load will be considered for further analyses and depicted in Figure 10 for a better understanding.

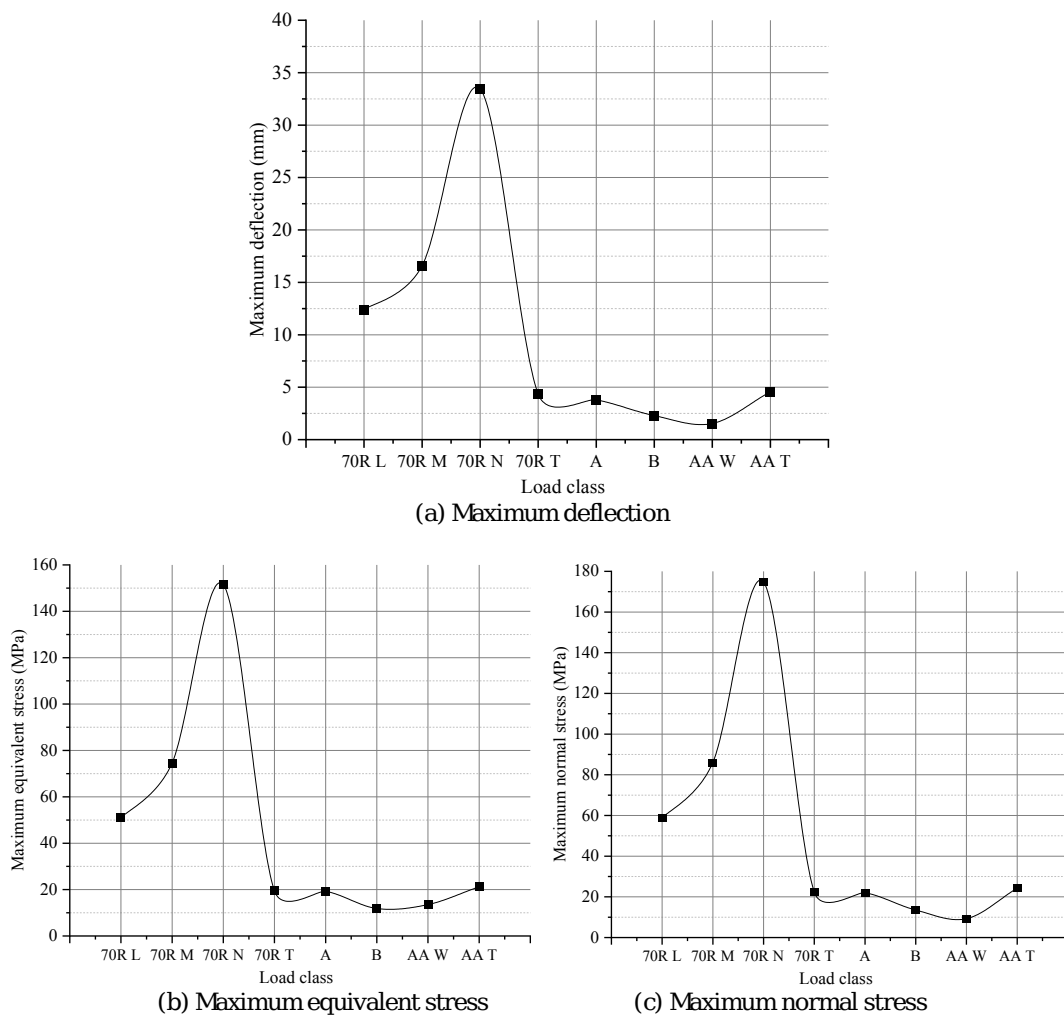


Figure 9. Results on steel deck for different live load cases (IRC:6-2017)

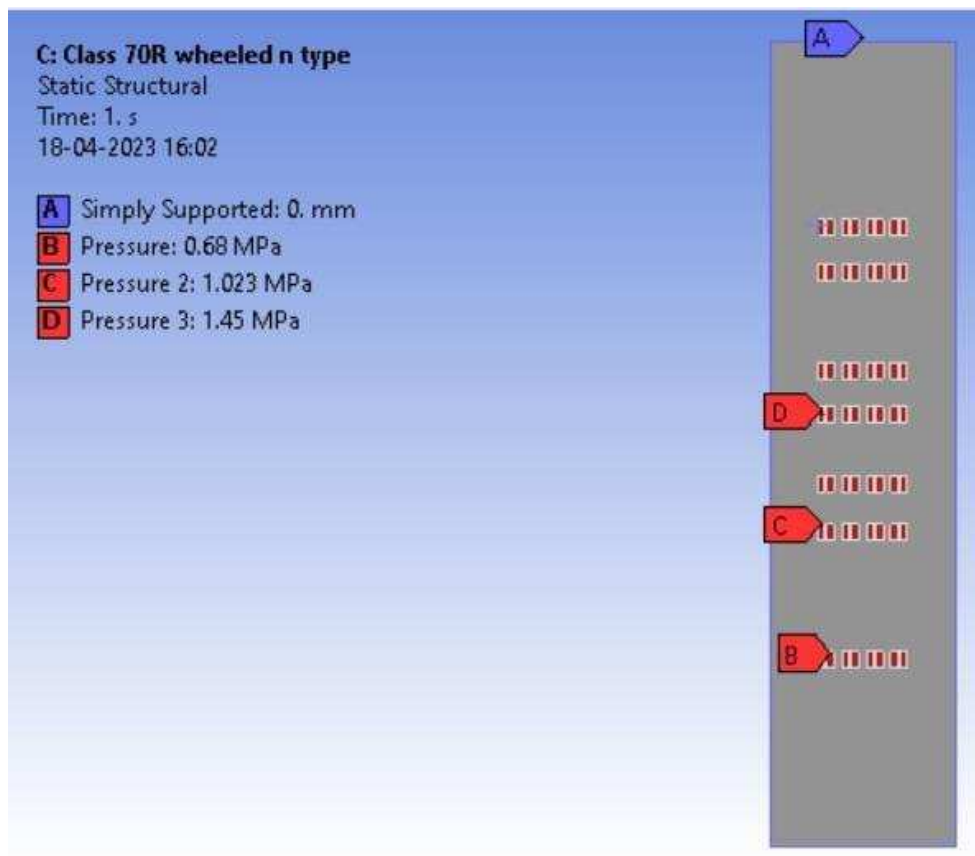


Figure 10. 70R wheeled load 'N' type

### Effect of skew angle on isotropic bridge deck

In this section, the isotropic steel deck is analysed to determine maximum deflection and stresses by varying thickness and skewness. The thickness of the deck is varied from 150 mm to 200 mm, with a 10 mm difference and the skewness from  $0^\circ$  to  $60^\circ$  to find one of the most optimum thicknesses. The thicknesses must be chosen based on the maximum deflection criteria of  $L/800$  (where  $L$  is span) specified in IRC:112-2011, clause 12.4.1 [46] and AASHTO LRFD Bridge Design Specifications 8th edition (2017), clause 2.5.2.6.2 [47]. The results are presented in Figure 11 for deflection and stresses. The variation in maximum equivalent stress and maximum normal stress along Y-axis is quite large for variation in skew angles. They become almost double from  $0^\circ$  to  $60^\circ$ . As obtained in the results, when the thickness of the deck is more than 170 mm, the maximum deflection criteria are fulfilled. So, the 200 mm thickness, i.e., a rounded value is considered for further analyses of steel decks.

### Effect of thickness on sandwiched bridge deck

Now, the sandwiched decks are modelled using steel and polyurethane by varying the thickness of steel and polyurethane. The sandwiched decks are analysed for maximum deflection and maximum stress. The sandwiched decks comprise steel plates above and below of a polyurethane layer. For the sake of simplicity, both layers of steel are taken equal in thickness. The sandwiched deck combinations are first made by reducing the amount of steel and increasing the amount of polyurethane while keeping the total thickness of the deck constant. Further, the amount of steel is kept constant while increasing the amount of polyurethane, which increases the total thickness of the deck. The annotation of the sandwiched cases is tabulated in Table 2 stated in Appendix.

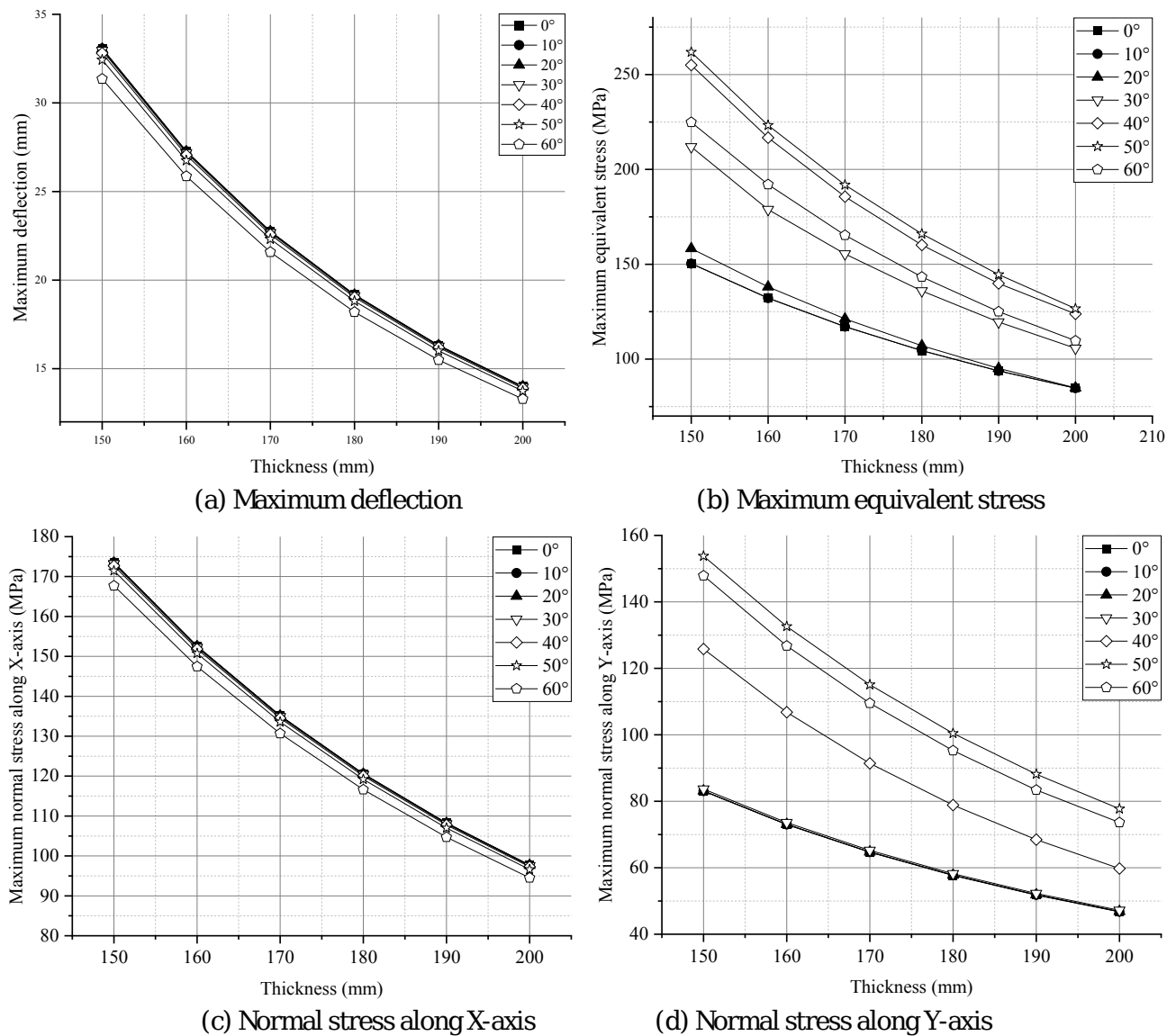


Figure 11. Variation of maximum values of deflection and stresses

Figure 12 shows the results of the analysis. As expected, the value of maximum deflection and stresses increase as we go on decreasing the amount of steel and adding the same amount of polyurethane. But, if we keep on increasing the polyurethane on keeping the steel constant, we see a decrease in those parameters but the total thickness of the deck increases. Also, some combinations, allow for low stresses and deflection but the amount of steel required for those is still higher than the increased thickness ones. Among the presented sandwiched deck combinations, a few are selected for the analysis by varying the skew angles, as per the pattern shown in Figure 13.

### Effect of skewness on sandwiched deck

In this section, sandwiched decks are analysed by varying the skew angles. The combinations are selected based on the sustainability and RRR concept of waste management. The decks are selected to show the effect of decreasing the amount of steel while simultaneously increasing amount of polyurethane, while keeping the total thickness constant on the behaviour of the deck. Also, two more combinations are selected, one of which has the lowest deflection and stresses, and the other is one of the best combinations of steel and polyurethane sandwiched deck for 200 mm thickness (which will be used in the subsequent sections for comparison with steel isotropic

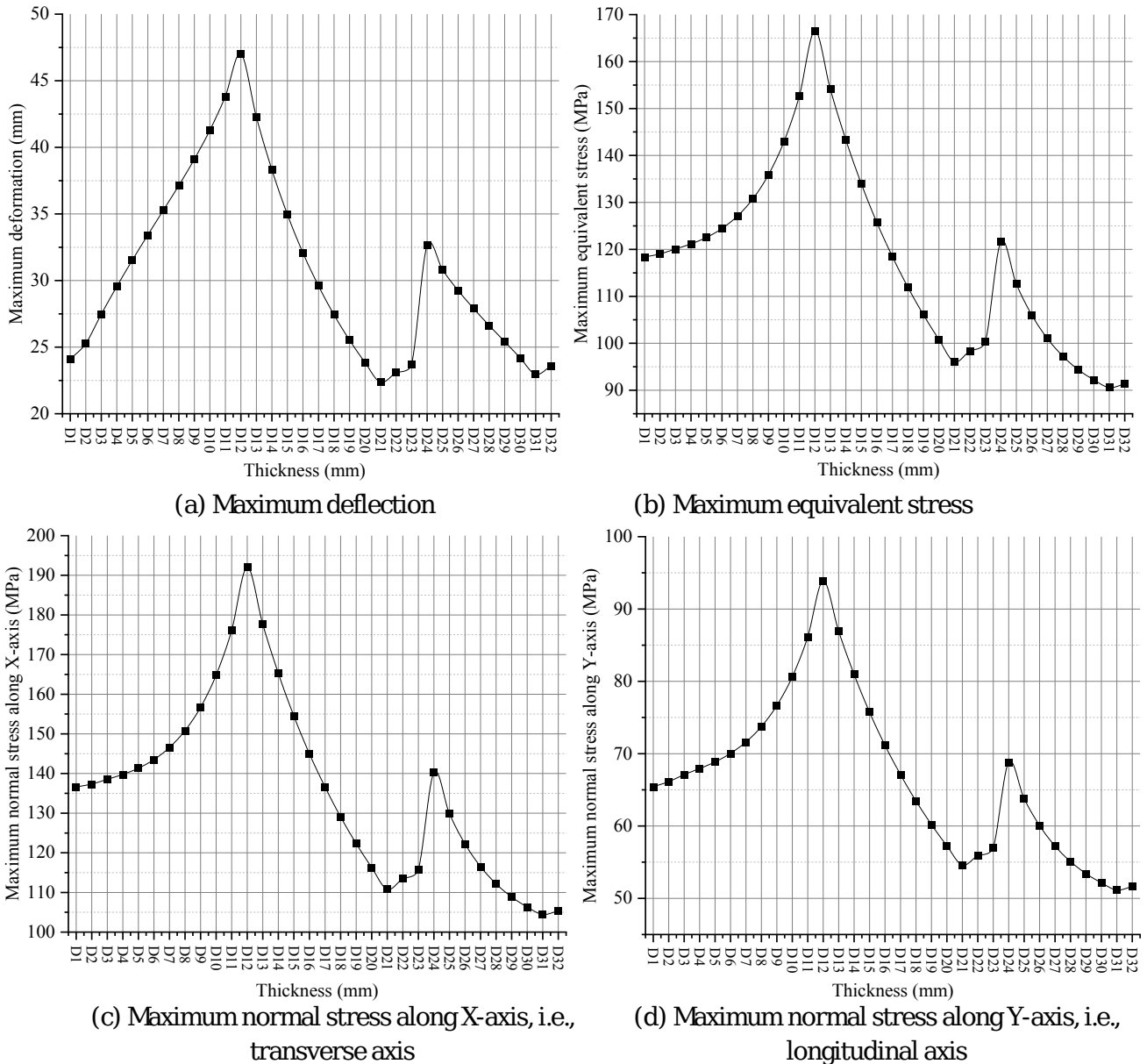


Figure 12. Results of different sandwiched decks

deck of 200 mm thickness). The combinations are selected from Table 2, D1 to D12, D20, D21 and D31 and taken for this analysis. The results of deflection and stresses are shown in Figure 14. The deflection and stresses are relatively comparable on increasing the skew angle. However, as the trend suggests, on increasing the skew angle, the deflection and stresses decrease slightly, and may be considered while designing sandwiched decks.

### Comparison between steel and sandwiched decks

In this section, the steel deck of thickness 200 mm is compared with two sandwiched deck combinations (D31 and D21), which are as follows:

- $t_s = 70$  mm,  $t_p = 60$  mm,
- $t_s = 30$  mm,  $t_p = 200$  mm.

The combination D31 leads to a total thickness of 200 mm and has low values of deflection and stresses. The combination D21 has values even lesser compared to D31 but it has more thickness compared to the former. D21 has a total thickness of 260 mm but only 60 mm of steel, on the

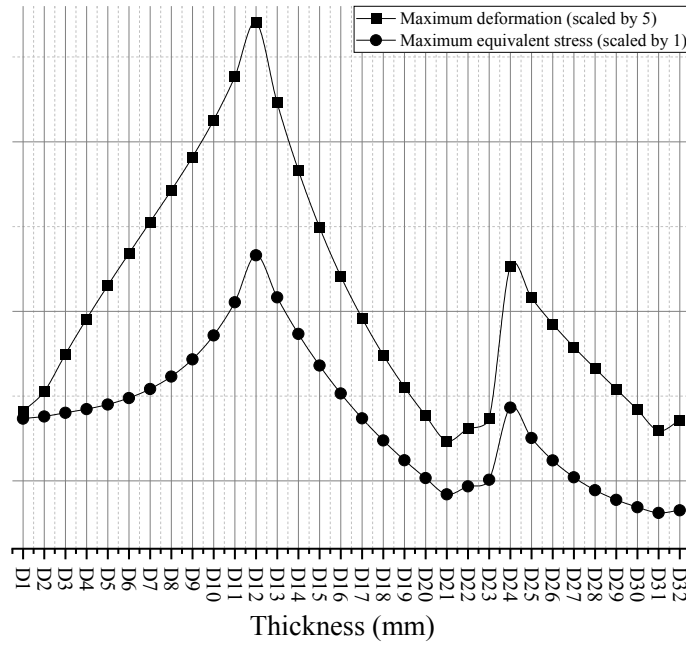


Figure 13. Trend line for the sandwiched decks maximum deflection (scaled by 5)

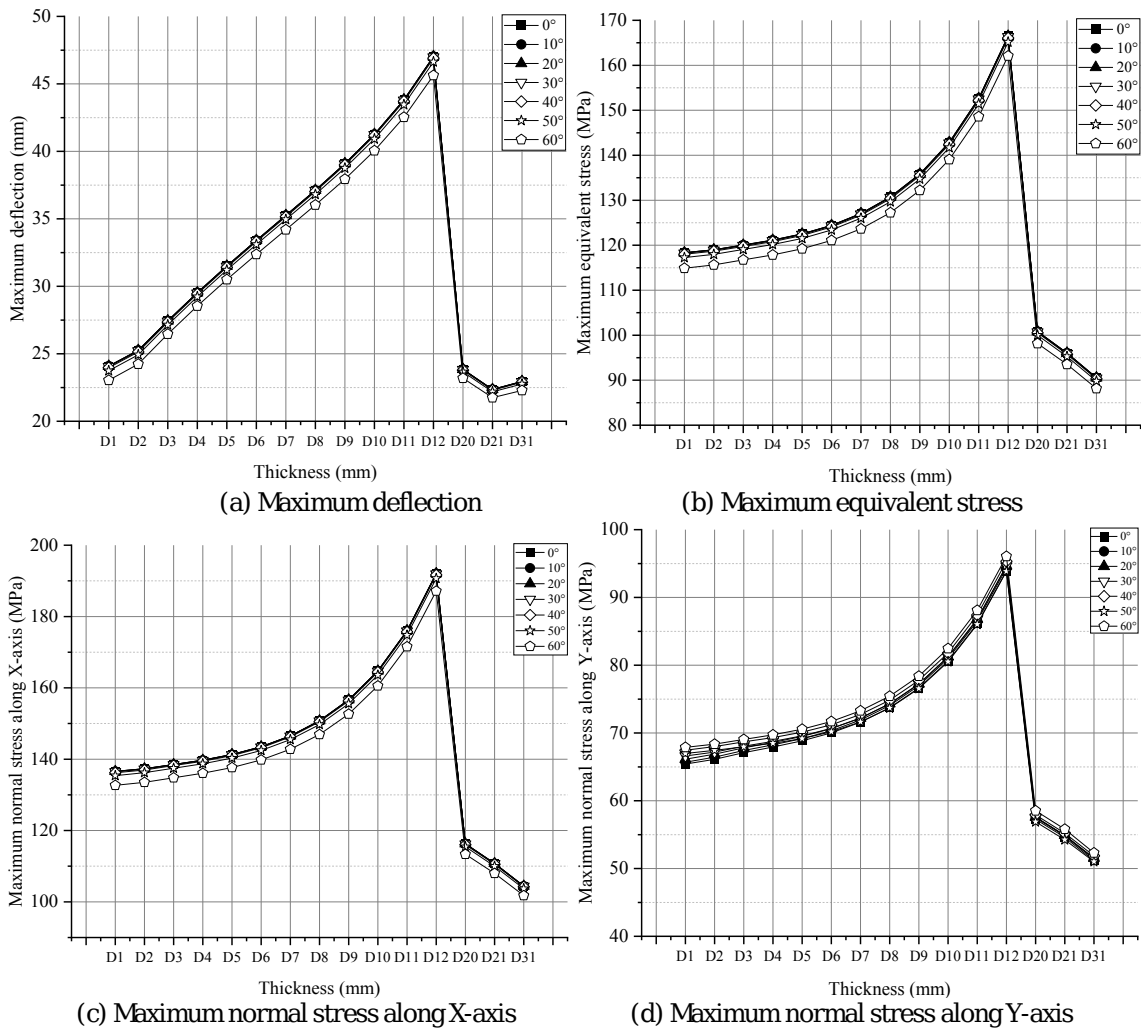


Figure 14. Variation of results of sandwiched decks for different skew angles

other hand, D31 has 140 mm of steel. The results of maximum deflection, maximum equivalent stress, maximum normal stress along X-axis, i.e., the transverse axis, and maximum normal stress along Y-axis, i.e., the longitudinal axis are compared. The findings are presented in Figure 15. It is observed that the three decks have comparable deflections and stresses. Interestingly the maximum equivalent stress of steel isotropic deck turns sharply greater than the sandwiched combinations after skew angle  $20^\circ$ , also the maximum normal stress along Y-axis, i.e., longitudinal axis of steel isotropic deck becomes greater than the sandwiched combination after  $30^\circ$ . However, the maximum deflection of steel isotropic deck remains significantly less than the sandwiched combinations, viz., about 8 mm less for both combinations 1 and 2. For the clarity of the readers, some results are depicted in the form of contours and shown in Figure 16, Figure 17, and Figure 18, for  $0^\circ$  skewed deck,  $30^\circ$  skewed deck, and  $60^\circ$  skewed deck, respectively.

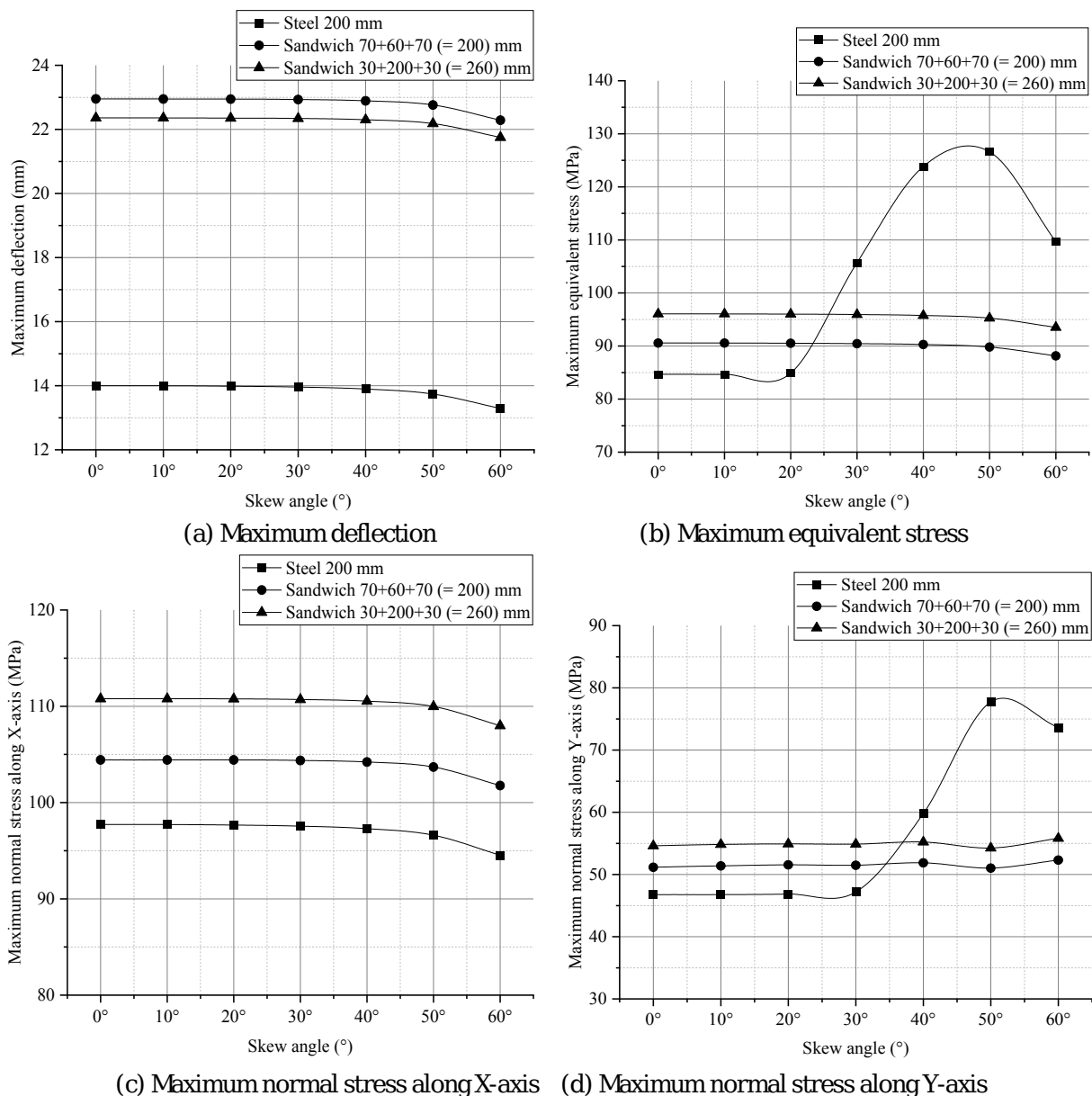


Figure 15. Results of isotropic and sandwiched decks

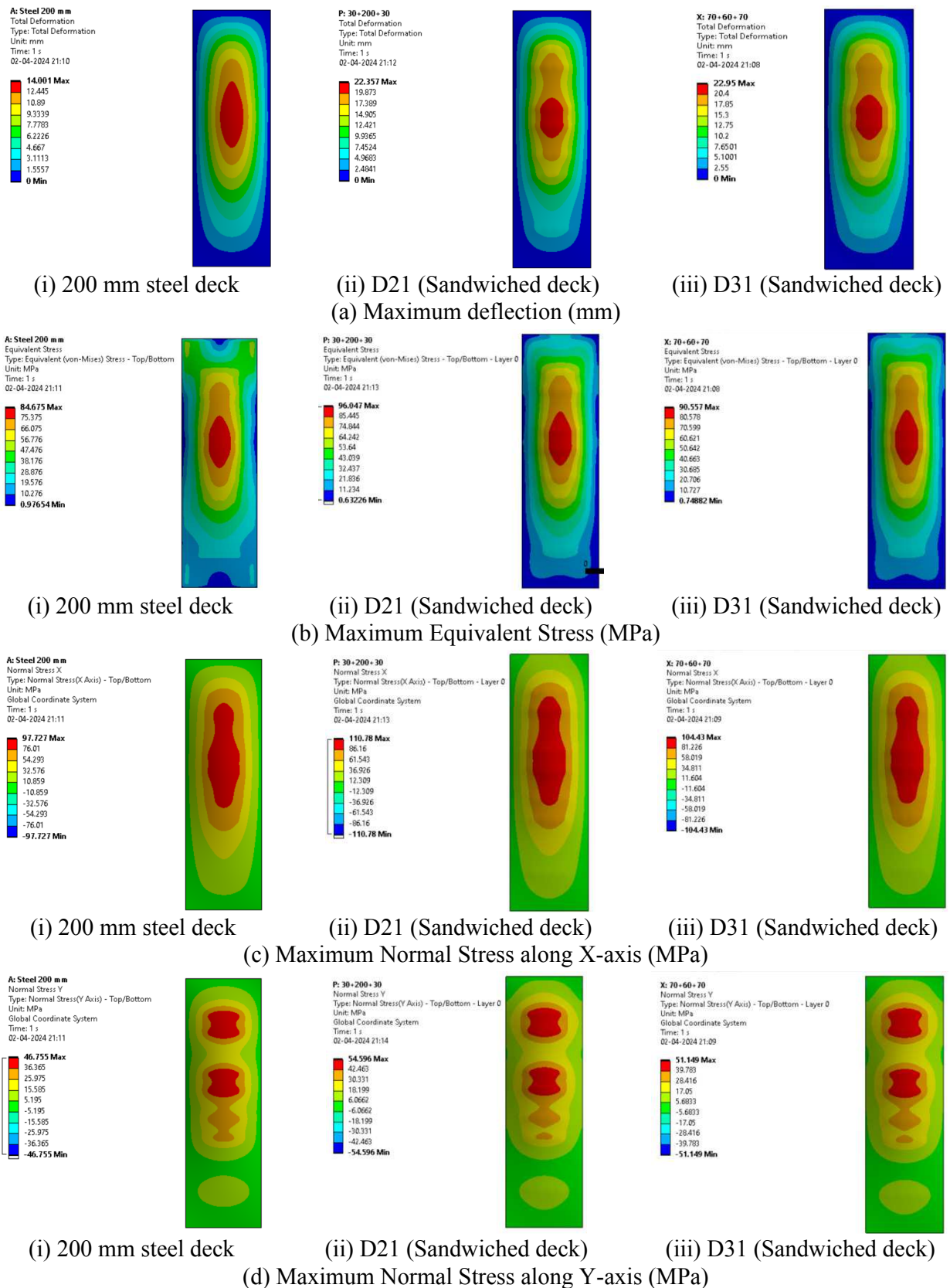


Figure 16. Variation of deflection and stresses on 0° skewed deck

### A special case: polyurethane

A special case is considered in this section where only polyurethane is used. A bridge of similar dimensions, i.e., length 20 m, and width 5.76 m, is used for this analysis. The thickness of the deck

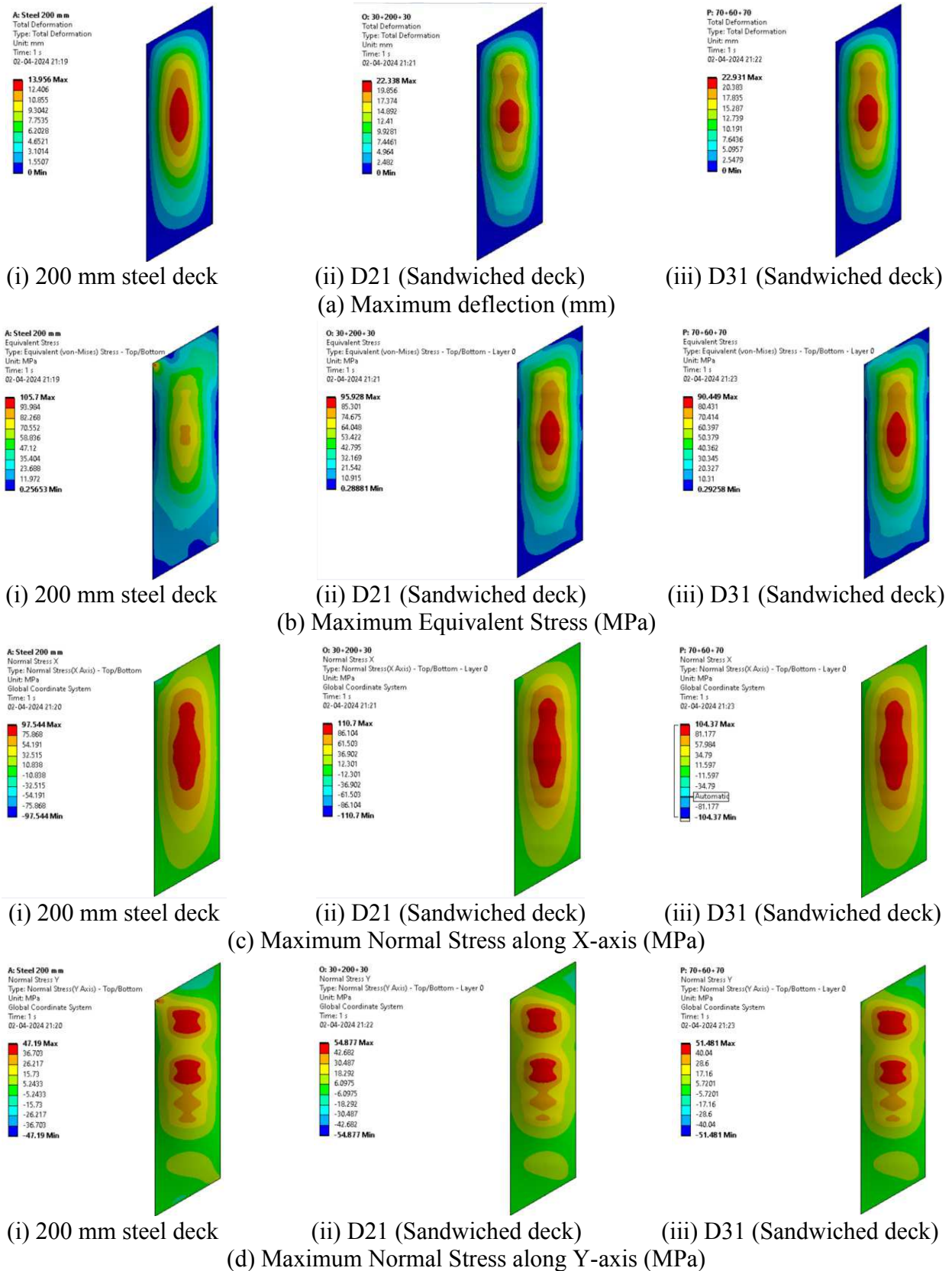


Figure 17. Variation of deflection and stresses on 30° skewed deck

is increased from 250 mm to 1500 mm along with the change in skew angle, to understand the response of the deck to the applied load. The results are presented as shown in Figure 19. As the result suggests, the stresses and the maximum deflection decrease substantially as thickness

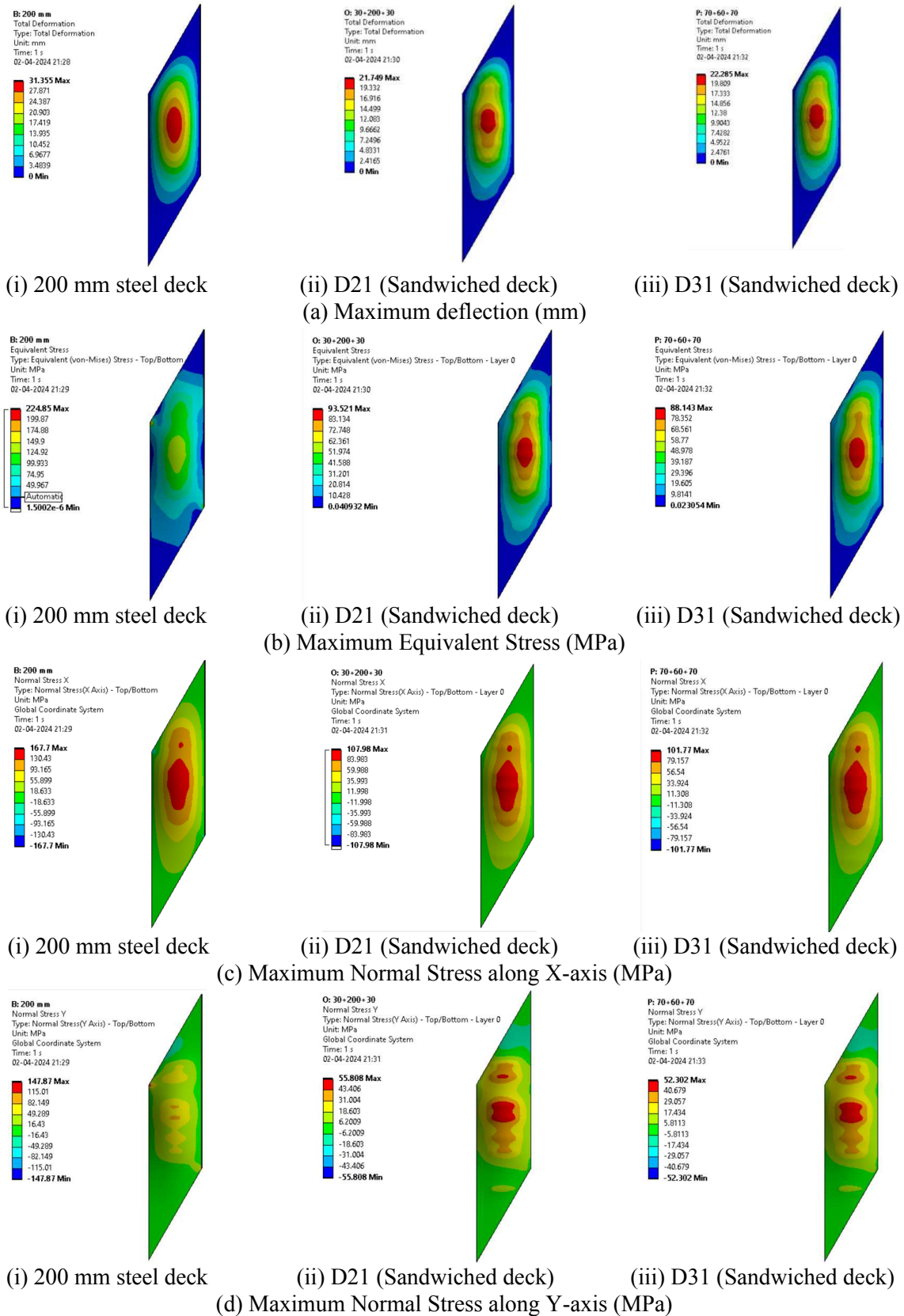


Figure 18. Variation of deflection and stresses on 60° skewed deck

increases. The percentage decrease in the maximum deflection from 250 mm to 500 mm is of 677% and from 250 mm to 1500 mm is of 772%. The percentage decrease in the stresses from 250 mm to 500 mm is of 298% and from 250 mm to 1500 mm is of 387%. The variation with the skew

angle, however, is very small, almost insignificant. Hence, if the design constraints permit, only polyurethane bridge deck can be a good alternative for steel, or even sandwiched deck. Also, it can be used for pedestrian bridges and many other such small-scale applications, or footpaths, or roads as a cover of potholes, etc.

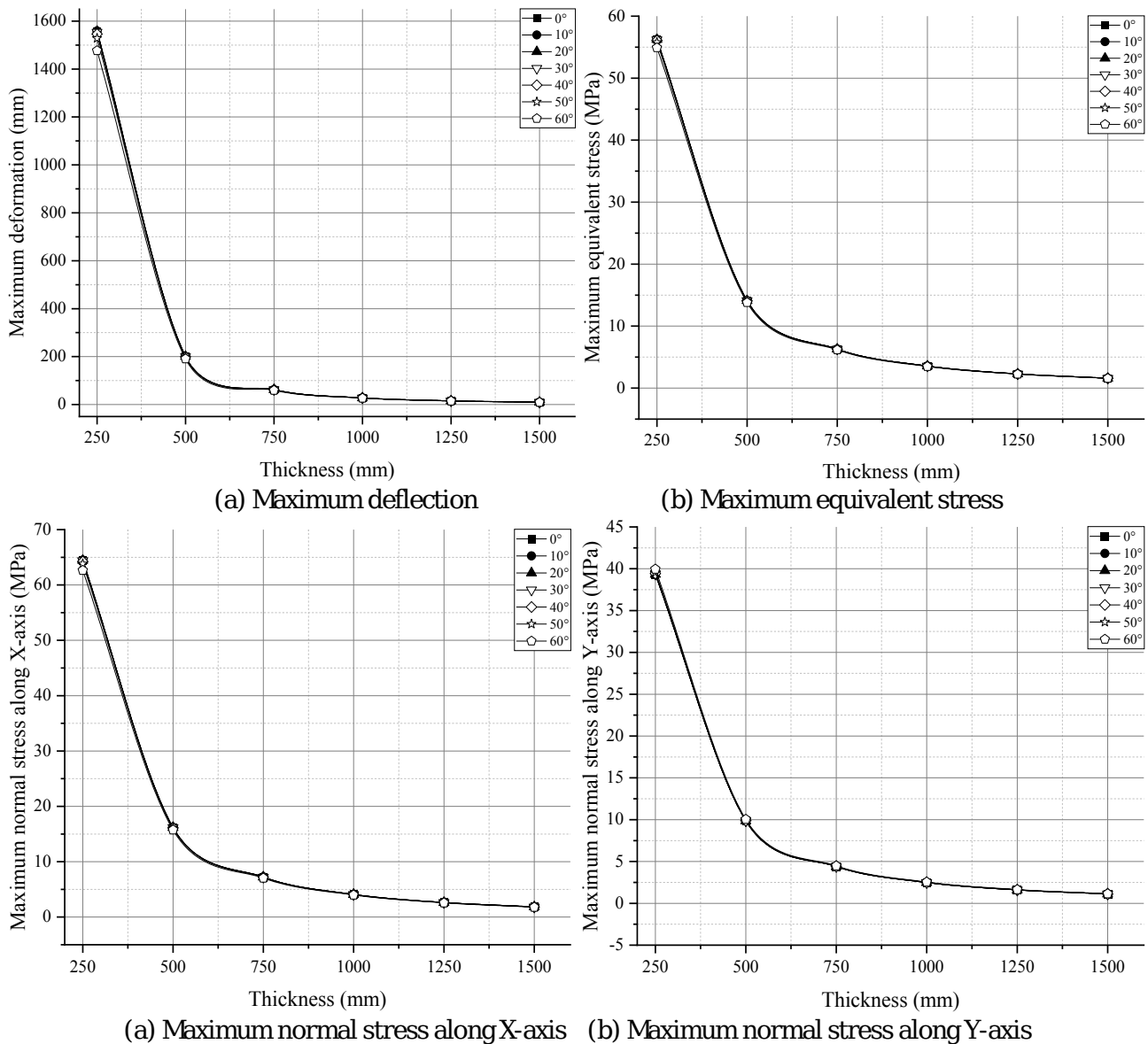


Figure 19. Results of bridge deck modelled using polyurethane

## 5 Conclusion

The sandwiched decks are analysed in the present study along with isotropic steel decks and make a comparative study as well. The following conclusions may be drawn from the study and are as follows:

- For a span of deck that can include all the loads completely (for one cycle), 70R wheeled load 'N' type gives the largest deflection and stresses among the live loads listed in IRC:6-2017.
- For a deck length of 20 m of steel, thickness over 170 mm is suitable as per the  $L/800$  deflection criteria.
- For a steel deck, on increasing the skew angle, the deflection decreases slightly, and the equiv-

alent stress decreases for 10° skew angle and then increases significantly. The normal stress along transverse direction decreases slightly and along the longitudinal direction increases significantly.

- On increasing the polyurethane thickness and reducing the steel thickness (to keep total thickness constant), led to an increase in deflection and stresses. Though on increasing the total thickness by increasing the polyurethane amount, deflection and stresses have decreased.
- On increasing the skew angle for the sandwiched deck, the deflection and stresses are decreased; so, the skewed deck is more effective than the straight bridge deck.
- The deflection in one of the most optimum sandwiched combinations (in this study) is 9 mm more than the steel counterpart. The stresses however increase by only 4-7 MPa.
- Only polyurethane deck of 1250 mm is the functional equivalent of steel deck of 200 mm. However, the stresses in the former are significantly lesser than the later. The equivalent stress being almost 37 times less.

### Future scope

The future studies, suggestions and academic opportunities are summarised as follows:

- The analysis may be extended for dynamic loading conditions such as traffic-induced vibrations, wind loads, and seismic events.
- Soil structure interaction can be modelled and studied to predict the behaviour of soil and its interaction with the structure.
- Detailed multi-scale modelling may be developed to facilitate global structural predictions.
- Field testing and long-term monitoring may be conducted to provide feedback for further improvement.
- The impact on the environment may be ascertained after the long-term monitoring, which would also predict the sustainability and adaptability of such structures.

The above points may also be considered for academic projects to be conducted in laboratories on the prototype to predict the behaviour of such structures.

### Appendix

**Table 2.** Combinations used for sandwiched deck analysis

Annotation	Steel layers thickness, $t_s$ (mm)	Polyurethane layer thickness, $t_p$ (mm)
D1	82.5	5
D2	80	10
D3	75	20
D4	70	30
D5	65	40
D6	60	50
D7	55	60
D8	50	70
D9	45	80
D10	40	90
D11	35	100
D12	30	110
D13	30	120
D14	30	130
D15	30	140

**Table 2.** Combinations used for sandwiched deck analysis - continued

Annotation	Steel layers thickness, $t_s$ (mm)	Polyurethane layer thickness, $t_p$ (mm)
D16	30	150
D17	30	160
D18	30	170
D19	30	180
D20	30	190
D21	30	200
D22	30	195
D23	30	191
D24	35	130
D25	40	120
D26	45	110
D27	50	100
D28	55	90
D29	60	80
D30	65	70
D31	70	60
D32	67.5	65

## Declarations

### Use of AI tools

The authors declare that they have not used Artificial Intelligence (AI) tools in the creation of this article.

### Data availability statement

No Data associated with the manuscript.

### Ethical approval (optional)

The authors state that this research complies with ethical standards. This research does not involve either human participants or animals.

### Consent for publication

Not applicable

### Conflicts of interest

The authors declare that they have no conflict of interest.

### Funding

No funding was received for this research.

### Author's contributions

A.A.: Methodology, Software, Validation, Writing - Review & Editing, Visualization. D.K.S.: Validation, Formal Analysis, Supervision, Writing - Original Draft, Writing - Review & Editing, Visualization. P.A.: Supervision, Writing - Review & Editing, Visualization. All authors discussed

the results and contributed to the final manuscript.

## Acknowledgements

All authors want to show thankfulness to each contribution for accomplishing this research work.

## References

- [1] Ahmed, A.T.M.R. and Anam, I. Dynamic analysis of RC bridges. In *Proceedings, 2nd International Conference on Structural Engineering, Mechanics & Computation (ICSEMC)*, pp. 1-6, Cape Town, South Africa, (2003, September).
- [2] Da Silva, J.G.S. Dynamical performance of highway bridge decks with irregular pavement surface. *Computers & Structures*, 82(11-12), 871–881, (2004). [[CrossRef](#)]
- [3] Mahmood, M.N. and Al-Ghabsha, A.T.S. Dynamic analysis of bridges subjected to moving vehicles. *Al-Rafidain Engineering*, 14(4), 34-50, (2006).
- [4] Yarnold, M.T., Wilson, J.L., Jen, W.C. and Yen, B.T. Local buckling analysis of trapezoidal rib orthotropic bridge deck systems. *Bridge Structures*, 3(2), 93–103, (2007). [[CrossRef](#)]
- [5] Menassa, C., Mabsout, M., Tarhini, K. and Frederick, G. Influence of skew angle on reinforced concrete slab bridges. *Journal of Bridge Engineering*, 12(2), 205-214, (2007). [[CrossRef](#)]
- [6] Li, Y.S., Tian, Y. and Zhang, Y.L. Local stress analysis of orthotropic steel bridge decks in high-speed railway. *Advanced Material Research*, 243(249), 1659-1663, (2011). [[CrossRef](#)]
- [7] Kar, A., Khatri, V., Maiti, P.R. and Singh, P.K. Study on effect of skew angle in skew bridges. *International Journal of Engineering Research and Development*, 2(12), 13-18, (2012).
- [8] De Freitas, S.T., Kolstein, H. and Bijlaard, F. Fatigue behavior of bonded and sandwich systems for strengthening orthotropic bridge decks. *Composite Structures*, 97, 117–128, (2013). [[CrossRef](#)]
- [9] Sindhu, B.V., Ashwin, K.N., Dattatreya, J.K. and Dinesh, S.V. Effect of skew angle on static behaviour of reinforced concrete slab bridge decks. *International Journal of Research in Engineering and Technology*, Conference Issue, 50-58, (2013).
- [10] Hassel, H.L., Bennett, C.R., Matamoros, A.B. and Rolfe, S.T. Parametric analysis of cross-frame layout on distortion-induced fatigue in skewed steel bridges. *Journal of Bridge Engineering*, 18(7), 601-611, (2013). [[CrossRef](#)]
- [11] Singh, D.K., Duggal, S.K. and Pal, P. Analysis of stiffened plates using FEM—a parametric study. *International Research Journal of Engineering and Technology*, 2(4), 1650-1656, (2015).
- [12] Pipinato, A. and De Miranda, M. Steel and composite bridges (Chapter 10). In *Innovative Bridge Design Handbook (Construction, Rehabilitation and Maintenance)* (pp. 247-271). United Kingdom: Butterworth-Heinemann Inc, (2016).
- [13] Li, Y., Cai, C.S., Liu, Y., Chen, Y. and Liu J. Dynamic analysis of a large span specially shaped hybrid girder bridge with concrete-filled steel tube arches. *Engineering Structures*, 106, 243-260, (2016). [[CrossRef](#)]
- [14] Shan, C. and Yi, Y. Stress concentration analysis of an orthotropic sandwich bridge deck under wheel loading. *Journal of Constructional Steel Research*, 122, 488–494, (2016). [[CrossRef](#)]
- [15] Bebiano, R., Calçada, R., Camotima, D. and Silvestre, N. Dynamic analysis of high-speed railway bridge decks using generalised beam theory. *Thin-Walled Structures*, 114, 22-31, (2017). [[CrossRef](#)]

- [16] Jiang, X., Su, Q., Han, X., Shao, C. and Chen, L. Experimental study and numerical analysis on mechanical behavior of T-shape stiffened orthotropic steel-concrete composite bridge decks. *International Journal of Steel Structures*, 17, 893-907, (2017). [[CrossRef](#)]
- [17] Singh, D.K., Duggal, S.K. and Pal, P. Free vibration analysis of stiffened lock gate structure coupled with fluid. *Journal of Structural Engineering*, 45(1), 1-9, (2018).
- [18] Singh, D.K., Pal, P. and Duggal, S.K. Dynamic pressure on lock gate structure coupled with fluid. *Vibroengineering Procedia*, 29, 165-170, (2019). [[CrossRef](#)]
- [19] Sundria, R. and Tripathi, R.K. Effect of skewness on reinforced concrete slab bridge by finite element method. *International Journal of Bridge Engineering*, 7(1), 33-40, (2019).
- [20] Chen, S., Huang, Y., Gu, P. and Wang, J.Y. Experimental study on fatigue performance of UHPC-orthotropic steel composite deck. *Thin-Walled Structures*, 142, 1-18, (2019). [[CrossRef](#)]
- [21] Singh, D.K., Pal, P. and Duggal, S.K. Free vibration analysis of lock gate structure. *Journal of Mechanics*, 36(4), 507-520, (2020). [[CrossRef](#)]
- [22] Agarwal, P. and Singh, D.K. Finite Element Analysis on Skew Box-Girder Bridges. In Proceedings, *International Conference on Trends and Recent Advances in Civil Engineering*, pp. 15-26, Singapore: Springer Nature Singapore. (2022, August). [[CrossRef](#)]
- [23] Jain, N. and Singh, V.K. Dynamic analysis of reinforced concrete bridges under seismic excitation. *Journal of Civil Engineering and Environmental Technology*, 7(2), 179-184, (2020).
- [24] Huang, W., Pei, M., Liu, X., Yan, C. and Wei, Y. Nonlinear optimization of orthotropic steel deck system based on response surface methodology. *AAAS Research*, 2020, 1-22, (2020). [[CrossRef](#)]
- [25] Diaz Arancibia, M., Rugar, L. and Okumus, P. Role of skew on bridge performance. *Transportation Research Record*, 2674(5), 282-292, (2020). [[CrossRef](#)]
- [26] Gautam, K. and Shrivastava, S. Skew bridge analysis using "ANSYS". *International Journal of Engineering Research & Technology*, 9(06), 870-875, (2020).
- [27] Madenci, E., Özkılıç, Y.O. and Gemi, L. Experimental and theoretical investigation on flexure performance of pultruded GFRP composite beams with damage analyses. *Composite Structures*, 242, 112162, (2020). [[CrossRef](#)]
- [28] Madenci, E., Özkılıç, Y.O. and Gemi, L. Theoretical investigation on static analysis of pultruded GFRP composite beams. *Academic Platform Journal of Engineering and Science*, 8(3), 483-490, (2020). [[CrossRef](#)]
- [29] Özkılıç, Y.O., Yazman, Ş., Aksoylu, C., Arslan, M.H. and Gemi, L. Numerical investigation of the parameters influencing the behavior of dapped end prefabricated concrete purlins with and without CFRP strengthening. *Construction and Building Materials*, 275, 122173, (2021). [[CrossRef](#)]
- [30] Gupta, K.K. Stress assessment of skew composite steel I-girder bridge. *International Journal of Engineering Research & Technology*, 10(05), 500-508, (2021).
- [31] Agarwal, P., Pal, P. and Mehta, P.K. Analysis of isotropic and orthotropic sandwich bridge decks. In Proceedings, *Recent Trends in Civil Engineering, Lecture Notes in Civil Engineering (ICRTICE)*, pp. 109-120, Singapore, (2021). [[CrossRef](#)]
- [32] Sahoo, P.R. and Barik, M. Dynamic response of stiffened bridge decks subjected to moving loads. *Journal of Vibration Engineering & Technologies*, 9, 1983-1999, (2021). [[CrossRef](#)]
- [33] Singh, D.K. and Pal, P. Forced vibration analysis of stiffened lock gate structure. *Journal of*

*Sound and Vibration*, 510, 116278, (2021). [[CrossRef](#)]

- [34] Doğan, M.A., Yazman, Ş., Gemi, L., Yildiz, M. and Yapici, A. A review on drilling of FML stacks with conventional and unconventional processing methods under different conditions. *Composite Structures*, 297, 115913, (2022). [[CrossRef](#)]
- [35] Gemi, L., Madenci, E., Özkılıç, Y.O., Yazman, Ş. and Safonov, A. Effect of fiber wrapping on bending behavior of reinforced concrete filled pultruded GFRP composite hybrid beams. *Polymers*, 14(18), 3740, (2022). [[CrossRef](#)]
- [36] Li, Z., Zhang, J., Zhu, Y. and Tu, J. Dynamic property analysis of orthotropic bridge deck with local fatigue crack. *Advances in Civil Engineering*, 2022, 3787756, (2022). [[CrossRef](#)]
- [37] Kanwar, C.S. and Khan, M.Z. Review on analysis of four-lane bridge deck under different loading condition. *International Journal of Creative Research Thoughts*, 10(6), 945-950, (2022).
- [38] Agarwal, P., Pal, P. and Mehta, P.K. Free vibration analysis of RC box-girder bridges using FEM. *Sound & Vibration*, 56(2), 105-125, (2022). [[CrossRef](#)]
- [39] Singh, D.K., Pal, P. and Duggal, S.K. Free vibration analysis of stiffened lock gate structure. *Journal of Vibration Engineering & Technologies*, 10, 1779–1791, (2022). [[CrossRef](#)]
- [40] Liu, P., Chen, Y., Lu, H., Zhao, J., An, L. and Wang, Y. Fatigue resistance analysis of the orthotropic steel deck with arc-shaped stiffener. *Metals*, 12(10), 1739, (2022). [[CrossRef](#)]
- [41] Singh, D.K. and Agarwal, P. Analysis of steel-concrete-steel sandwich plate structure. *Materials Today: Proceedings*, 58(3), 846-849, (2022). [[CrossRef](#)]
- [42] Agarwal, P. and Singh, D.K. Parametric study on prestressed skewed box-girder bridge. *Advances in Bridge Engineering*, 4, 12, (2023). [[CrossRef](#)]
- [43] Singh, D.K. and Agarwal, P. Analysis of isotropic stiffened plate structure. *Noise & Vibration Worldwide*, 54(10-11), 557-569, (2023). [[CrossRef](#)]
- [44] Singh, D.K., Pal, P. and Duggal, S.K. Forced vibration characteristics of lock gate structure. *Noise & Vibration Worldwide*, 54(2-3), 134-144, (2023). [[CrossRef](#)]
- [45] IRC: 6 *Standard Specifications and Code of Practice for Road Bridges*, Section: II Loads and Load combinations (Seventh Revision), New Delhi, India, (2017).
- [46] IRC: 112 *Standard Specifications and Code of Practice for Road Bridges*, Section: II Loads and Load combinations (Seventh Revision), New Delhi, India, (2017).
- [47] AASHTO: *LRFD Bridge Design Specifications*, 8th Edition, American Association of State Highway and Transportation Officials, Washington DC, (2017).

Mathematical Modelling and Numerical Simulation with Applications (MMNSA)

(<https://dergipark.org.tr/en/pub/mmnsa>)



**Copyright:** © 2024 by the authors. This work is licensed under a Creative Commons Attribution 4.0 (CC BY) International License. The authors retain ownership of the copyright for their article, but they allow anyone to download, reuse, reprint, modify, distribute, and/or copy articles in MMNSA, so long as the original authors and source are credited. To see the complete license contents, please visit (<http://creativecommons.org/licenses/by/4.0/>).

**How to cite this article:** Anand, A., Singh, D.K. & Agarwal, P. (2024). Finite element static analysis of polyurethane-sandwiched skewed bridge decks. *Mathematical Modelling and Numerical Simulation with Applications*, 4(2), 193-215. <https://doi.org/10.53391/mmnsa.1411726>



RESEARCH PAPER

## Mathematical modelling of using renewable energy in the power sectors for the sustainable environment

Md. Sirajul Islam <sup>1,‡</sup>, Mst. Shefali Khatun <sup>1,‡</sup> and Md. Haider Ali Biswas <sup>2,\*,‡</sup>

<sup>1</sup>Department of Mathematics, Bangabandhu Sheikh Mujibur Rahman Science and Technology University, Gopalganj, 8100, Bangladesh, <sup>2</sup>Mathematics Discipline, Khulna University, Khulna, 9208, Bangladesh

\* Corresponding Author

‡ sirajul.math@bsmrstu.edu.bd (Md. Sirajul Islam); shefali.16mat033@bsmrstu.edu.bd (Mst. Shefali Khatun); mhabiswas@math.ku.ac.bd (Md. Haider Ali Biswas)

### Abstract

Currently, human-caused greenhouse gas emissions are one of the main causes of global warming. Burning fossil fuels (such as coal, oil, and gas) have become a climate change due to the uptake of heat-trapping gases. A lot of CO<sub>2</sub> is produced from this, which helps in the creation of greenhouse gases. On the other hand, global electricity demand has been rising for decades, such to rising populations, increasing industrialization, and higher incomes. The power sector is the biggest source of carbon dioxide emissions because of fossil fuel, the main source of energy used for power generation all over the world that's why climate change as well as increased global warming. Therefore, most countries have set targets for the use of renewable energy (RE) to reduce their electricity and need for energy and carbon emissions. In this study, RE is used to keep the environment sustainable, where the system of ODEs has been formed using different types of parameters to analyze the mathematical structure of four variables associated with RE. Positivity test, stability analysis, and bifurcation analysis are examined to prove the truth for the sustainability of the environment. The model plays a special role in increasing electricity production and reducing greenhouse gases in the environment. This study emphasizes the significance of employing RE in the power sector for environmental sustainability.

**Keywords:** Renewable energy; environmental sustainability; bifurcation analysis; logistic model

**AMS 2020 Classification:** 34A34; 37N25; 65L05; 92D25; 92B05

### 1 Introduction

The environment is an important component of human civilization. Since the development of civilization, people have gradually developed their environment. Just as humans are exploiting

nature for their own needs or using natural resources, nature is also ready to oppose humans and the entire life force in its fragmented and wounded form. At the turn of the 21st century, when mankind is at the pinnacle of civilization, the environment is pushing us toward catastrophe. A 'greenhouse reaction' has occurred in the environment, which is changing the climate by increasing global temperatures day by day. Human activities have reached such a level that the environment can't meet the needs of billions of people. Among man-made activities, industries play a major role in the emission of various types of air pollutants into the atmosphere. With the increase in population unplanned urbanization, new industrial areas, thermal power generation vehicles, etc. have developed, where most of the electricity is used. Electric power plays an important role in people's lives because nowadays all-important activities require electricity directly or indirectly and it provides an increasing share of energy production and consumption in all countries and its growth continues for transportation and thermal electrification energy applications as well as digital connectivity devices and air conditioning. A large portion of the world's energy is used to build transport and power buildings. The use of fossil fuels is a major cause of environmental pollution and climate change. Most of the world's electricity comes from fossil fuel-based power plants. Carbon dioxide and other hothouse feasts are responsible for global warming because such fuel can provide a large amount of energy. It is widely used in everything from power generation to vehicles. Because of the high concentration of carbon in these fuels, the use of these fuels releases a large amount of carbon into the atmosphere, contributing to the production of various greenhouse gases, including carbon dioxide, carbon monoxide, and methane. This command to global warming and climate change.

The Paris Climate Agreement, adopted in 2015, is a landmark international treaty aiming to limit global warming to below 2 degrees Celsius, preferably to 1.5 degrees Celsius, compared to pre-industrial levels. The agreement requires all signatories to submit Nationally Determined Contributions (NDCs) that outline their plans to reduce greenhouse gas emissions and adapt to climate impacts [1]. Among the latest developments from the COP meeting COP26 (2021) - pledging to phase out unabated coal power and end international financing for coal in Glasgow, more than 100 countries committing to reduce methane emissions by 30% by 2030, agreement to increase financial support to help developing countries adapt to climate impacts and transition to renewable energy, and comprehensive review of collective progress towards the goals of the Paris Agreement at COP28 (2023) - Dubai, highlighting the urgent need for accelerated action, many countries submitting more ambitious NDCs, pledging to cut deep emissions and increase investment in renewable energy, significant discussions were held on the role of green hydrogen as a key component of decarbonization efforts. The latest regulation on renewable energy and sustainability is a package of policies in the European Union that aims to reduce net greenhouse gas emissions by at least 55% by 2030 compared to 1990 levels and amends the binding target for the share of renewable energy in the EU's energy mix to 40% by 2030 [2]. In the United States, reducing emissions by 40% by 2030 includes significant investments in renewable energy, electric vehicles, and other green technologies. China is focused on raising the share of non-fossil fuels in primary energy consumption to about 20% by 2025 and to peak carbon emissions before 2030.

Renewable energy for Bangladesh's position in climate action aims to generate 10% of its energy from renewable sources by 2025, with a long-term target of 40% by 2041. Significant investments in solar power, including the development of large-scale solar parks and off-grid solar home systems, have made Bangladesh a leader in off-grid solar solutions. Emerging focus on wind and biomass energy to diversify the renewable energy portfolio. Bangladesh is highly vulnerable to the effects of climate change, such as sea level rise and extreme weather events. The country has implemented robust adaptation measures, including cyclone shelters, improved drainage systems, and climate-tolerant infrastructure. Actively seek international climate finance to support

adaptation and mitigation efforts. Bangladesh has been vocal in favour of establishing a loss and damage fund at COP27. The Bangladesh Climate Change Strategy and Action Plan (BCCSAP) is a comprehensive plan outlining the country's approach to climate adaptation, mitigation, and capacity building. The Renewable Energy Policy (2008) provides incentives and a framework for promoting renewable energy development, including tariff benefits, subsidies, and feed-in tariffs. Despite the high risk of climate change impacts, Bangladesh is making significant progress in renewable energy and climate adaptation. The country's proactive policies, international cooperation, and ambitious goals align with the global objectives set out in the Paris Agreement and the COP meeting [2]. As global regulations and commitments intensify, Bangladesh's efforts in renewable energy and sustainability are crucial to its resilience and contribution to global climate action.

Although fossil fuels have been around for millions of years, human civilization began using them only 200 years ago. But it's hard to prognosticate how long it will last because fossil fuel reserves are being discovered almost every year. Some research reports have predicted the depletion of fossil energy reserves. Therefore, people today are using renewable energy to combat climate change, fossil fuel conservation, and environmental pollution, which are produced through the use of a variety of natural resources including sunlight, wind, water wave and tidal energy, bioenergy, geothermal, ocean waves, ocean heat, tidal, hydrogen fuel cells, and biogas. The electricity and thermal energy sectors are more affected by climate change than any other sector of the global economy. According to a report by think tank Ember, the electricity sector is the largest source of Carbon dioxide emissions [3]. But the International Energy Agency 2022 says the decarbonization of the power sector is underway, and to achieve this milestone, wind and solar will need to make up 41 percent of global electricity generation by 2030, with solar up 24 percent and wind up 17 percent over the previous year [4]. World leaders are working together on this problem. According to experts, there is no alternative to renewable energy to combat climate change. With the development of civilization, the use of electricity and heat is increasing every day. It has been described in various papers below that a large amount of greenhouse gases is being emitted in the power sector today, which is a threat to the environment in the coming days. Therefore, researchers are using different types of renewable energy in the power sector and have developed models showing that using renewable energy compared to fossil fuels reduces carbon emissions reduces greenhouse gas emissions, and also helps to keep the environment sustainable.

To strengthen research on sustainable and renewable energy models, models often estimate the continuous availability of renewable resources, such as sunlight, wind, and water flow, by making a more thorough examination of the model's assumptions, constraints, and possible extensions. Assumptions about the efficiency and performance of renewable energy technologies can significantly influence the model's results. Incorporates realistic efficiency rates and degradation over time into models. The model often assumes the constant availability of wind resources. Changes in the model can be observed by including temporal and spatial variability of wind speed. Includes historical data and climate projections to account for seasonal and geographic variations. One of the limitations is the integration of renewable energy into the existing power grid. The models have to deal with the technical challenges of grid stability, energy storage, and transmission losses. The availability of land and water resources for renewable energy projects such as solar farms and hydropower creates practical limitations. Availability of suitable land for wind farms and their environmental impacts. Assesses land use conflicts, impacts on wildlife, and community acceptance. Offshore wind can be considered as an alternative. Expanding the models to include hybrid renewable energy systems can improve reliability and efficiency. For example, combining solar, wind, and biomass can provide more consistent energy and reduce dependence on a single source. Combine wind energy with solar, biomass, and other renewable

sources. Increases reliability and streamlines supply. Dynamic simulation models can optimize such hybrid systems.

By critically examining and incorporating these assumptions, limitations, and extensions, researchers can develop more accurate and comprehensive models for sustainable and renewable energy systems. This holistic approach will better inform policy-making, investment decisions, and strategic planning of renewable energy infrastructure.

Proposed a mathematical model in which the Bangladeshi analyzed the greenhouse gas emission rate as a result of the use of fuel in various power stations. It collected parameters related to greenhouse gas emissions from various power stations in Bangladesh and in the simulation using HOMER software found that the majority of greenhouse gas emissions in the power sector are dependent on coal [5]. Increasing the use of renewable energy in these sectors will meet the demand for electricity or heat on the one hand, while reducing the adverse impact on the environment. For this, humanity has to increase the use of renewable energy by changing our dependence on fossil fuel energy for electricity and heat generation. A power generation and transmission company, especially suitable for CELECEP, has started to work together with the agreements reached by countries in the 2030 Agenda, taking into account all the Sustainable Development Goals [6]. Among electric companies, SDG priorities are matched by efficient energy, innovation, and adequate infrastructure that is environmentally friendly, and responsibly combating climate change. If this continues, it will be possible to reduce global greenhouse gas emissions by 2050. The production of such coal-based electricity will reduce fossil fuels on the one hand and pollute the environment on the other. Some research reports have predicted the depletion of fossil energy reserves and briefly described that due to limited fossil fuel and environmental pollution, fossil fuel-based power plants are declining worldwide today. Saving the world from this will be realized only when renewable energy is replaced by electricity and renewable energy is compared with non-renewable energy, if the price of fossil fuel can be increased by making the price of renewable energy friendly, then it can be easily replaced. There are different types of renewable energy such as wind, water, solar, wave, tidal, etc. which play a huge role in generating electricity today. These energies emit some carbon, but very little in quantity, which helps to keep the environment sustainable. The review showed that offshore wind technologies emit the lowest GHG emissions (average life cycle GHG emissions can be 5.3 to 13 g Carbon dioxide-eq/kWh). Results comparing GHG projections by fossil fuel heat and electricity indicate that life cycle GHG emissions are relatively high compared to renewable sources, excluding nuclear-based power generation [7]. This study has shown that the analysis of GHG emissions in the life cycle is an effective tool for assessing the environmental impacts of renewable energy technologies.

Recent advances in environmental sustainability and renewable energy modeling have focused on improving the efficiency, integration, and resilience of renewable energy systems. Combining different renewable energy sources, such as solar, wind, and biomass, in a hybrid system can improve reliability and efficiency. Studies on hybrid systems show that they can provide more consistent energy, reduce dependence on fossil fuels, and reduce greenhouse gas emissions. Dynamic simulation models help optimize the operation of these hybrid systems by accounting for different resource availability and demand patterns, which leads to more effective energy management [8]. Power-to-X (PtX) technology converts surplus renewable electricity into other energy, such as hydrogen or synthetic fuel, which can then be stored and used. These technologies address the mismatch between renewable energy production and demand, increasing system flexibility and reliability. Recent advances in PtX include more efficient electrolyzers for hydrogen production and innovative methods of carbon capture and utilization in the production of synthetic fuels. Integrating renewable energy systems into the urban environment is a growing field of research. This includes the use of building-integrated photovoltaics (BIPV) urban wind turbines

and decentralized energy systems to create smart, sustainable cities. The studies emphasize the importance of urban planning and policy support in facilitating the adoption of renewable energy technologies in cities, addressing challenges such as space constraints and aesthetic considerations [9].

The developed world is now turning to electric vehicles to prevent environmental pollution and increased costs of fossil fuels. Electric vehicles are making the future of transportation easier. Electric vehicles have now appeared on the streets of Bangladesh such as autos, rickshaws, vans, etc. Greenhouse gas emissions, especially Carbon dioxide are increasing due to the rapid growth of EVs in Bangladesh. So, proposing an EVCS model based on solar and biogas found that a conventional grid-based charging station reduces Carbon dioxide emissions by 34.68% compared to conventional charging stations [10–12]. As the use of electricity increases, the residents of Bangladesh are suffering from load shedding, and the use of renewable energy can contribute a lot to meet this demand. In addition to energy production, Bangladesh needs to increase consumer knowledge and reduce power wastage to conserve energy, which will reduce the pressure on the power supply [13]. Briefly describe the PV power plant produced electricity from PV technology depending on the solar radiation and other meteorological variables in the desert climate conditions per hour and is the combination of the ambient air temperature and relative humidity of the PV power output of all technologies is related to the sky conditions [14].

To provide a comprehensive analysis of the importance of renewable energy in sustainable power generation, the model can include various renewable energy sources such as solar and hydroelectric, but only wind energy has been used in this paper. Solar energy is one of the most abundant and widely used forms of renewable energy. Advances in photovoltaic (PV) technology have significantly improved the efficiency and cost-effectiveness of solar power. Research indicates that combining solar energy with other renewable sources can increase the stability and reliability of power grids. For example, a study on hybrid systems consisting of PV and thermal solar collectors Carbon dioxide emissions and high profitability. Hydroelectricity remains the basis of renewable energy due to its ability to generate consistent and large-scale electricity [8]. Recent advances focus on small-scale hydropower systems that can be integrated into existing water infrastructure, reducing environmental impact while maximizing energy output. The versatility of hydropower, from large dams to small micro-hydro systems, makes it an important component of a sustainable energy mix. Biomass energy, derived from organic matter, provides a renewable source that can be used for both electricity generation and heating. The development of advanced biomass conversion technologies such as pyrolysis and gasification increases the efficiency and environmental benefits of biomass energy. Combining biomass with other renewable sources can help solve breakage problems and provide a stable energy supply. Advanced modeling and simulation techniques are crucial for optimizing the integration of multiple renewable energy sources. Dynamic simulation models, such as those used for hybrid renewable energy plants, help design and operate systems that can adapt to different energy demand and supply conditions. These models are essential for effectively planning and managing renewable energy resources. By incorporating a diverse range of renewable energy sources into their models, researchers can develop more robust and sustainable power generation systems. This holistic approach ensures that the benefits of each type of renewable energy are maximized, contributing to a more reliable and environmentally friendly energy landscape.

Carbon emissions have become a major cause of extreme environmental pollution, with negative implications for human life whether a country's economy is developed or underdeveloped. Therefore, reducing such emissions in developing countries is critical to sustaining economic growth [15]. South Asia's transnational capital flows are reducing Carbon dioxide, while energy consumption and economic growth are hurting the environment. The study, which takes into account FDI

and trade, inverted U-shaped concluded that there is an inverted U-shaped relationship between economic growth and Carbon dioxide emissions in the short and long term for Malaysia. To achieve long-term environmental and economic goals, governments must take transformational initiatives towards green energy and less polluting economic growth sectors. He has proposed and analyzed a mathematical model to increase the production capacity by absorbing GHG by sowing seeds in a dynamic system of green buildings [16].

Greenhouse gases capture heat and warm the Earth. Almost all of the rise in greenhouse gases in the atmosphere over the past 150 years has been attributed to human activity. In the United States of America, the majority of greenhouse gases released from human activity are the use of fossil fuels for energy production, heating, and transportation. Figure 1 represents the percentage of

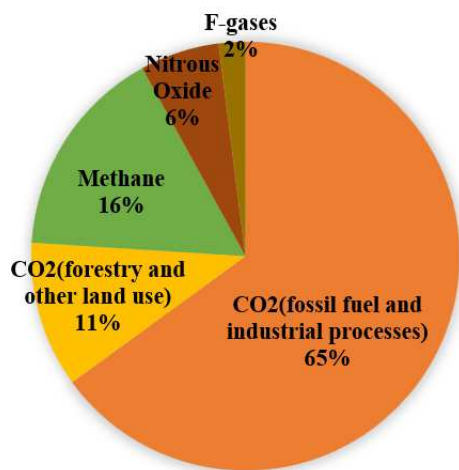


Figure 1. Global GHGs emissions by gas [17]

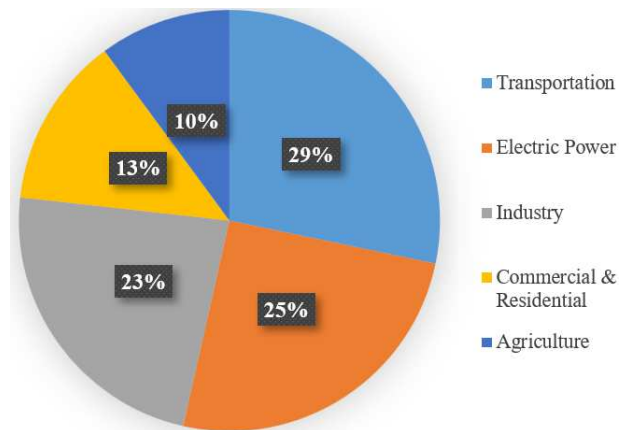


Figure 2. U.S. Greenhouse gases emissions by different sectors in 2021 [18]

common GHGs in the environment in 2022 which implies that Carbon dioxide is the main gas of GHGs. In Figure 2, it is illustrated that the yearly study estimates total national greenhouse gas emissions from human activities. In Figure 3, for the fiscal year 2021–22, the total electricity output

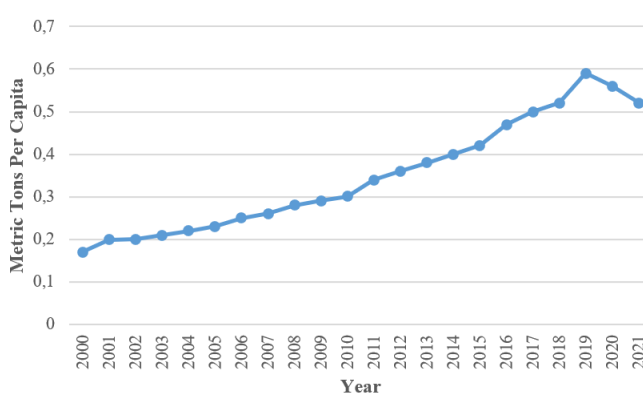


Figure 3. Bangladesh carbon CO<sub>2</sub> emissions [18]

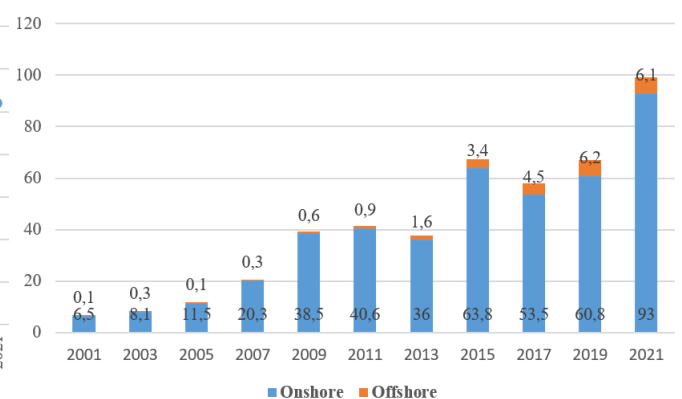
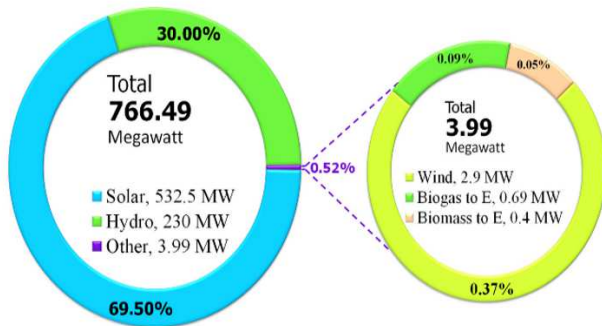
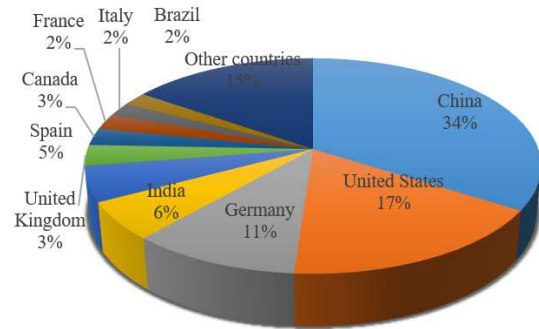


Figure 4. New installations of global wind power [18]

was 85,607 GWh, which was the previous year’s net production of 80,423 GWh [13]. Figure 4 shows the historic expansion of new global wind power projects (2001-2021). In 2021, worldwide wind energy produced a total of 837 GW (more than 780 GW from onshore and 57 GW from offshore), a progress of 12% compared to 2020, with roughly 93.6 GW (72.5 GW from onshore and the rest from offshore) of new capacity added to the global grids. To improve the presentation



**Figure 5.** Current status of RE production capacity of the country [13]



**Figure 6.** Top 10 countries of worldwide total wind power installation in 2021 [18]

of numerical findings and better illustrate the behavior of models and the impact of renewable energies, various types of visual aids can be effectively used such as a time series graph, this graph shows the daily change in the production of solar and wind energy compared to the demand in a month. Highlights how renewable energy production and demand change over time, daily or seasonal variations in solar and wind energy production compared to energy demand, and periods of surplus or deficit, helping to understand the need for energy storage and grid management [8]. Pie chart and bar graph, this pie chart illustrates the percentage contribution of solar, wind, hydro, and biomass to the total energy mix. Representing the contribution of different energy sources to the total energy mix, showing the percentage of energy generated from solar, wind, hydropower, and biomass, provides a clear snapshot of the energy mix and can be used to compare different scenarios or regions. A Geographic Information System (GIS) map, showing spatial data related to renewable energy resources and infrastructure, showing the geographical distribution of solar radiation, wind speed, or location of renewable energy installations, shows the regional potential for renewable energy projects and increases the planning burden.

Many theoretical models were described and many models were proposed considering one or two species related to the work. In this research, we have developed a model taking into account the above discussions to analyze the impact of rapidly increasing GHGs from the electricity sector and after using renewable energy in the electricity sector. Then based on some basic assumptions and based on the formulation of newly separated optimal control problems for reducing emissions, renewable energy has been used to the maximum. Renewable energy sources come from naturally occurring sources that regenerate themselves through natural factors. Renewable energy sources have been identified as the key answer to mitigation of greenhouse gas emissions climate change, and environmental pollution. As the world's population and economy keep expanding, so does the energy need, a scenario that naturally boosts the demand and consumption of conventional sources of energy, particularly fossil fuels. Fossil fuels constitute the principal type of energy sources that generate serious environmental pollution. Therefore, replacing fossil fuels with renewable energy sources in electricity generation is a significant step to minimize carbon emissions. The wind has been used by man for a very long period to operate windmills, pumps, sailing ships, and mechanical energy for industrial activities. Wind turbine generators are used to create electric power and provided around 6% of global electricity in 2019. Through sustainable energy, the dependence on fossil fuel sources is reduced while increasing the usage of renewable sources of energy thus reducing greenhouse gases. Researchers are using the Lotka Volterra model to perform various tasks such as the biographies of people near coastal areas as a result of climate change [19]. A combined plankton-oxygen kinetics model showed that the rate of oxygen production gradually changes over time due to ocean warming [20]. A non-linear mathematical

model has been formulated with the assistance of such different papers and it consists of four species to describe the positive effects of increasing the use of renewable energy sources. To show the impacts of the other dynamical model by increasing renewable energy, analytical analysis has been conducted for the expanded dynamical model and also numerical simulations have been performed.

## 2 Mathematical formulation of the model

To describe the effect of environmental sustainability because of increasing the use of renewable energy in the power sectors. The consequences and preventative measures that the government should take in response to environmental problems can be readily ascertained by examining these interconnections. A progressive system has been considered, involving four dynamical variables the density of greenhouse gases  $G(t)$ , electricity produced i.e. coal-based  $P(t)$ , renewable energy i.e. wind  $R(t)$  environmental sustainability  $E(t)$ . Renewable energy sources have been identified as the main solution for mitigation of greenhouse gas emissions climate change, and environmental pollution. The interrelationship of the previously described dynamical system is shown in Figure 7.

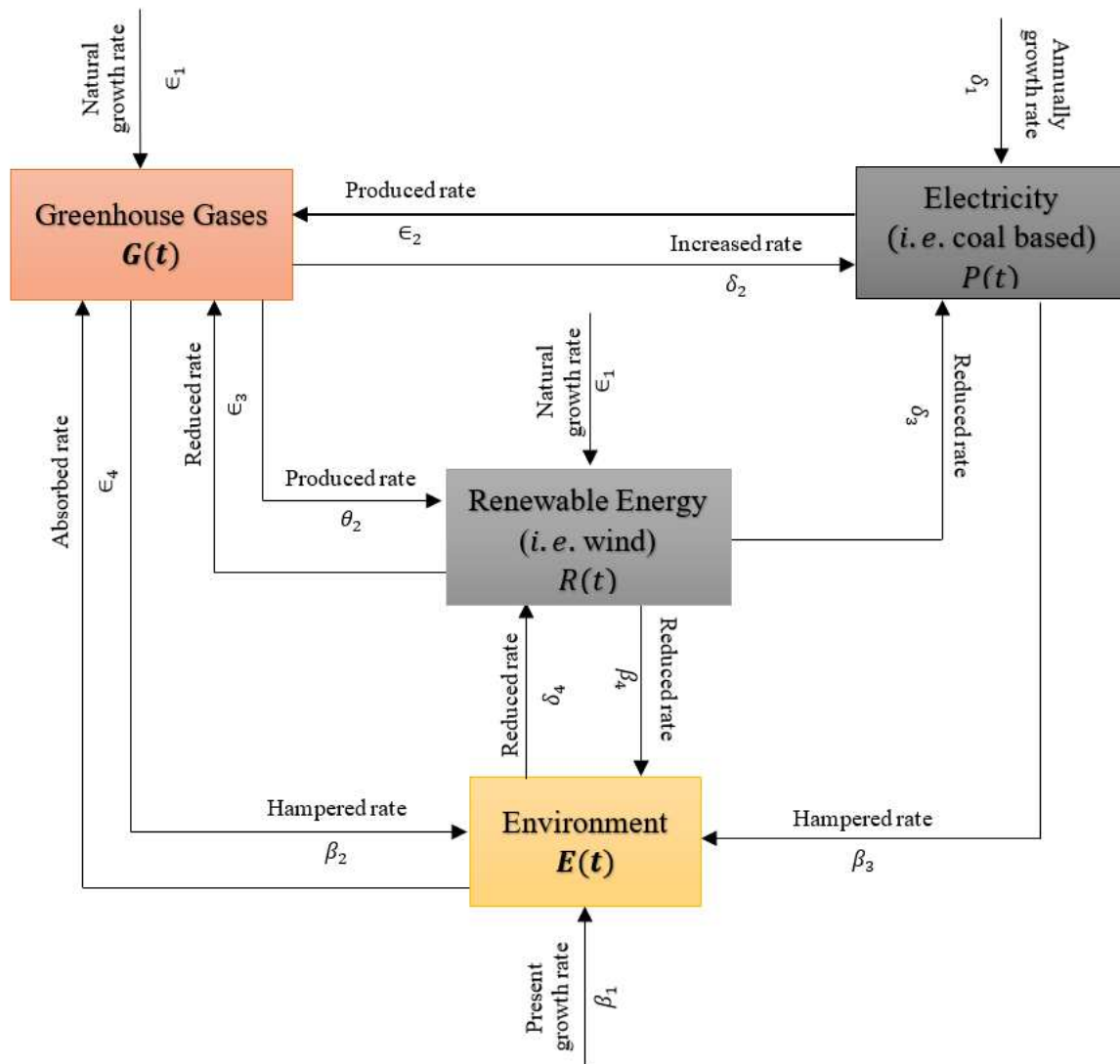


**Figure 7.** Impacts of the use of renewable energy on the GHGs, coal-based electricity and environment in the power sector

$$\begin{aligned}
\frac{dG}{dt} &= \epsilon_1 G + \epsilon_2 GP - \epsilon_3 GR - \epsilon_4 GE, \\
\frac{dP}{dt} &= \delta_1 P \left(1 - \frac{P}{k}\right) + \delta_2 PG - \delta_3 PR, \\
\frac{dR}{dt} &= \theta_1 R + \frac{\theta_2 R}{a + G} - \theta_3 RE + \theta_4 R, \\
\frac{dE}{dt} &= \beta_1 E - \beta_2 EG - \beta_3 EP + \beta_4 ER + \beta_5 E,
\end{aligned} \tag{1}$$

with initial conditions  $G_0 = G(0) > 0$ ,  $P_0 = P(0) \geq 0$ ,  $R_0 = R(0) > 0$ ,  $E_0 = E(0) > 0$ . In model (1),  $G(t)$ ,  $P(t)$ ,  $R(t)$  and  $E(t)$  are denoted by the greenhouse gas, the electricity produces i.e. coal-based, renewable energy i.e. wind, and environmental sustainability, respectively. The first equation  $\frac{dG}{dt}$  represents the rate of change greenhouse gases where  $\epsilon_1$  is the natural growth rate of the greenhouse gas;  $\epsilon_2$  is the producing rate of the greenhouse gas by the electricity produced i.e. burning coal;  $\epsilon_3$  is the reducing rate of greenhouse gas by using renewable energy i.e. wind in the electricity;  $\epsilon_4$  is the net absorbing rate of greenhouse gas by the environment where  $\epsilon_4 = \epsilon_5 - \epsilon_6$  (here  $\epsilon_5$  is the natural absorption rate of the greenhouse gas and is the producing rate of the greenhouse gas after a natural disaster). The second governing equation  $\frac{dP}{dt}$  represents the rate of change of coal-based electricity production where  $\delta_1$  is the annually produced rate of electricity;  $\delta_2$  is the increasing rate of electricity demand for the effect of temperature due to increasing GHGs;  $\delta_3$  is the net reducing rate of coal-based electricity due to using renewable energy i.e. wind, where  $\delta_3 = \delta_5 - \delta_6$  (here  $\delta_5$  is the reducing rate of coal-based electricity due to using renewable energy i.e. wind and is the increasing rate of electricity by using renewable energy i.e. wind).

The third governing equation  $\frac{dR}{dt}$  represents the rate of change of renewable energy i.e. wind where  $\theta_1$  is the annually produced rate of renewable energy;  $\theta_2$  is the increasing changing rate of renewable energy (i.e. wind energy) by the effect of climate change due to increasing GHGs;  $\theta_3$  is the reducing potential rate of renewable energy sources i.e. wind due to (adverse) environmental factors;  $\theta_4$  is the highest producing rate of renewable energy i.e. wind in April where  $\theta_4 = \theta_5 - \theta_6$  (here  $\theta_5$  is the highest producing rate of renewable energy i.e. wind in April and is the lowest producing rate of renewable energy i.e. wind in November). The fourth governing equation  $\frac{dE}{dt}$  represents the rate of change of environmental sustainability where  $\beta_1$  is the present environmental quality;  $\beta_2$  is the hampering rate of environment quality by the greenhouse gas;  $\beta_3$  is the hampering rate of environment quality by producing electricity (i.e. burning coal);  $\beta_4$  is the produced rate of environmental sustainability (or, reducing the rate of environment pollution) by the use of renewable energy in the electricity sector;  $\beta_5$  is the increasing rate of environmental pollution due to without electricity i.e. coal-based.

### 3 Analytical analysis

In this section, the positivity test of all variables, boundedness of the system, stability analysis at equilibrium points and sensitivity analysis are demonstrated.

#### Positivity test

**Lemma 1** *Let  $G(0) > 0$ ,  $P(0) \geq 0$ ,  $R(0) > 0$ ,  $E(0) > 0$ , and  $(G(t), P(t), R(t), E(t)) \in \mathbb{R}_4^+$ , then the solutions  $G(t)$ ,  $P(t)$ ,  $R(t)$ ,  $E(t)$  of the model are non-negative.*

**Proof** To verify the lemma, system (1) has been employed. For this, the first equation of the system is considered as given

$$\frac{dG}{dt} = \epsilon_1 G + \epsilon_2 GP - \epsilon_3 GR - \epsilon_4 GE. \tag{2}$$

To find the positivity, Eq. (2) can be written as  $\frac{dG}{dt} \geq (\epsilon_1 + \epsilon_2 P) G \Rightarrow \frac{dG}{dt} \geq A_1 G$ , where  $A_1 = \epsilon_1 + \epsilon_2 P$ . Then  $\Rightarrow \frac{dG}{G} \geq A_1 dt$  that yields  $\Rightarrow \ln G \geq A_1 t + \ln d_1$ , where  $d_1$  is an integrating constant,

$$G(t) \geq d_1 e^{A_1 t}. \tag{3}$$

Now applying the initial condition at  $t = 0$ ,  $G(0) = G_0 > 0$ , then from Eq. (3), we have  $G(0) = G_0 \geq d_1$ . Putting the value of  $d_1$  in Eq. (3), we obtain  $G(t) \geq G_0 e^{A_1 t}$ . When  $t \rightarrow \infty$ ,  $G(t) > 0$ , means that  $G(t)$  is positive for all  $t \geq 0$ . By following the same way, it can be obtained for other compartments. Therefore,  $G(t) \geq 0$ ,  $P(t) \geq 0$ ,  $R(t) \geq 0$  and  $E(t) \geq 0$ ,  $\forall t \geq 0$ . Hence, the lemma is proved.

### Boundedness of the equation

Now, it is established that the proposed system is bounded. By the following Lemma 2, it is started to be proved.

**Lemma 2** *The set*

$$\Psi = \left\{ (G, P, R, E) \in \mathfrak{R}_4^+ : h(t) = G(t) + P(t) + R(t) + E(t), 0 \leq h(t) \leq \frac{\omega}{\rho} \right\},$$

*is a region of attraction for each solution and initially all the variables are positive, where  $\rho$  is a constant.*

**Proof** Let

$$h(t) = G(t) + P(t) + R(t) + E(t),$$

and  $\rho > 0$  be a constant. Then it can be written

$$\frac{dh}{dt} = \frac{dG}{dt} + \frac{dP}{dt} + \frac{dR}{dt} + \frac{dE}{dt}.$$

$$\begin{aligned} \frac{dh}{dt} = & \epsilon_1 G + \epsilon_2 GP - \epsilon_3 GR - \epsilon_4 GE + \delta_1 P \left( 1 - \frac{P}{k} \right) + \delta_2 PG - \delta_3 PR \\ & + \theta_1 R + \frac{\theta_2 R}{a + G} - \theta_3 RE + \theta_4 R + \beta_1 E - \beta_2 EG - \beta_3 EP + \beta_4 ER + \beta_5 E, \end{aligned}$$

$$\begin{aligned} \frac{dh}{dt} + \rho h = & (\epsilon_1 + \rho) G + (\delta_1 + \rho) P + (\theta_1 + \theta_4 + \rho) R + (\beta_1 + \beta_5 + \rho) E \\ & + (\epsilon_2 P - \epsilon_3 R - \epsilon_4 E + \delta_2 P - \beta_2 E) G - \frac{\delta_1 P^2}{k} \\ & - (\delta_3 R + \beta_3 E) P + \left( \frac{\theta_2}{a + G} - \theta_3 E + \beta_4 E \right) R, \end{aligned}$$

$$\begin{aligned} \frac{dh}{dt} + \rho h &\leq (\epsilon_1 + \rho)G + (\delta_1 + \rho)P + (\theta_1 + \theta_4 + \rho)R + (\beta_1 + \beta_5 + \rho)E \\ &\quad + (\epsilon_2P - \epsilon_3R + \delta_2P - \beta_2E)G - \frac{\delta_1P^2}{k} - (\delta_3R + \beta_3E)P + \left(\frac{\theta_2}{a + G} + \beta_4E\right)R, \\ &\leq \omega. \end{aligned} \tag{4}$$

Applying the theory of inequality, we have  $h \leq \frac{\omega}{\rho} + C_0e^{-\rho t}$ . For  $t \rightarrow \infty$  it has been  $0 \leq h \leq \frac{\omega}{\rho}$ . Hence the solution of the system is bounded in  $\Psi$ .

### Equilibrium points

The equilibrium points of the system can be obtained by setting,  $\frac{dG}{dt} = 0, \frac{dP}{dt} = 0, \frac{dR}{dt} = 0, \frac{dE}{dt} = 0$ . The system produces two dynamic equilibrium points  $R_i(\bar{G}, \bar{P}, \bar{R}, \bar{E})$ , where  $i = 1, 2$  and these are shown as

$$\begin{aligned} \text{(i)} \quad R_1(G, P, R, E) &= R_P \left( \frac{I_1R^* + I_2}{I_3}, \frac{I_7R^* + I_8}{I_3\beta_3}, \frac{\beta_1\delta_2 + \beta_5\delta_2}{\beta_2\delta_3} - \frac{\beta_1 + \beta_5}{2\beta_4}, \frac{I_4R^* + I_5}{I_6 + \theta_3I_1R^*} \right). \\ \text{(ii)} \quad R_2(\bar{G}, 0, \bar{R}, \bar{E}) &= R_P \left( \frac{\beta_1 + \beta_4\bar{R} + \beta_5}{\beta_2}, 0, \frac{\theta_3\epsilon_1 - \theta_1\epsilon_4 - \theta_4\epsilon_4}{2\theta_3\epsilon_3} - \frac{a\beta_2 + \beta_1 + \beta_5}{2\beta_4}, \frac{\epsilon_1 - \epsilon_3\bar{R}}{\epsilon_4} \right). \end{aligned}$$

### Stability analysis

Now, the system of nonlinear differential equations given by model (1) can be evaluated into the Jacobian matrix given as,

$$J_{(x_1, x_2, x_3, x_4)} = \begin{bmatrix} \epsilon_1 + \epsilon_2P - \epsilon_3R - \epsilon_4E & \epsilon_2G & -\epsilon_3G & -\epsilon_4G \\ \delta_2P & a_{22} & -\delta_3P & 0 \\ -\frac{\theta_2R}{(a+G)^2} & 0 & a_{33} & -\theta_3R \\ -\beta_2E & -\beta_3E & \beta_4E & a_{44} \end{bmatrix}, \tag{5}$$

where  $a_{22} = \delta_1 \left(1 - \frac{2P}{k}\right) + \delta_2G - \delta_3R$ ,  $a_{33} = \theta_1 + \frac{\theta_2}{a+G} - \theta_3E + \theta_4$ , and  $a_{44} = \beta_1 - \beta_2G - \beta_3P + \beta_4R + \beta_5$ .

**Theorem 1** *The system's coexisting equilibrium point is stable or locally stable under certain conditions but unstable otherwise.*

**Proof** The Jacobian matrix given by (5) at the co-existing equilibrium point  $R_1(G, P, R, E) = R_P(G^*, P^*, R^*, E^*)$  takes the following form

$$\begin{aligned} J_{(x_1, x_2, x_3, x_4)} &= \begin{bmatrix} \epsilon_1 + \epsilon_2P^* - \epsilon_3R^* - \epsilon_4E^* & \epsilon_2G^* & -\epsilon_3G^* & -\epsilon_4G^* \\ \delta_2P^* & a_{22} & -\delta_3P^* & 0 \\ -\frac{\theta_2R^*}{(a+G^*)^2} & 0 & a_{33} & -\theta_3R^* \\ -\beta_2E^* & -\beta_3E^* & \beta_4E^* & a_{44} \end{bmatrix} \\ &= \begin{bmatrix} \epsilon_1 + \epsilon_2P^* - \epsilon_3R^* - \epsilon_4E^* & \epsilon_2G^* & -\epsilon_3G^* & -\epsilon_4G^* \\ 0 & b_{22} & b_{23} & b_{24} \\ 0 & 0 & c_{33} & c_{34} \\ 0 & 0 & 0 & d_{44} \end{bmatrix}. \end{aligned}$$

The characteristic equation of the system takes the form as

$$(\epsilon_1 + \epsilon_2P^* - \epsilon_3R^* - \epsilon_4E^* - \lambda_1)(b_{22} - \lambda_2)(c_{33} - \lambda_3)(d_{44} - \lambda_4) = 0.$$

Hence the eigenvalues are

$$\begin{aligned}\lambda_1 &= \epsilon_1 + \epsilon_2 P^* - \epsilon_3 R^* - \epsilon_4 E^*, \\ \lambda_2 &= b_{22} = \delta_1 \left(1 - \frac{2P^*}{k}\right) + \delta_2 G^* - \delta_3 R^* + \frac{\delta_2 P^* \epsilon_2 G^*}{\epsilon_1 + \epsilon_2 P^* - \epsilon_3 R^* - \epsilon_4 E^*}, \\ \lambda_3 &= c_{33} = b_{33} - \eta_4 b_{23}, \\ \lambda_4 &= d_{44} = c_{44} - \eta_6 c_{34}.\end{aligned}$$

Therefore, the co-existing equilibrium may be a locally stable point when

$$\begin{aligned}\epsilon_1 + \epsilon_2 P^* &> \epsilon_3 R^* + \epsilon_4 E^*, \\ \delta_1 + \delta_2 G^* + \frac{\delta_2 P^* \epsilon_2 G^*}{\epsilon_1 + \epsilon_2 P^* - \epsilon_3 R^* - \epsilon_4 E^*} &> \delta_1 \frac{2P^*}{k} + \delta_3 R^*, b_{33} > \eta_4 b_{23}, c_{44} > \eta_4 c_{34},\end{aligned}$$

or, it may be stable when

$$\begin{aligned}\epsilon_1 + \epsilon_2 P^* < \epsilon_3 R^* + \epsilon_4 E^*, \delta_1 + \delta_2 G^* + \frac{\delta_2 P^* \epsilon_2 G^*}{\epsilon_1 + \epsilon_2 P^* - \epsilon_3 R^* - \epsilon_4 E^*} < \delta_1 \frac{2P^*}{k} + \delta_3 R^*, \\ b_{33} < \eta_4 b_{23}, c_{44} < \eta_4 c_{34}, \text{ otherwise, it is unstable.}\end{aligned}$$

**Theorem 2** *The system's coal-free power plant equilibrium point is stable or locally stable under certain conditions but unstable otherwise.*

**Proof** The Jacobian matrix given in Eq. (5) at the coal-free electricity equilibrium point  $R_2(G, 0, R, E) = R_P(\bar{G}, 0, \bar{R}, \bar{E})$  takes the following form:

$$\begin{aligned}J_{(x_1, x_2, x_3, x_4)} &= \begin{bmatrix} \epsilon_1 - \epsilon_3 \bar{R} - \epsilon_4 \bar{E} & \epsilon_2 \bar{G} & -\epsilon_3 \bar{G} & -\epsilon_4 \bar{G} \\ 0 & \delta_1 + \delta_2 \bar{G} - \delta_3 \bar{R} & 0 & 0 \\ -\frac{\theta_2 \bar{R}}{(a + \bar{G})^2} & 0 & a_{33} & -\theta_3 \bar{R} \\ -\beta_2 \bar{E} & -\beta_3 \bar{E} & \beta_4 \bar{E} & a_{44} \end{bmatrix} \\ &= \begin{bmatrix} \epsilon_1 - \epsilon_3 \bar{R} - \epsilon_4 \bar{E} & \epsilon_2 \bar{G} & -\epsilon_3 \bar{G} & -\epsilon_4 \bar{G} \\ 0 & \delta_1 + \delta_2 \bar{G} - \delta_3 \bar{R} & 0 & 0 \\ 0 & 0 & b_{33} & b_{34} \\ 0 & 0 & 0 & d_{44} \end{bmatrix}.\end{aligned}$$

The characteristic equation of the above matrix takes the following form:

$$|J_{R_P} - \bar{\lambda}I| = 0,$$

$$\Rightarrow \begin{bmatrix} \epsilon_1 - \epsilon_3 \bar{R} - \epsilon_4 \bar{E} - \lambda_1 & \epsilon_2 \bar{G} & -\epsilon_3 \bar{G} & -\epsilon_4 \bar{G} \\ 0 & \delta_1 + \delta_2 \bar{G} - \delta_3 \bar{R} - \lambda_2 & 0 & 0 \\ 0 & 0 & b_{33} - \lambda_3 & b_{34} \\ 0 & 0 & 0 & d_{44} - \lambda_4 \end{bmatrix} = 0,$$

$$\Rightarrow (\epsilon_1 - \epsilon_3 \bar{R} - \epsilon_4 \bar{E} - \lambda_1) (\delta_1 + \delta_2 \bar{G} - \delta_3 \bar{R} - \lambda_2) (b_{33} - \lambda_3) (d_{44} - \lambda_4) = 0.$$

Hence the eigenvalues are

$$\lambda_1 = \epsilon_1 - \epsilon_3 \bar{R} - \epsilon_4 \bar{E}, \quad \lambda_2 = \delta_1 + \delta_2 \bar{G} - \delta_3 \bar{R},$$

$$\lambda_3 = b_{33} = \theta_1 + \frac{\theta_2}{a + \bar{G}} - \theta_3 \bar{E} + \theta_4 + \frac{-\theta_2 \bar{R} \epsilon_3 \bar{G}}{(\epsilon_1 - \epsilon_3 \bar{R} - \epsilon_4 \bar{E})(a + \bar{G})^2}, \quad \text{and}$$

$$\lambda_4 = d_{44} = b_{44} - \eta_{11} b_{34}.$$

Therefore, the coal-free electricity equilibrium may be a locally stable point when

$$\epsilon_1 > \epsilon_3 \bar{R} + \epsilon_4 \bar{E}, \quad \delta_1 + \delta_2 \bar{G} > \delta_3 \bar{R},$$

$$\theta_1 + \frac{\theta_2}{a + \bar{G}} + \theta_4 > \theta_3 \bar{E} + \frac{\theta_2 \bar{R} \epsilon_3 \bar{G}}{(\epsilon_1 - \epsilon_3 \bar{R} - \epsilon_4 \bar{E})(a + \bar{G})^2}, \quad b_{44} > \eta_{11} b_{34},$$

or, it may be stable when the following conditions hold, otherwise, it is unstable:

$$\epsilon_1 < \epsilon_3 \bar{R} + \epsilon_4 \bar{E}, \quad \delta_1 + \delta_2 \bar{G} < \delta_3 \bar{R}, \quad b_{44} < \eta_{11} b_{34},$$

$$\theta_1 + \frac{\theta_2}{a + \bar{G}} + \theta_4 > \theta_3 \bar{E} + \frac{\theta_2 \bar{R} \epsilon_3 \bar{G}}{(\epsilon_1 - \epsilon_3 \bar{R} - \epsilon_4 \bar{E})(a + \bar{G})^2}.$$

#### 4 Numerical simulations

Changes in environmental sustainability, driven by the impact of renewable energy on the power sector, as well as alterations in both greenhouse gas emissions and coal-based power plants are depicted in the dynamics of the model shown in [Table 1](#). The trend of electricity consumption is gradually increasing in the country where most of the fossil fuels such as natural gas, coal, oil, etc. are produced by burning and most of the carbon dioxide is emitted from coal, which is spoiling the environment and increasing greenhouse gases. Coal-based electricity generation typically results in an increase in greenhouse gases and a decrease in environmental sustainability. The depicted figure observed that, if electricity is produced by reducing coal-based electricity production and increasing the use of renewable energy such as wind, solar, hydro, etc., it reduces greenhouse gases and increases environmental sustainability. [Table 1](#) shows the changing rate of all dynamical variables of the model.

**Table 1.** Description and respective values of parameters for the proposed model

Sym	Descriptions of the parameters	Values (year <sup>-1</sup> )	Refs.
$\epsilon_1$	The natural growth rate of the greenhouse gas	1.741e(-8) Gt/GWh	[17, 19]
$\epsilon_2$	Producing rate of the greenhouse gas by the electricity produced i.e. burning coal	1.60e(-5) Gt/GWh	[7, 13, 21]
$\epsilon_3$	Reducing the rate of greenhouse gas by using renewable energy i.e. wind in the electricity	0.0001021 Gt/GWh	[7, 13]
$\epsilon_4$	Net absorbing rate of greenhouse gas by the environment	6.56e(-6) Gt/GWh	[19, 22]

**Table 1.** Description and respective values of parameters for the proposed model - continued

Sym	Descriptions of the parameters	Values (year <sup>-1</sup> )	Refs.
$\epsilon_5$	Naturally absorption rate of the greenhouse gas	0.00676 kg/km <sup>2</sup>	[17, 22]
$\epsilon_6$	Producing rate of greenhouse gas after a natural disaster	0.0005 kg/km <sup>2</sup>	[17, 22]
$\delta_1$	Annually produced rate of electricity	0.0645 GWh	[13, 23]
$k$	carrying capacity of the electricity	10000	[est.]
$\delta_2$	Increasing rate of electricity demand due to increasing GHGs	9.969e(-7) GWh	[23, 24]
$\delta_3$	Reducing the rate of the coal-based electricity (power plant) due to using renewable energy i.e. wind	0.063495 GWh	[19, 21, 25]
$\delta_4$	Reducing rate of the coal-based electricity (power plant) due to environmental pollution	0.0636 GWh	[19, 25]
$\delta_5$	Increasing the rate of electricity by using renewable energy i.e. wind	0.0001048 GWh	[15, 26]
$\theta_1$	Annually growth rate of renewable energy	0.1078 GWh	[13, 26]
$a$	Saturated constant	0.005	[est.]
$\theta_2$	Increasing changing rate of wind energy by the effect of climate change due to increasing GHGs	0.0495 GWh	[7, 13, 17]
$\theta_3$	Reducing the potential rate of renewable energy sources i.e. wind due to (adverse) environmental factors	0.0290 GWh	[5, 13]
$\theta_4$	April has the highest rate of renewable energy	2.474e(-6) GWh	[5, 13]
$\beta_1$	Present environmental quality	0.15	[est.]
$\beta_2$	Hampered rate of environmental quality by the greenhouse gas	0.105	[24, 27]
$\beta_3$	Hampered rate of environment quality by producing electricity (i.e. burning coal)	0.0122	[19, 28]
$\beta_4$	Produced rate of environmental sustainability by the use of renewable energy in the electricity sector	7.27e(-8)	[17, 19]
$\beta_5$	The increasing rate of environmental pollution due to electricity i.e. coal-based (normally pollution)	0.023467	[17, 19]

In this section, the increasing changing rate of renewable energy (i.e. wind energy) is described by the effect of climate change, attributed to the rising GHGs levels in the power sector ( $\theta_2$ ), in relation to the other dynamics of the model shown in [Figure 9](#), [Figure 10](#), [Figure 11](#) and [Figure 12](#). If the wind energy changes continue to increase due to greenhouse gases, the change of greenhouse gases rapidly with different values of wind energy shown in [Figure 9](#).

With the increasing wind energy in the power sector, then coal-based electricity is decreasing rapidly with different values of  $\theta_2$  shown in [Figure 10](#). Climate change is having a clear impact on the weather. Experts say due to this change three seasons are now visible in the country of six seasons. Among them, summer is the most prominent. It is understood that the wind speed is higher in summer than at other times, but in extreme heat, this wind feels less on our bodies. Climate change is changing the wind speed sometimes more or sometimes less thereby affecting wind power that is shown in [Figure 11](#). While the increase in renewable energy in the power sector is reducing coal-based electricity, it is reducing the amount of air pollution in the environment and protecting animals from various problems, reducing the amount of greenhouse gases, thereby helping to keep the environment sustainable that is shown in [Figure 12](#).

The reducing potential rate of renewable energy sources i.e. wind due to (adverse) environmental factors. Due to human activities, the climate is changing, resulting in various problems in the environment such as low pressure and natural disasters. The main source of solar energy production is the sun, if there is a low pressure or the sky is cloudy then our solar energy is interrupted, on the other hand, due to frequent natural disasters the wind speed changes. So, it can be said that an adverse environment destroys the source of renewable energy. Here, [Figure 13](#) represents the decreasing GHGs with different values of  $\theta_3$  when increasing renewable energy due to adverse environmental factors being decreased.

[Figure 14](#) represents the increasing renewable energy after fewer environmental factors in the coal-based power sector are decreased. [Figure 15](#) represents the increasing potential rate of renewable energy sources i.e.

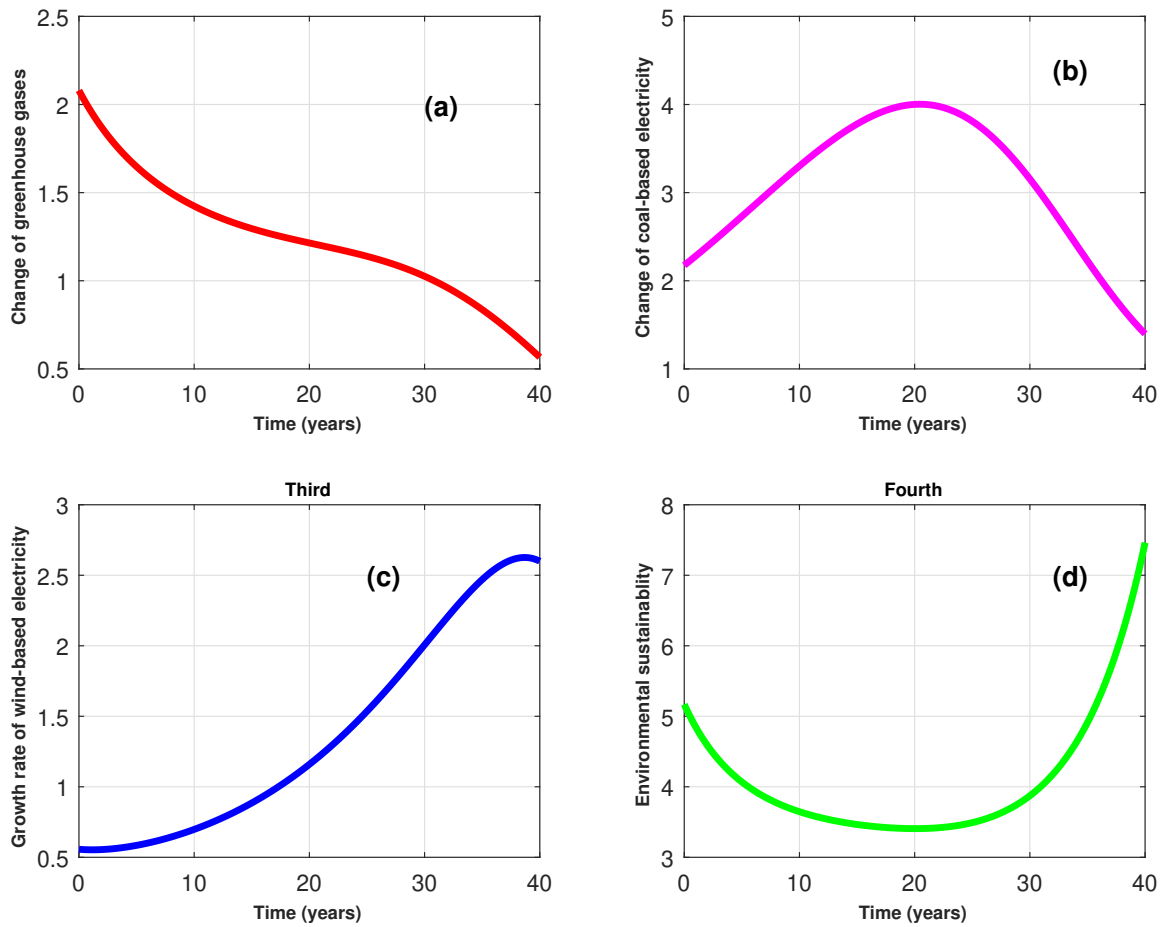


**Figure 8.** Impact of using renewable energy in power sector on the greenhouse gases, coal-based electricity and environmental sustainability

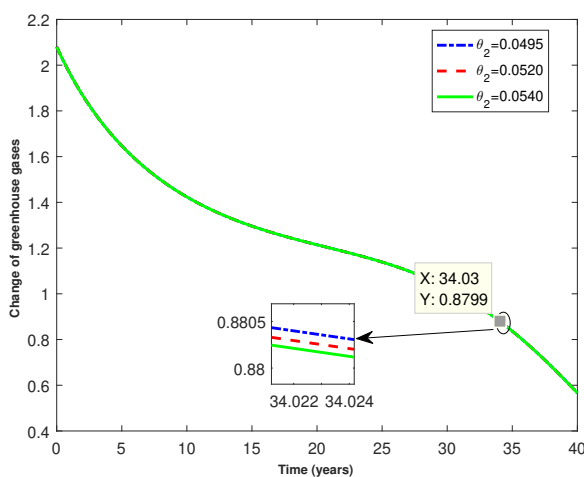


**Figure 9.** Change of greenhouse gases for different values of  $\theta_2$

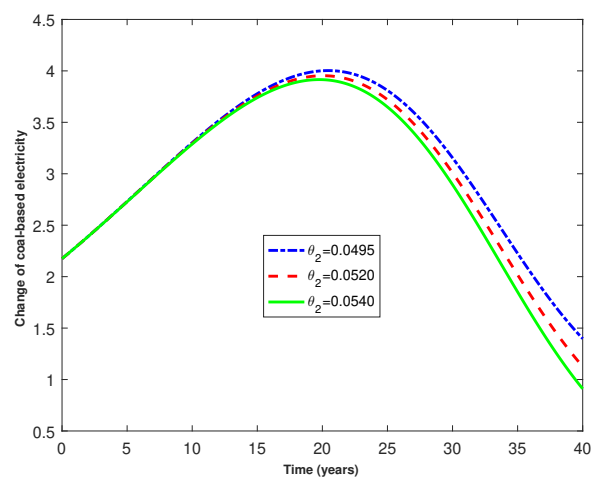


**Figure 10.** Change of coal-based electricity for different values of  $\theta_2$

wind when adverse environmental factors are being decreased. Figure 16 represents the increasing potential rate of renewable energy sources i.e. wind when adverse environmental factors are being decreased. The

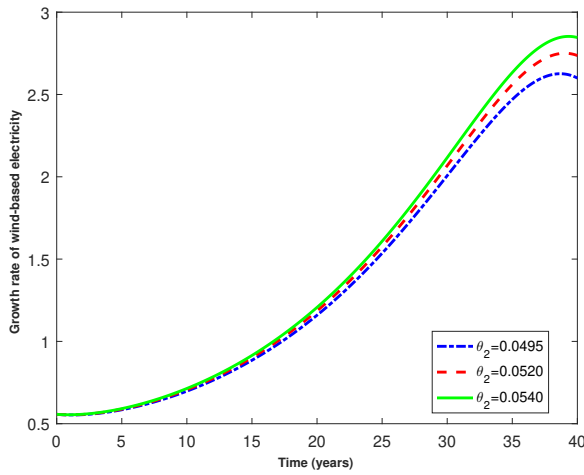


**Figure 11.** Change of wind-based electricity for different values of  $\theta_2$

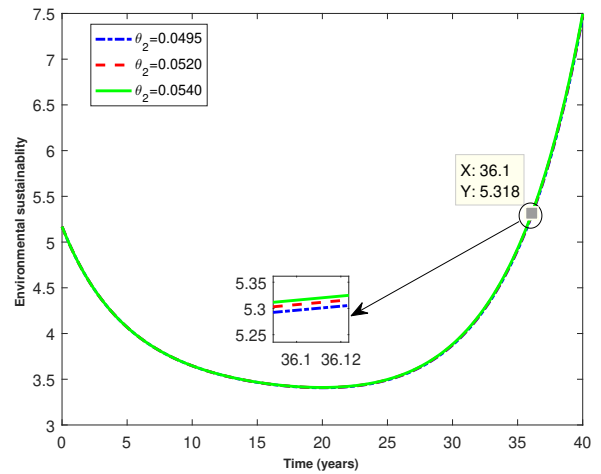


**Figure 12.** Change of ES for different values of  $\theta_2$

amount of load shedding is increasing due to the reduction in power generation due to grid disasters and energy crises. In this situation, it is being planned to reduce load shedding by keeping the amount of renewable energy in full production.

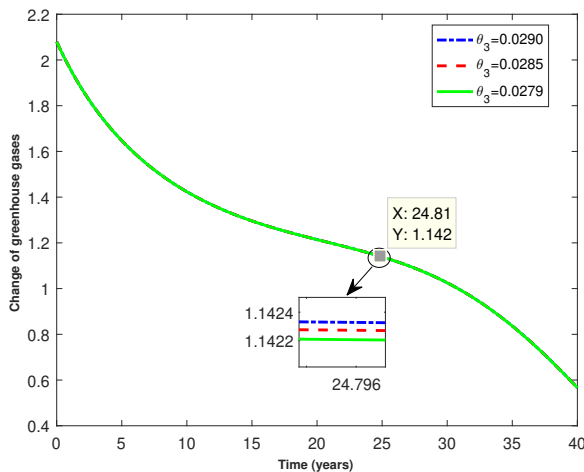


**Figure 13.** Change of greenhouse gases for different values of  $\theta_3$

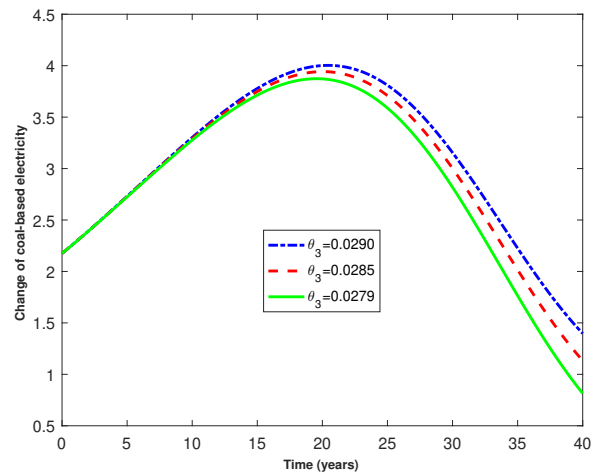


**Figure 14.** Change of coal-based electricity for different values of  $\theta_3$

Using wind power energy, in Figure 17, it is seen that the greenhouse gases are decreasing with different values of  $\epsilon_3$ . The use of renewable energy in the power sector not only reduces greenhouse gas emissions but also helps to sustain the environment as shown in Figure 18, Figure 19 and Figure 20.

### 5 Bifurcation diagram for different variables

Bifurcation analysis is a qualitative shift in the behaviour of dynamics for the verification of one or more parameters which investigates how an ODE depends on parameters. However, a bifurcation diagram depicts the change of equilibrium number concerning parametric variables. For bifurcation analysis, we need the Jacobian matrix of model (1). According to Eq. (5), the characteristic equation of the Jacobian matrix  $J = DF(x)$  is  $Jv = \lambda v$ , where  $\lambda$  and  $v$  are eigenvalues and eigenvectors, respectively. Then at any

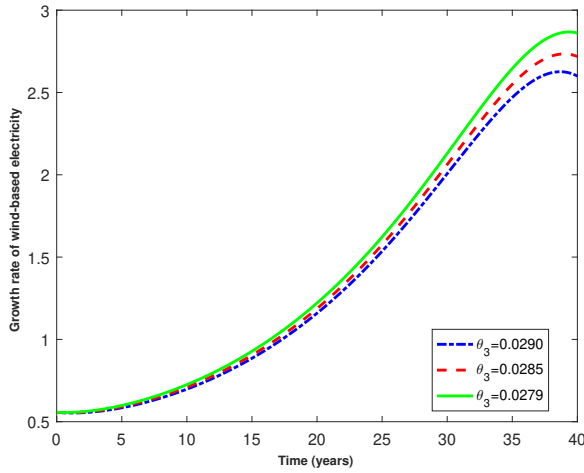


Figure 15. Change of wind-based electricity for different values of  $\theta_3$

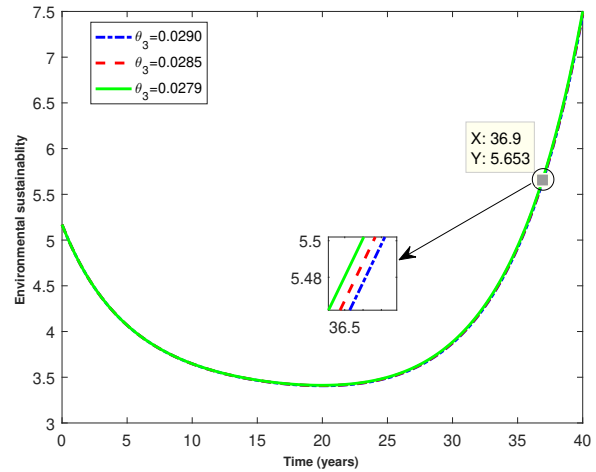


Figure 16. Growth rate of ES for different values of  $\theta_3$

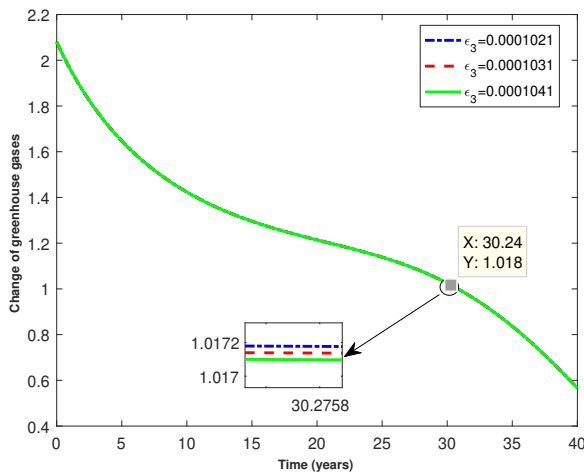


Figure 17. Change of greenhouse gases for different values of  $\epsilon_3$

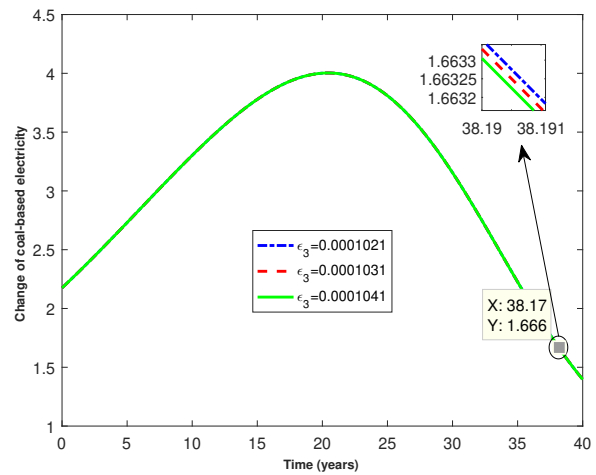


Figure 18. Change of coal-based electricity for different values of  $\epsilon_3$

equilibrium point  $(\tilde{G}, \tilde{P}, \tilde{R}, \tilde{E})$ , the following equation is provided:

$$\begin{bmatrix} \epsilon_1 + \epsilon_2 \tilde{P} - \epsilon_3 \tilde{R} - \epsilon_4 \tilde{E} & \epsilon_2 \tilde{G} & -\epsilon_3 \tilde{G} & -\epsilon_4 \tilde{G} \\ \delta_2 \tilde{P} & a_{22} & -\delta_3 \tilde{P} & 0 \\ -\frac{\theta_2 \tilde{R}}{(a + \tilde{G})^2} & 0 & a_{33} & -\theta_3 \tilde{R} \\ -\beta_2 \tilde{E} & -\beta_3 \tilde{E} & \beta_4 \tilde{E} & a_{44} \end{bmatrix} \begin{bmatrix} v_G \\ v_P \\ v_R \\ v_E \end{bmatrix} = \lambda \begin{bmatrix} v_G \\ v_P \\ v_R \\ v_E \end{bmatrix} \quad (6)$$

The eigenvalues give information on the direction and strength of the attraction and repulsion of the orbit. If the eigenvalues are complex numbers, we obtain a spiral equilibrium. But if the eigenvalues are real numbers, we get a node. Further, by assessing the  $tr(J)$  and  $\det(J)$  at the equilibrium points, we can easily establish whether a bifurcation happens or not and also the type of the equilibrium points i.e. stable, node, saddle, or unstable.

We have a saddle when  $\det(J) < 0$ . But for  $\det(J) > 0$ , we need to determine the  $tr(J)$  value. If  $tr(J) < 0$ , we have a stable point but if  $tr(J) > 0$ , we have an unstable point. Here four diagrams have been tested for bifurcation using 3D numerical simulations. Three alternative dynamics are investigated for various bifurcation analyses. Figure 21 depicts the bifurcation analysis of the proposed model.

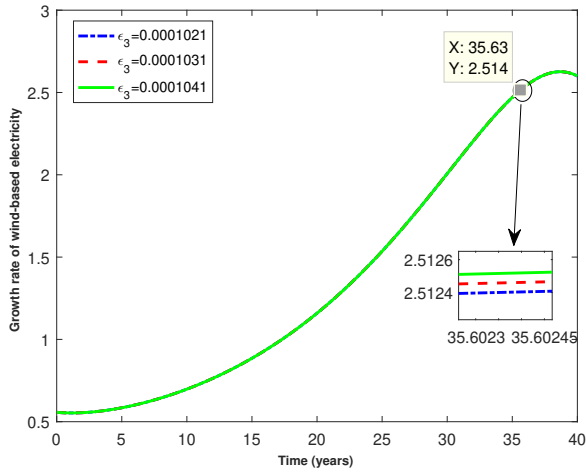


Figure 19. Change of wind-based electricity for different values of  $\epsilon_3$

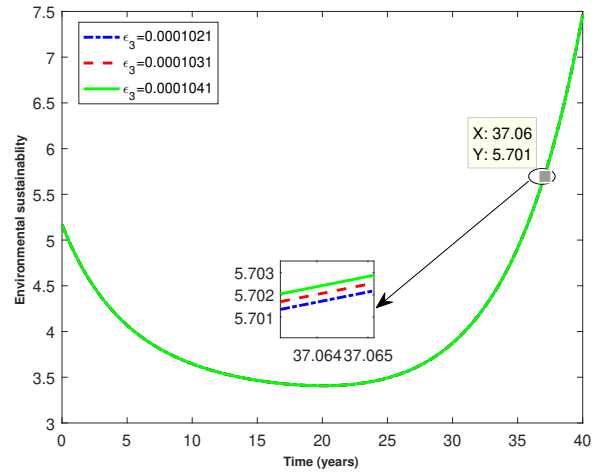


Figure 20. Change of ES for different values of  $\epsilon_3$

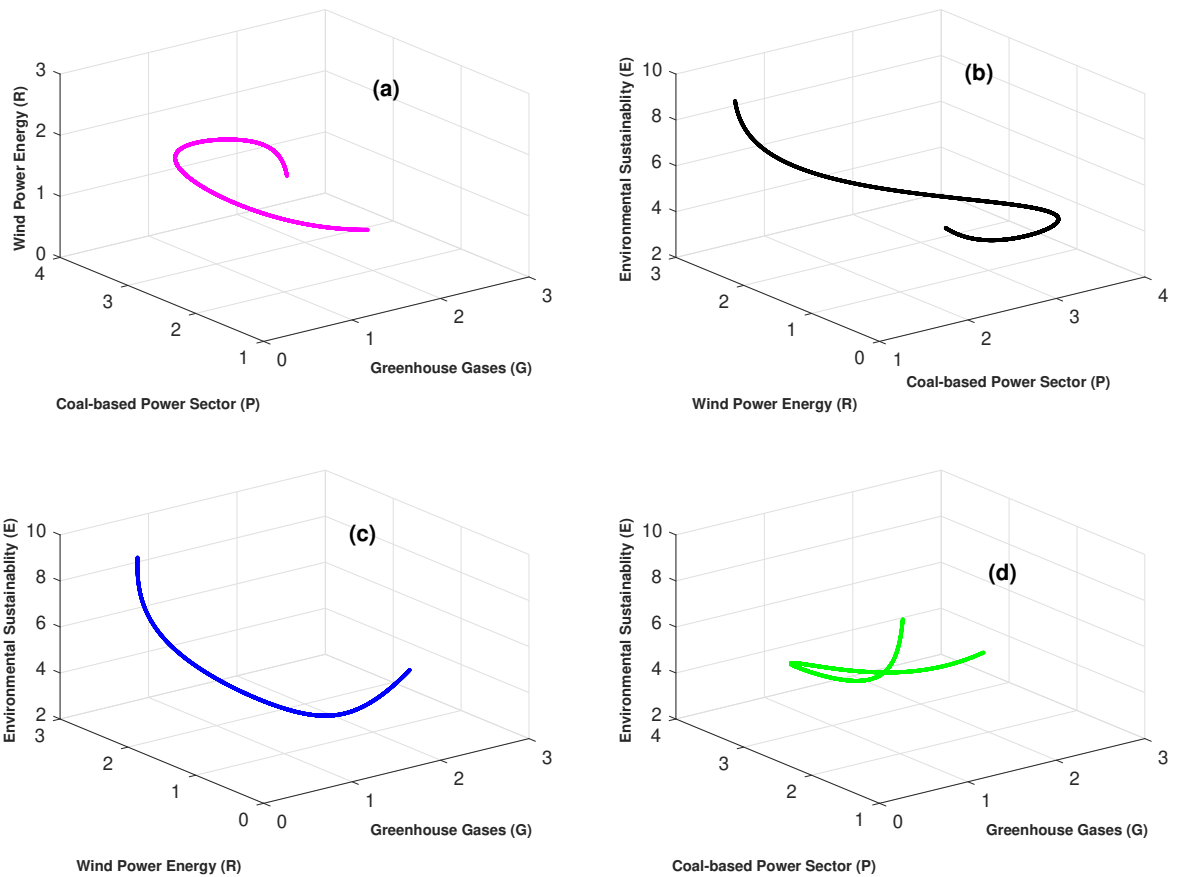


Figure 21. Bifurcation diagram of model (1) for Figure 21(a) greenhouse gases  $G(t)$ , coal-based power sector  $P(t)$  and wind power energy  $R(t)$ . Figure 21(b) coal-based power sector  $P(t)$ , wind power energy  $R(t)$  and environmentally sustainable  $E(t)$ . Figure 21(c) greenhouse gases  $G(t)$ , wind power energy  $R(t)$  and environmentally sustainable  $E(t)$ . Figure 21(d) greenhouse gases  $G(t)$ , coal-based power sector  $P(t)$  and environmentally sustainable  $E(t)$

## 6 Sensitivity analysis

In the context of mathematical modelling, sensitivity analysis is a technique used to understand how changes in the input parameters of a model affect the output or outcomes of the model. It helps quantify the influence of individual parameters on the overall behaviour of the system being modelled. Sensitivity analysis is particularly valuable for assessing the robustness, reliability, and credibility of a model’s results, especially when dealing with complex systems where uncertainties exist. The basic reproduction number, often denoted as  $R_0$ , is a critical concept in epidemiology and mathematical modeling. In our model, the basic reproduction number can be calculated using the method of next-generation matrix. First, let’s find the coal-free equilibrium point by setting all compartments except  $R$  to zero:  $G_0 = 0, P_0 = 0, R_0 = R, E_0 = 0$ .

$$FV = \begin{bmatrix} \epsilon_1 - \epsilon_3 R_0 & 0 & 0 & 0 \\ 0 & \delta_1 - \delta_3 R_0 & 0 & 0 \\ -\epsilon_3 R_0 & -\delta_3 R_0 & \theta_1 + \frac{\theta_2}{a} + \theta_4 & \beta_4 R_0 \\ 0 & 0 & 0 & \beta_1 + \beta_4 R_0 + \beta_5 \end{bmatrix}.$$

In this case, the basic reproduction number  $R_0$  would be

$$R_0 = \max(\epsilon_1 - \epsilon_3 R_0, \delta_1 - \delta_3 R_0, \theta_1 + \frac{\theta_2}{a} + \theta_4, \beta_1 + \beta_4 R_0 + \beta_5). \tag{7}$$

It is essential to conduct a sensitivity study on the model parameters to understand the reliability. It system-

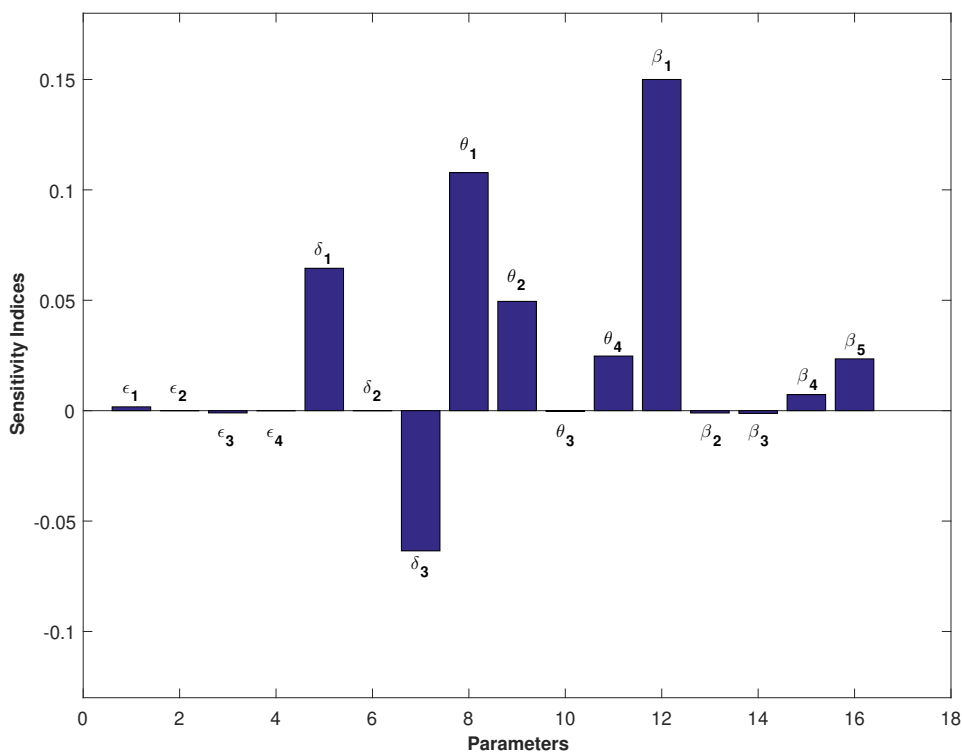


**Figure 22.** Sensitivity diagram for different parameter values of model (1)

atically involves various key parameters to monitor their impact on the model outputs. Here a sensitivity analysis indicates how sustainable energy can increase the reliability of models. The performance rate of wind turbines and energy storage systems can be adjusted to see how changes in technical performance affect the overall system outputs. This is very important for deterioration and technological progress over time. Running the model in best-case and worst-case scenarios for key parameters provides insight into the

range of possible outcomes.

It can help to identify the conditions under which the model works optimally or fails to meet the energy demand. Using simulations to change multiple parameters at random allows a broader understanding of the robustness of the model. This statistical method can provide probability distributions for different outcomes, highlighting the most likely scenarios.

Extending the model to include hybrid renewable energy systems (e.g., wind) can be tested through sensitivity analysis to determine the best mix for reliability and efficiency. Assessing the sensitivity of models to climate variables (e.g., temperature, precipitation) can help understand how future climate conditions may affect renewable energy production and system resilience [8]. In conclusion, a sensitivity study provides important insights into the reliability and robustness of renewable energy models. By systematically changing key parameters, researchers can identify the most influential factors, measure uncertainties, and optimize system design for better performance and resilience.

## 7 Conclusion

Model (1) has been built to represent the influence of coal-based electricity and greenhouse gases by using renewable energy to reduce the significant quantity of carbon emissions from the power industry or to keep the environment sustainable. Then, the constraints and positives for the solution of the model have been studied and two equilibrium positions have been found. After that, the stability at each equilibrium point has been assessed by the next-generation matrix approach. Numerical simulations have been also performed for the model to highlight the dynamic behaviour of the species.

## Declarations

### Use of AI tools

The authors declare that they have not used Artificial Intelligence (AI) tools in the creation of this article.

### Data availability statement

All data generated or analyzed during this study are included in this article.

### Ethical approval (optional)

The authors state that this research complies with ethical standards. This research does not involve either human participants or animals.

### Consent for publication

Not applicable

### Conflicts of interest

The authors declare that they have no conflict of interest.

### Funding

No funding was received for this research.

### Author's contributions

M.S.I.: Conceptualization, Methodology, Data Curation, Writing - Original Draft, Writing - Review & Editing. M.S.K.: Methodology, Software, Validation, Writing - Review & Editing, Visualization, Supervision. M.H.A.B.: Validation, Formal Analysis, Writing - Original Draft, Writing - Review & Editing, Visualization. All authors discussed the results and contributed to the final manuscript.

## Acknowledgements

Not applicable

## References

- [1] UNFCCC, The Paris Agreement, (2015). <https://unfccc.int/process-and-meetings/the-paris-agreement>
- [2] EW, Nutrition, A Guide to International Sustainability Regulations, (2023). <https://ew-nutrition.com/guide-sustainability-regulations/>
- [3] World Economic Forum, Decarbonization of the Power Sector is Underway Power Sector Emissions may have Peaked in 2022 as Wind and Solar Reached Record Heights, (2023). <https://www.weforum.org/agenda/2023/04/>
- [4] Reuters (Nina C.), Wind and Solar Hit Record 12% of Global Power Generation Last Year, (2023). <https://www.reuters.com/business/energy/wind-solar-hit-record-12-global-power-generation-last-year-2023-04-11/>
- [5] Karmaker, A.K., Rahman, M.M., Hossain, M.A. and Ahmed, M.R. Exploration and corrective measures of greenhouse gas emission from fossil fuel power stations for Bangladesh. *Journal of Cleaner Production*, 244, 118645, (2020). [CrossRef]
- [6] Martínez, A.P., Jara-Alvear, J., Andrade, R.J. and Icaza, D. Sustainable development indicators for electric power generation companies in Ecuador: a case study. *Utilities Policy*, 81, 101493, (2023). [CrossRef]
- [7] Amponsah, N.Y., Troldborg, M., Kington, B., Aalders, I. and Hough, R.L. Greenhouse gas emissions from renewable energy sources: a review of lifecycle considerations. *Renewable and Sustainable Energy Reviews*, 39, 461–475, (2014). [CrossRef]
- [8] Chu, B., Duncan, S., Papachristodoulou, A. and Hepburn, C. Analysis and control design of sustainable policies for greenhouse gas emissions. *Applied Thermal Engineering*, 53(2), 420–431, (2013). [CrossRef]
- [9] Liu, B., Xiao, H., Yang, P. and Cai, Z. Influence of the DC frequency limit controller on the frequency characteristics of the multi-area asynchronous interconnected power grid with renewable energy integration. *Frontiers in Energy Research*, 12, 1392285, (2024). [CrossRef]
- [10] Ji, Y., Zhang, J., Li, S., Deng, Y. and Mu, Y. Electric vehicles acceptance capacity evaluation in distribution network considering photovoltaics access. *Energy Reports*, 9, 602–608, (2023). [CrossRef]
- [11] Karmaker, A.K., Ahmed, M.R., Hossain, M.A. and Sikder, M.M. Feasibility assessment & design of hybrid renewable energy based electric vehicle charging station in Bangladesh. *Sustainable Cities and Society*, 39, 189–202, (2018). [CrossRef]
- [12] Kobashi, T., Choi, Y., Hirano, Y., Yamagata, Y. and Say, K. Rapid rise of decarbonization potentials of photovoltaics plus electric vehicles in residential houses over commercial districts. *Applied Energy*, 306, 118142, (2022). [CrossRef]
- [13] Abdullah-Al-Mahbub, M. and Islam, A.R.M.T. Current status of running renewable energy in Bangladesh and future prospect: a global comparison. *Heliyon*, 9(3), e14308, (2023). [CrossRef]
- [14] Hassan, M.A., Bailek, N., Bouchouicha, K., Ibrahim, A., Jamil, B., Kuriqi, A. et al. Evaluation of energy extraction of PV systems affected by environmental factors under real outdoor conditions. *Theoretical and Applied Climatology*, 150, 715–729, (2022). [CrossRef]
- [15] Umair, M. and Yousuf, M.U. Evaluating the symmetric and asymmetric effects of fossil fuel energy consumption and international capital flows on environmental sustainability: a case of South Asia. *Environmental Science and Pollution Research*, 30, 33992–34008, (2022). [CrossRef]
- [16] Biswas, M.H.A., Dey, P.R., Islam, M.S. and Mandal, S. Mathematical model applied to green building concept for sustainable cities under climate change. *Journal of Contemporary Urban Affairs*, 6(1), 36–50, (2021). [CrossRef]

- [17] Kabeyi, M.J.B. and Olanrewaju, O.A. Sustainable energy transition for renewable and low carbon grid electricity generation and supply. *Frontiers in Energy Research*, 9, 743114, (2022). [CrossRef]
- [18] EPA, Inventory of U.S. Greenhouse Gas Emissions and Sinks, (2017). <https://www.epa.gov/ghgemissions/inventory-us-greenhouse-gas-emissions-and-sinks>
- [19] Mandal, S., Islam, M.S. and Biswas, M.H.A. Modeling the potential impact of climate change on living beings near coastal areas. *Modeling Earth Systems and Environment*, 7, 1783–1796, (2020). [CrossRef]
- [20] Sekerci, Y. and Petrovskii, S. Mathematical modelling of plankton–oxygen dynamics under the climate change. *Bulletin of Mathematical Biology*, 77, 2325–2353, (2015). [CrossRef]
- [21] Elum, Z.A. and Momodu, A.S. Climate change mitigation and renewable energy for sustainable development in Nigeria: a discourse approach. *Renewable and Sustainable Energy Reviews*, 76, 72–80, (2017). [CrossRef]
- [22] Ledley, T.S., Sundquist, E.T., Schwartz, S.E., Hall, D.K., Fellows, J.D. and Killeen, T.L. Climate change and greenhouse gases. *Eos, Transactions American Geophysical Union*, 80(39), 453–458, (1999). [CrossRef]
- [23] US EPA, Household Carbon Footprint Calculator, (2016). <https://www.epa.gov/ghgemissions/household-carbon-footprint-calculator>
- [24] Ahmed, S., Islam, M.T., Karim, M.A. and Karim, N.M. Exploitation of renewable energy for sustainable development and overcoming power crisis in Bangladesh. *Renewable Energy*, 72, 223–235, (2014). [CrossRef]
- [25] The UN Climate Change Conference, (2023). <https://unfccc.int/>
- [26] WWEA, WWEA Annual Report 2022, (2023). <https://wwindea.org/wwea-annual-report-2022>
- [27] Islam, R., Islam, M.M., Islam, M.N., Islam, M.N., Sen, S. and Faisal, R.K. Climate change adaptation strategies: a prospect toward crop modelling and food security management. *Modeling Earth Systems and Environment*, 6, 769–777, (2020). [CrossRef]
- [28] Dym, C.L. *Principles of Mathematical Modeling*. Elsevier Academic Press: Amsterdam, (2004).

Mathematical Modelling and Numerical Simulation with Applications (MMNSA)  
(<https://dergipark.org.tr/en/pub/mmnsa>)



**Copyright:** © 2024 by the authors. This work is licensed under a Creative Commons Attribution 4.0 (CC BY) International License. The authors retain ownership of the copyright for their article, but they allow anyone to download, reuse, reprint, modify, distribute, and/or copy articles in MMNSA, so long as the original authors and source are credited. To see the complete license contents, please visit (<http://creativecommons.org/licenses/by/4.0/>).

**How to cite this article:** Islam, M.S., Khatun, M.S. & Biswas, M.H.A. (2024). Mathematical modelling of using renewable energy in the power sectors for the sustainable environment. *Mathematical Modelling and Numerical Simulation with Applications*, 4(2), 216-237. <https://doi.org/10.53391/mmnsa.1446574>